1-1-2017

Selective Atomic Layer Deposition Of Transition Metal Thin Films

Marissa Marie Kerrigan
Wayne State University,

Recommended Citation

Kerrigan, Marissa Marie, "Selective Atomic Layer Deposition Of Transition Metal Thin Films" (2017). *Wayne State University Dissertations*. 1822.
https://digitalcommons.wayne.edu/oa_dissertations/1822

SELECTIVE ATOMIC LAYER DEPOSITION OF TRANSITION METAL THIN FILMS

by

MARISSA MARIE KERRIGAN

DISSERTATION

Submitted to the Graduate School

of Wayne State University,

Detroit, Michigan

in partial fulfillment of the requirements

for the degree of

DOCTOR OF PHILOSOPHY

2017

MAJOR: CHEMISTRY (Inorganic)

Approved By:

Advisor Date

DEDICATION

I dedicate this dissertation to Patrick Edward Frost. Your constant support and love have helped to make all that I have accomplished possible. Words cannot express my gratitude for all that you do for me.

"The science of today is the technology of tomorrow."

- Edward Teller

ACKNOWLEDGMENTS

The most difficult section of this document to write is this one. There are so many people to whom I am forever indebted for their support over these last few years. I am at a loss for words to express adequately my gratitude to you all.

My first word of thanks goes to the most influential person in my graduate career, my advisor, Professor Charles “Chuck” H. Winter. Chuck, you have been instrumental in my growth as a scientist and as a person over these past four and a half years. Every challenge I have faced, you have driven me to exceed and excel. I am proud to have accomplished all that I have under your guidance. I can truly say, I would not be the person I am today without you.

I would next like to thank my committee, Professors Stanislav “Stas” Groysman and Jeremy Kodanko. I have appreciated all of the input you have given to me throughout my studies. You have made invaluable suggestions for my research, and I am lucky to have such knowledgeable and distinguished experts in organometallic chemistry helping my development as a chemist.

I would especially like to thank the last member of my committee, Charles “Chuck” Leroy Dezelah IV. Before I was even “officially” in the Winter Lab, you taught me so much about ALD and the hardware for the reactors, which has been instrumental in everything I have done for my studies. You have also been my chauffer, manager, sounding-board, chemistry-spirit guide, paper-hat-Chuck, trivia and beer connoisseur, and most of all, my friend. You have always been there whenever I needed advice for science or just in general, you are a truly amazing friend.

I have enjoyed the time I have spent with my labmates. The imparting of knowledge, the sharing of ideas, and comradery in the Winter group have invaluably impacted my experience at Wayne State University. I would especially like to thank Tom, Chatu, Lakmal, Joe, Wathsala, Joseph, and Josh.

Something I feel that is unique to the Winter group, is the unwavering support of our former group members. I have had countless enlightening conversations with many of my former group members, including but not limited to: Chatu Sirammane, Chuck Dezelah, Mark Saly, Lakmal Kalutarage, and Tom Knisley. Tom, you have been especially influential to my development as a scientist. From our similar experiences from U of M – Dearborn to Wayne State University, you have been an impeccable role model for me both personally and professionally. Your encouragement and friendship from the very start has made me strive to be my very best.

As I have expressed what is unique to the Winter group, I would now like to share what I feel is unique to Wayne State University Chemistry Department. First and foremost, I started my studies with a group of 49 PhD students (Fall 2012). Each and every one of you has helped me along the way, especially Habib and Lucas. From studying for classes, to studying for cumes, to just going out for karaoke, you are 48 of the best people I have ever met. I am better for having known all of you. I have also been fortunate enough to make friends with other students past my own incoming year, which I again feel is unique to Wayne State University Chemistry Department. Everyone I have met here has helped me to grow, giving me advice with course work, seminars, and everything in between. Thank you for everything.

Wayne State University Chemistry Department also has the absolute best faculty and staff. Our building managers, formerly Mary Gorny Wood and currently Jackie Baldyga, have made every scientific breakthrough possible by keeping our building in impeccable running order. They are the oil that greases the wheels in our machine. Melissa Barton, who is technically the "Academic Service Officer" for our department, requires an extra acknowledgement. Her title does not do justice to all she does for every single student with whom she has ever worked. Melissa, your advice, and hugs, are the best and not a single one of us could ever thank you enough for you guidance. You truly are Wonder Woman. I would also like to express my gratitude to our faculty. Professor Jennifer "Jenn" L. Stockdill, if I had to pick one woman scientist who has inspired me the most, it would be you. You are intelligent, funny, tenacious, and one of the most caring people I have ever met. I am proud to call you my friend. I am inspired by everything you have accomplished at the beginning of your career, and I can't wait to see the wonderful things you achieve in the years to come. Thank you for you guidance and friendship Jenn. Professor Tamara Hendrickson, thank you for the cats, they are the best ever. Thank you to all of the lecturing professors that I have interacted with. Professor Barber, I enjoyed learning the teaching aspect of chemistry from you, and thanks for the pizza and the life and religious guidance. Professor Munk, as a fellow grad student from Wayne State University, I feel that we have all gained from your experience and advice on finals and cumes. You have been a life saver with all of the chocolate you have provided throughout the years, thank you. Last but not least, I want to thank the entire Inorganic faculty. I have enjoyed the years I have spent learning from you, whether in a formal setting (lectures or seminars), or just a casual chat in the hallway. Professors Matt Allen, Stephanie Brock, Stas Groysman, Federico Rabuffetti, Claudio Verani, and my advisor Chuck Winter, I have had invaluable experiences that I have gained from each and every one of you. You are the reason that Wayne State University Chemistry graduates achieve all that they do.

The Lumigen Instrument Center (LIC) is a top of the line facility. Without its wonderful instrumentation and staff, our department's work would not be to the highest-caliber that it has reached. Thank you to Johnna Birbeck, Yurii Danyliuk, Bashar Ksebati, Zhi "Mike" Mei, Phillip Martin, and Judy Westrick. I would also like to thank the staff in the business office (who allows travel, purchasing, and benefits to run smoothly) and the staff in the storeroom (who can always help find whatever it is you need to complete your experiments): Gregory Kish, Diane Kudla, Kellie Lauder, Bernie Miesik, Bonnie Miller, Fran Owczarek, Jason Parizon, Elizabeth Ries, and Lisa Smith.

My high school teachers have had a profound impact on my life. My early education is from Taylor Public Schools, and I could not ask for a better one. I would especially like to thank Ken Hastings, my chemistry teacher, who sparked my interest in chemistry. I would also like to thank Jack Nelson, my physics teacher, who introduced me to the Socratic method of teaching. That basic skill set for learning helped me through college and grad school, thank you.

The most important people I would like to thank are my family. My parents, Paula and Timothy Kerrigan, have been the main source of encouragement for me to strive to be my very best. They have laid the foundation for my success by their example throughout my life. My brothers, James and Shaun Kerrigan, have always been the people I have looked up to the most. You have always supported and pushed me to be my best at whatever I have attempted, and you have always called me out if I gave less than what I was capable. My family is the reason that I even attempted my PhD course work. Thank you for having high expectations for me, and helping me to achieve them. My fiancé Patrick Frost, has been my best friend, my proof-reader, the one I have turned to when I was struggling, when I was celebrating, when I needed advice, when I needed reassurance, and when I needed a rock. All that I have attempted, let alone accomplished, is a tribute to the love and support you have shown me. I also want to thank SP and MJ, you have been my comfort and strength when I needed you. I love you all.

TABLE OF CONTENTS

Dedication……………………………………………………………………………...ii

Acknowledgements……………………………………………………………….....iii

List of Tables…………………………………………………………………….....ix

List of Figures………………………………………………………………………..x

List of Charts……………………………………………………………………….xiv

List of Abbreviations………………………………………………………….….xv

CHAPTER 1 – Introduction…………………………………………………………1

CHAPTER 2 – Substrate Selectivity in The Low Temperature, Thermal Atomic Layer Deposition of Cobalt Metal Thin Films from Bis(1,4-di-*tert*-butyl-1,3-diazadienyl)cobalt and Formic Acid………………………………………………………………….30

CHAPTER 3 – Low Temperature Growth and Substrate Selectivity of Cobalt Metal Thin Films by Thermal Atomic Layer Deposition from Bis(1,4-di-*tert*-butyl-1,3-diazadienyl)cobalt and Amines……………………………………………………..64

CHAPTER 4 – Low Temperature Growth and Substrate Selectivity of Nickel Metal Thin Films by Thermal Atomic Layer Deposition from Bis(1,4-di-*tert*-butyl-1,3-diazadienyl)nickel and Amines……………………………………………………..92

CHAPTER 5 – Conclusion………………………………………………………...118

Appendix – Permissions……………….……………………………………..…122

References……………………………………………………………...…….123

Abstract……………………………………………………………………………131

Autobiographical Statement………………………………………………………133

LIST OF TABLES

Table 1. Applications and reduction potentials of first row transition metals in micro-electronic devices……………………………………………………………20

Table 2. Resistivities of cobalt films grown on metallic substrates using Co(^{tBu2}DAD)$_2$ and formic acid…………………………………………………………………..40

Table 3. Resistivities of cobalt films grown on metallic substrates using Co(^{tBu2}DAD)$_2$ and *tert*-butyl amine…………………………………………………………...……81

Table 4. Resistivities of nickel films grown on metallic substrates using Ni(^{tBu2}DAD)$_2$ and *tert*-butyl amine……………………...…………………………………...…111

LIST OF FIGURES

Figure 1. Miniaturization roadmap from 2011 – 2020 for functional device component size……………………………………………………………………..…….1

Figure 2. Schematic of a cross-sectional view of a transistor. “L” represents the distance between the source and the drain, which is also known as the node………………3

Figure 3. General schematic for evaporative PVD………………………………………..6

Figure 4. General schematic for PVD sputtering…………………………………………7

Figure 5. General schematic for CVD……………………………………………………..9

Figure 6. High-aspect ratio features (≤ 20 nm) coated by PVD/CVD and ALD, respectively……………………………………………………………………....10

Figure 7. General saturation curve for an ALD process. Region 1 indicates sub-saturative growth, while region 2 indicates saturative growth………………………………11

Figure 8. General ALD window. The various regions depict insufficient reactivity (solid line, region 1), precursor condensation (dashed line, region 1), the ALD window (region 2), surface deactivation (dashed line, region 3) and precursor self-decomposition (solid line, region 3)…………………………………….……..12

Figure 9. General thickness *versus* number of cycles plot. Normal ALD growth proceeds in a linear fashion, and can be described using the equation y = mx +b. The slope, or “m,” is the growth rate for the process. The y-intercept of the graph, or “b,” should ideally be zero…………………………………………………………….……13

Figure 10. General ALD cycle……………………………………………………………..14

Figure 11. Comparison of normal ALD growth to substrate-selective ALD growth, respectively……………………………………………………………………16

Figure 12. General reaction scheme for the ALD growth of cobalt metal from Co(^{tBu2}DAD)$_2$ and formic acid………………………………………………...30

Figure 13. Plot of thickness versus number of cycles for cobalt metal growth on ruthenium, platinum, and copper substrates at 180 °C……………………………………..32

Figure 14. Cross-sectional SEM of a 14 nm thick cobalt metal film grown at 180 °C, on a) a platinum substrate b) a copper substrate..…………………………………....33

Figure 15. EDS spectrum for 25 cycles (~2.5 nm) of cobalt metal grown at 180 °C, on a) a platinum substrate and b) a copper substrate..…………………………………..35

Figure 16. AFM images of 15 nm thick cobalt metal film grown on a) platinum and b) copper. The inset shows a smooth region of the cobalt on copper film. Cobalt on platinum: rms = 0.6 nm. Cobalt on copper: rms = 2.4 nm, inset rms = 1.1 nm..…38

Figure 17. High-resolution XPS multiplex of a) the Co 2p region of a 14 nm thick cobalt film grown on a platinum substrate at 180 °C b) the Co 2p region of a cobalt metal standard.……………………………………………………………………42

Figure 18. a) Plot of atomic concentration versus argon ion sputtering time, b) elemental compositions of a 14 nm thick cobalt film grown on a platinum substrate at 180 °C ……………………………………………………………………………....44

Figure 19. High-resolution XPS multiplex of the Co 2p region of a 14 nm thick cobalt film grown on a copper substrate at 180 °C…………………………………………...47

Figure 20. Plot of atomic concentration versus argon ion sputtering time of a 14 nm thick cobalt film grown on a copper substrate at 180 °C …………………………...48

Figure 21. a) Cross-sectional SEM of a CDO substrate after 1000 deposition cycles at 180 °C b) EDS of a CDO substrate after 1000 deposition cycles at 180 °C…………..50

Figure 22. High-resolution XPS multiplex of a CDO substrate after 150 deposition cycles at 180 °C…………………………………………………………………….52

Figure 23. EDS of ~35 nm of film after 500 deposition cycles on SiO_2…………………54

Figure 24. Cross-sectional SEM of ~35 nm of film after 500 deposition cycles on SiO_2, a) before deionized water rinse and b) after deionized water rinse …………………55

Figure 25. Infrared spectrum of ~35 nm of film after 500 deposition cycles on SiO_2…...57

Figure 26. Area-selective ALD temperature windows, where no growth was observed on Si(100), Si-H, and CDO substrates after 250 cycles …………………………..…69

Figure 27. General reaction scheme for the deposition of cobalt metal thin films from Co(^{tBu2}DAD)$_2$ and *tert*-butyl amine by thermal ALD……………………………65

Figure 28. Plot of growth rate of cobalt metal on platinum substrates *versus* pulse length of Co(^{tBu2}DAD)$_2$ after 200 cycles, using Co(^{tBu2}DAD)$_2$ and *tert*-butyl amine as precursors ………………………………………………………………………..66

Figure 29. Plot of growth rate of cobalt metal on platinum substrates *versus* pulse length of *tert*-butyl amine after 200 cycles, using Co(^{tBu2}DAD)$_2$ and *tert*-butyl amine as precursors ………………………………………………………………………..67

Figure 30. Plot of growth rate *versus* deposition temperature for cobalt metal growth on platinum substrates after 200 cycles using Co(^{tBu2}DAD)$_2$ and *tert*-butyl amine ……………………………………………………………………………....68

Figure 31. Plot of thickness *versus* number of cycles for cobalt metal growth on platinum substrates at 200 °C using Co(^{tBu2}DAD)$_2$ and *tert*-butyl amine.…………………..69

Figure 32. X-ray diffraction pattern for ~50 nm thick cobalt metal film grown on a platinum substrate at 200 °C using Co(^{tBu2}DAD)$_2$ and *tert*-butyl amine ……….....70

Figure 33. Atomic force microscopy 5 x 5 μm^2 area image of a ~10 nm thick cobalt metal film (100 cycles) grown on a platinum substrate at 200 °C using Co(^{tBu2}DAD)$_2$ and *tert*-butyl amine; rms roughness = 0.22 nm…………………………………....71

Figure 34. Atomic force microscopy 5 x 5 μm^2 area image of an ~100 nm thick cobalt metal film (1000 cycles) grown on a platinum substrate at 200 °C using Co(^{tBu2}DAD)$_2$ and *tert*-butyl amine; rms roughness = 3.07 nm………………….72

Figure 35. High-resolution XPS multiplex of cobalt 2p region of a) 50 nm and b) 100 nm thick cobalt film grown on platinum using Co(^{tBu2}DAD)$_2$ and *tert*-butyl amine; c) reference cobalt film…………………………………………………………...73

Figure 36. a) XPS depth profile and b) elemental compositions of a ~100 nm thick cobalt film grown on platinum at 200 °C, using Co(^{tBu2}DAD)$_2$ and *tert*-butyl amine…...76

Figure 37. Plot of thickness *versus* number of cycles for the early growth stages of cobalt metal on ruthenium, copper, and platinum substrates at 200 °C using Co(^{tBu2}DAD)$_2$ and *tert*-butyl amine……………………………………………………….....78

Figure 38. Cross-sectional SEM of a 20 nm thick cobalt metal film grown at 200 °C, on a) a platinum substrate b) a copper substrate ……………………………………….79

Figure 39. a) Cross-sectional SEM of a CDO substrate after 500 deposition cycles at 200 °C b) EDS of a CDO substrate after 500 deposition cycles at 200 °C…………...82

Figure 40. Area-selective ALD temperature windows, where no growth was observed on Si(100), Si-H, and CDO substrates after 200 cycles……………………………...84

Figure 41. Cross-sectional SEM after 200 deposition cycles at 200 °C using Co(^{tBu2}DAD)$_2$ and a) diethyl amine b) triethyl amine……………………………………………85

Figure 42. Plot of thickness *versus* number of cycles for cobalt metal growth on platinum substrates at 200 °C using Co(^{tBu2}DAD)$_2$ and *tert*-butyl amine, using lower purity N_2 carrier gas……………………………………………………………………..87

Figure 43. High-resolution XPS multiplex of cobalt 2p region of an 100 nm thick cobalt film grown on platinum, at 200 °C, using N_2 produced by a nitrogen generator, Co(^{tBu2}DAD)$_2$, and *tert*-butyl amine……………………………………….…88

Figure 44. General reaction scheme for the deposition of nickel metal thin films from Ni(^{tBu2}DAD)$_2$ and *tert*-butyl amine by thermal ALD……………………………..93

Figure 45. Plot of growth rate of nickel metal on platinum substrates *versus* pulse length of Ni(^{tBu2}DAD)$_2$ after 500 cycles, using Ni(^{tBu2}DAD)$_2$ and *tert*-butyl amine as precursors……………………………………………………………………...94

Figure 46. Plot of growth rate of nickel metal on platinum substrates *versus* pulse length of *tert*-butyl amine after 500 cycles, using Ni(^{tBu2}DAD)$_2$ and *tert*-butyl amine as precursors……………………………………………………………………...95

Figure 47. Plot of growth rate *versus* deposition temperature for nickel metal growth on platinum substrates after 250 cycles using Ni(^{tBu2}DAD)$_2$ and *tert*-butyl amine.…………………………………………………………………….....96

Figure 48. Plot of thickness *versus* number of cycles for nickel metal growth on platinum substrates at 200 °C using Ni(^{tBu2}DAD)$_2$ and *tert*-butyl amine ………………..…97

Figure 49. X-ray diffraction pattern for a ~60 nm thick nickel metal film grown on a platinum substrate at 180 °C using Ni(^{tBu2}DAD)$_2$ and *tert*-butyl amine………..…98

Figure 50. Atomic force microscopy 5 x 5 μm^2 area image of a ~18 nm thick nickel metal film grown on a platinum substrate at 180 °C using Ni(^{tBu2}DAD)$_2$ and *tert*-butyl amine; rms roughness = 0.45 nm………………………………………………99

Figure 51. Atomic force microscopy 5 x 5 μm^2 area image of a ~60 nm thick nickel metal film grown on a platinum substrate at 180 °C using Ni(^{tBu2}DAD)$_2$ and *tert*-butyl amine; rms roughness = 1.52 nm……………………………………………..100

Figure 52. High-resolution XPS multiplex of nickel 2p region of a) 18 nm and b) 60 nm thick nickel film grown on platinum, at 180 °C, using Ni(^{tBu2}DAD)$_2$ and *tert*-butyl amine; c) reference nickel film…………………………………………………102

Figure 53. a) XPS depth profile and b) elemental compositions of an 18 nm thick nickel film grown on platinum at 180 °C using Ni(^{tBu2}DAD)$_2$ and *tert*-butyl amine….105

Figure 54. XPS depth profile of a 60 nm thick nickel film grown on platinum at 180 °C using Ni(^{tBu2}DAD)$_2$ and *tert*-butyl amine……………………………………106

Figure 55. Plot of thickness *versus* number of cycles for the growth of nickel metal on ruthenium, copper, and platinum substrates at 180 °C using Ni(^{tBu2}DAD)$_2$ and *tert*-butyl amine………………………………………………………………..…109

Figure 56. a) Cross-sectional SEM of a CDO substrate after 1000 deposition cycles at 180 °C b) EDS of a CDO substrate after 1000 deposition cycles at 180 °C…………112

Figure 57. Area-selective ALD temperature window, where no growth was observed on Si(100), Si-H, and CDO substrates after 250 cycles…………………………....114

LIST OF CHARTS

Chart 1. Examples of common cobalt precursors for thin film depositions……………...23

Chart 2. Examples of common nickel precursors for thin film depositions……………...27

LIST OF ABBREVIATIONS

ABBREVIATION	**LONG FORM**
acac	Acetylacetonate
AFM	Atomic Force Microscopy
ALD	Atomic Layer Deposition
at.%	Atomic %
CCTBA	μ^2-η^2-(*tert*-butylacetylene)-dicobalthexacarbonyl
Cp	Cyclopentadienyl
CVD	Chemical Vapor Deposition
DMAMB	1-Dimethylamino-2-methyl-2-butoxide
DMAMP	1-Dimethylamino-2-methyl-2-propoxide
DMAP	1-Dimethylamino-2-propoxide
EDS	Energy-Dispersive X-ray Spectroscopy
^{iPr2}DAD	1,4-Di-isopropyl-1,3-diazadienyl
MeCp	Methylcyclopentadienyl
MRAM	Magnetoresistive Random Access Memory
PEALD	Plasma-Enhanced Atomic Layer Deposition

PVD	Physical Vapor Deposition
RMS	Root Mean Square
SAM	Self-Assembled Monolayer
SEM	Scanning Electron Microscopy
$^{\mathrm{tBu2}}$DAD	1,4-di-*tert*-butyl-1,3-diazabutadiene
tmhd	2,2,6,6-tetramethylheptanedionate
wt.%	Weight %
XPS	X-Ray Photoelectron Spectroscopy
XRD	X-Ray Diffraction

CHAPTER 1 INTRODUCTION

1.1 Trends in Integrated Circuits Technology Miniaturization

Microelectronic manufacturing process development has profound implications on a global scale, due to the worldwide saturation of consumer electronic devices. The advancement of microelectronics devices has consistently followed Moore's law, which states that the number of transistors per unit area on an integrated circuit will double approximately every two years.[1-7] The increased density of transistors (and therefore, decreased size) has been observed continuously since the 1960's, with functional devices predicted to employ transistors with 10 nm node (the distance between the source and the drain on a transistor) as soon as 2017 (**Figure 1**).[8] Continually increasing transistor density has, in turn, led to continually decreasing size and power consumption of consumer electronic devices – making today's connected world possible.

Figure 1. Miniaturization roadmap from 2011 – 2020 for functional device component size.

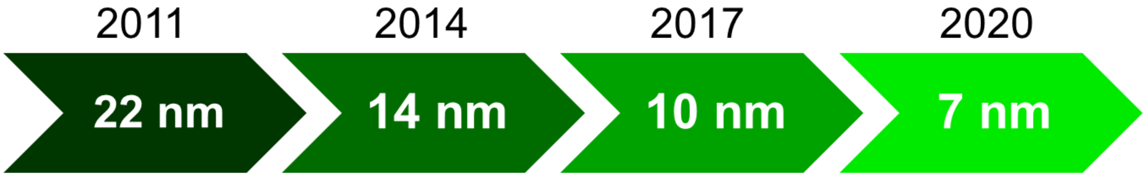

To comply with the demand for higher density integrated circuits, the architectural design of integrated circuits has evolved greatly over the last sixty years, with initial designs being two-dimensional circuits on a single layer.[4-5] As the demand for faster and higher performing integrated circuits grew, the archetypal two-dimensional structure became obsolete; compression methods were used to increase density in conjunction with decreasing the transistor size.[4-5] Two-dimensional compression reached its limit, giving way to a three-dimensional stacking of circuit layers. The three-dimensional architecture is comprised of many high-aspect ratio features, such as trenches and vias, to connect individual layers.[4-5, 7] High-aspect ratio features must be precisely and uniformly coated to minimize process tolerances, allowing for higher device manufacturing yield. The ability to coat high-aspect ratio features with precision is required if the current trend in microelectronics miniaturization is to continue, while still keeping costs to the consumer low.[1-3, 7]

Transistors are the building blocks of integrated circuits, and are composed of dielectric (gate), semiconductive (substrate), and conductive (interconnect) materials.[4-5] Transistors function as binary "on/off" switches (**Figure 2**), and can be combined to form logic networks. Some of the simplest transistors form the "AND" and "OR" logical operations, while more complex networks provide the backbone of mathematical and data storage processing. To turn the transistor "on," a voltage is applied to the dielectric gate to open a current path from the source to the drain. The open current path from the source to the drain represents the logical "1," as the transistor output voltage is the same as the source voltage. Similarly, to turn the transistor "off," the dielectric gate is grounded, closing the path from the source to the drain. The threshold voltage, which is defined as the lowest required voltage at the gate to open the current path from source to drain, needs to be low so that the heat dissipation for the device is low while in use (to prolong device life).[4-5] However, the threshold voltage needs to be high enough that the device cannot be turned on accidently.

Figure 2. Schematic of a cross-sectional view of a transistor. “L” represents the distance between the source and the drain, which is also known as the node.

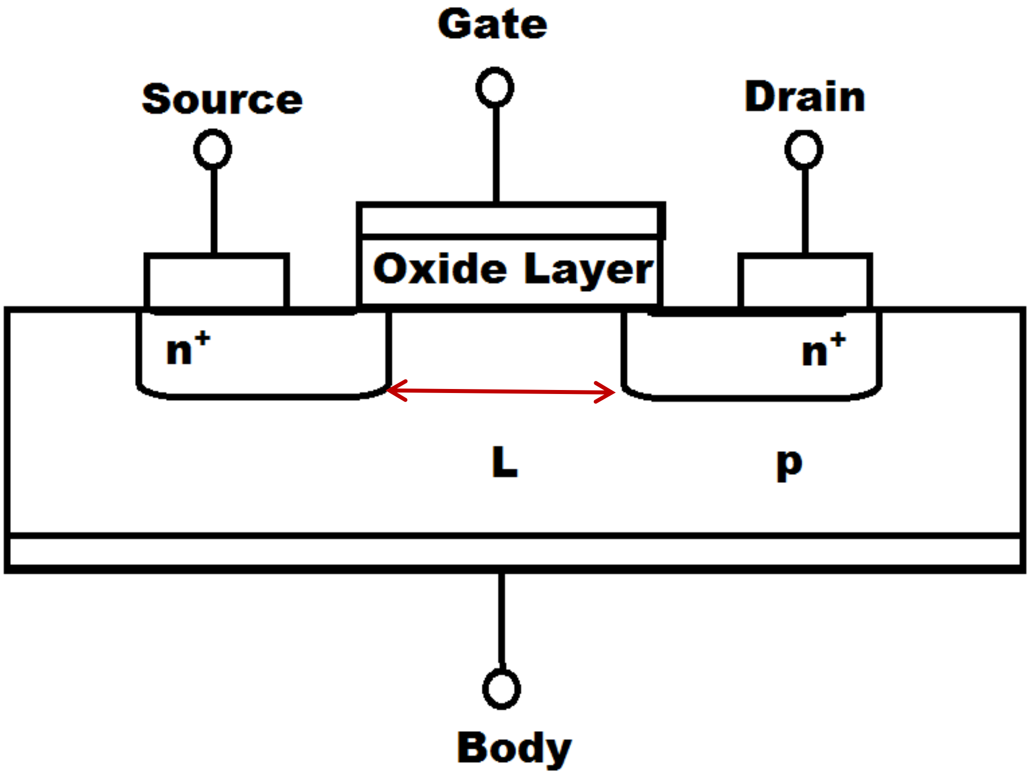

One challenge with the miniaturization of components is the fabrication of the dielectric gate oxide. As the thickness decreases, leakage current from the source to the drain increases, leading to inefficient devices and significant energy waste.[9-11] Traditionally, SiO_2 has been used as the gate oxide, but when the gate oxide is less than 15 nm thick, SiO_2 is no longer sufficient to prevent current leakage.[12] In modern integrated circuits, HfO_2 is used for the gate oxide, but also has its limits: less than 12 nm thick, HfO_2 also fails to prevent significant leakage current. New materials are needed in order to continue the transistor miniaturization trend, while minimizing leakage current.[7]

Another challenge in integrated circuit manufacturing is the miniaturization of interconnects. Aluminum was commonly used as an interconnect material in early generations, as a result of its relative abundance, low cost, and low resistivity. Copper has largely replaced aluminum as an interconnect material in later generation devices, due to its higher scalability, lower resistivity, and lower heat dissipation.[4-5] The challenge in using copper is in its adhesion to the dielectric layer, since copper poorly nucleates on insulating substrates. The nucleation challenge prevents the formation of uniform, continuous layers. Copper also has a high tendency to diffuse into silicon and SiO_2 at the temperatures necessary for device manufacturing,[3, 13] leading to the formation of short circuits. The use of an inert material with good adhesion to both copper and SiO_2 is necessary to prevent the diffusion of copper into the dielectric components. The main challenge in the miniaturization of interconnects is finding a suitable adhesion/diffusion barrier layer for copper at this scale. The current state of the art is TaN, though this material ceases to be effective at ≤ 5 nm thickness.[14] As the demand for smaller transistor components (< 20 nm) increases, the production of conformal thin films with precise control of thickness is required to facilitate miniaturization of microelectronic devices.

1.2 Current Methods of Thin Film Deposition

1.2.1 Physical Vapor Deposition

Physical vapor deposition (PVD) is a well-established thin film deposition technique employed within the microelectronics industry to manufacture device components. The ubiquity of PVD is due to its high quality films and relatively inexpensive operating cost requirements.[15] Examples of PVD techniques include sputter deposition, laser-ablation deposition, evaporation, and vacuum arc-based deposition. The two most common PVD methods used in the microelectronics industry are the evaporation and sputtering techniques.[15] In these two methods, deposition occurs *via* the removal of atoms from the bulk-source material by using evaporation or high-energy particle bombardment in a high-vacuum deposition chamber.[15]

Evaporative deposition techniques are characterized by the heating of the source material beyond its melting point, using a highly biased (-5000V) filament, with the substrate placed in a direct line-of-sight to the source (**Figure 3**).[15] Typically, there is a relatively large distance between the source and the substrate (10 – 100 cm) to optimize deposition area while also limiting substrate heating.[15] Optimizing the distance between the source and the substrate is necessary, because a larger distance will result in a slower deposition rate, since the deposition rate is inversely proportional to the distance squared.[15] This technique is even able to coat large, meter-width diameter substrates at relatively fast rates (~100 nm/min), contributing to its wide use in industrial applications.[15]

Figure 3. General schematic for evaporative PVD.

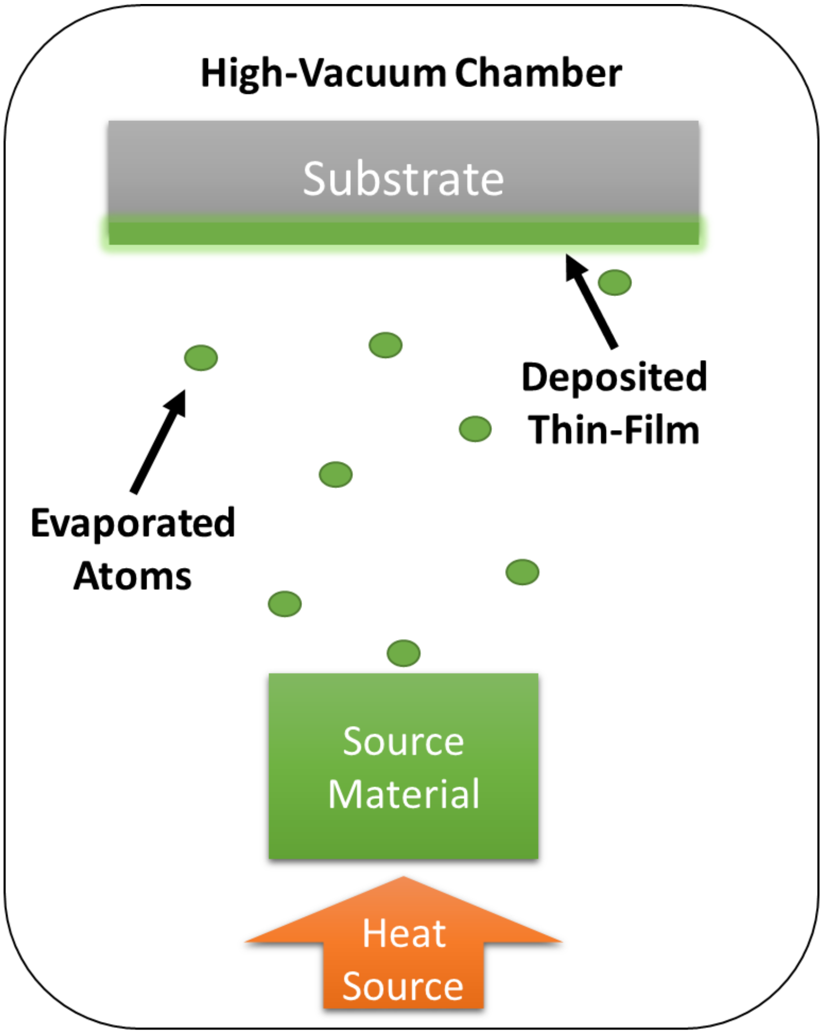

Another common PVD technique used in manufacturing is sputtering. Sputtering uses an ion beam source to generate energetic particles of inert gas ions (50 – 2000 eV) which collide with the source material, liberating atoms into the vapor phase for thin film deposition (**Figure 4**).[15] In order for these atoms to be cleaved from the source material, the energy of the particles generated from the ion beam source must exceed that of the surface binding energy of the source material.[15] Once in the vapor phase, these sputtered atoms then deposit on the substrate, forming a thin film of the desired material.

Figure 4. General schematic for PVD sputtering.

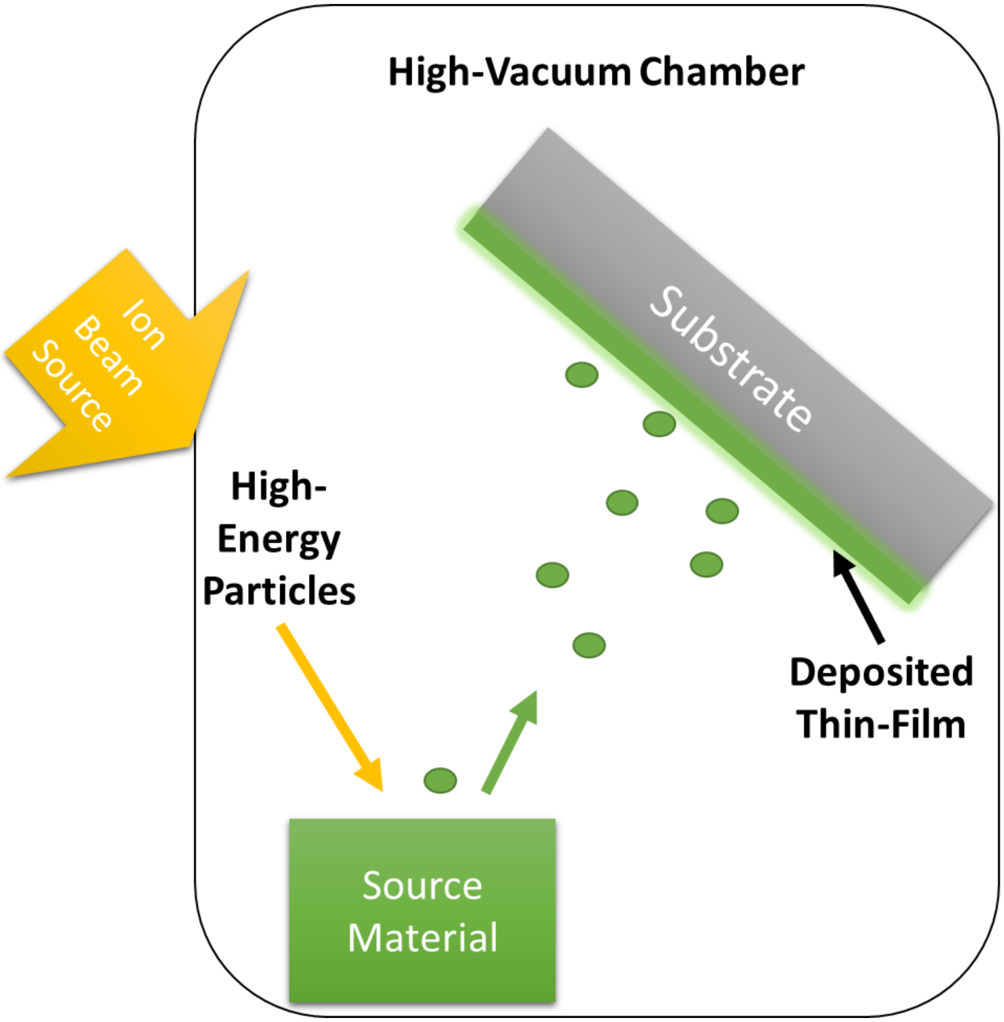

Sputtering PVD techniques are widely used in the manufacturing processes for device components in the microelectronic industry, due to the high quality and throughput of materials produced and inexpensive material operating costs in comparison to other available deposition techniques.[15] Although the material deposited through sputtering is still held as a quality standard in the microelectronics industry, the directional nature of

PVD limits the ability to coat high-aspect ratio features, with this limitation typically more pronounced in feature sizes of < 250 nm.[16] Because of this limitation, new techniques are required due to the continued drive for miniaturization, to afford films with excellent step-coverage of high-aspect ratio trenches and vias while keeping consumer costs low and quality high.

1.2.2 Chemical Vapor Deposition

Chemical vapor deposition (CVD) occurs when a heated substrate is exposed to one or more gas-phase precursors delivered into a reaction chamber by a steady flow of an inert carrier gas (**Figure 5**).[2, 17-18] These reactions are often performed in a vacuum chamber at high temperatures (≥ 500 °C). Deposition of the desired thin film can occur by gas-phase reactions of the precursor (with the resulting product precipitating onto the substrate) and/or by pyrolysis, which is the thermal decomposition of the precursors onto the substrate.[2, 17-18] Any volatile by-products or excess precursors are removed from the reaction chamber by the carrier gas flow.

Figure 5. General schematic for CVD.

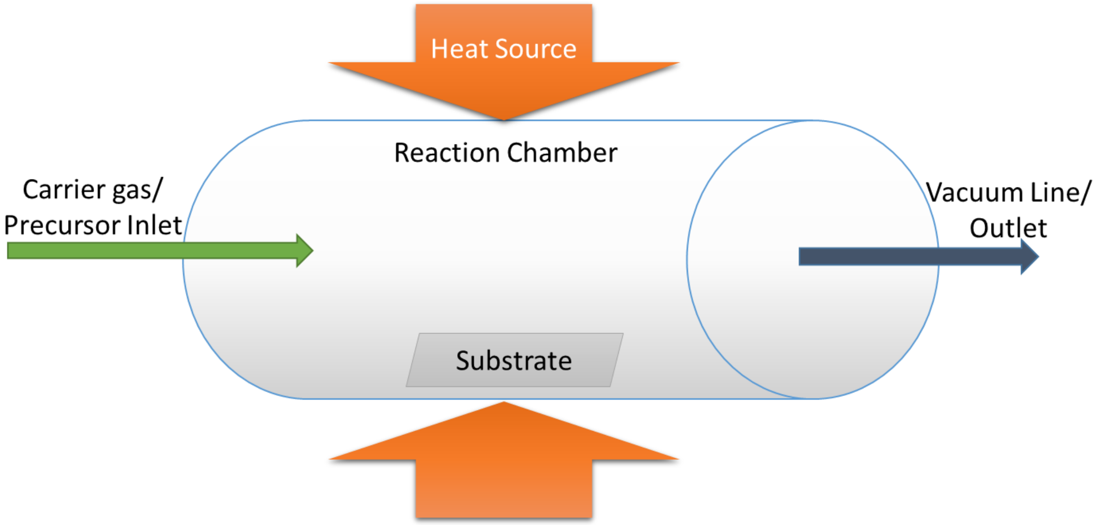

CVD is commonly used in the microelectronics industry due to its generally high throughput. However, gas phase precipitation and pyrolysis can lead to the incorporation of impurities in the films, causing defects and non-conformal growth. This undesired effect is more pronounced at thicknesses below 20 nm, and leads to poor step coverage of high-aspect ratio features.[1-3, 19] In addition, the high temperatures required in many CVD processes are incompatible with microelectronic device manufacturing, due to the potential for component damage.

1.2.3 Atomic Layer Depostion (ALD)

CVD and PVD have limited practicality when coating high-aspect ratio features at the sub-20 nm scale due to the non-conformal film growth that results from gas phase reactions.[20-21] Therefore, a more advanced process is required to continue the miniaturization trend in microelectronics past the 20 nm scale.[1-4] Atomic layer deposition

(ALD) allows for precise thickness control and highly conformal thin film growth necessary for manufacturing features at this scale and smaller (**Figure 6**).[1-3, 19]

Figure 6. High-aspect ratio features (≤ 20 nm) coated by PVD/CVD and ALD.

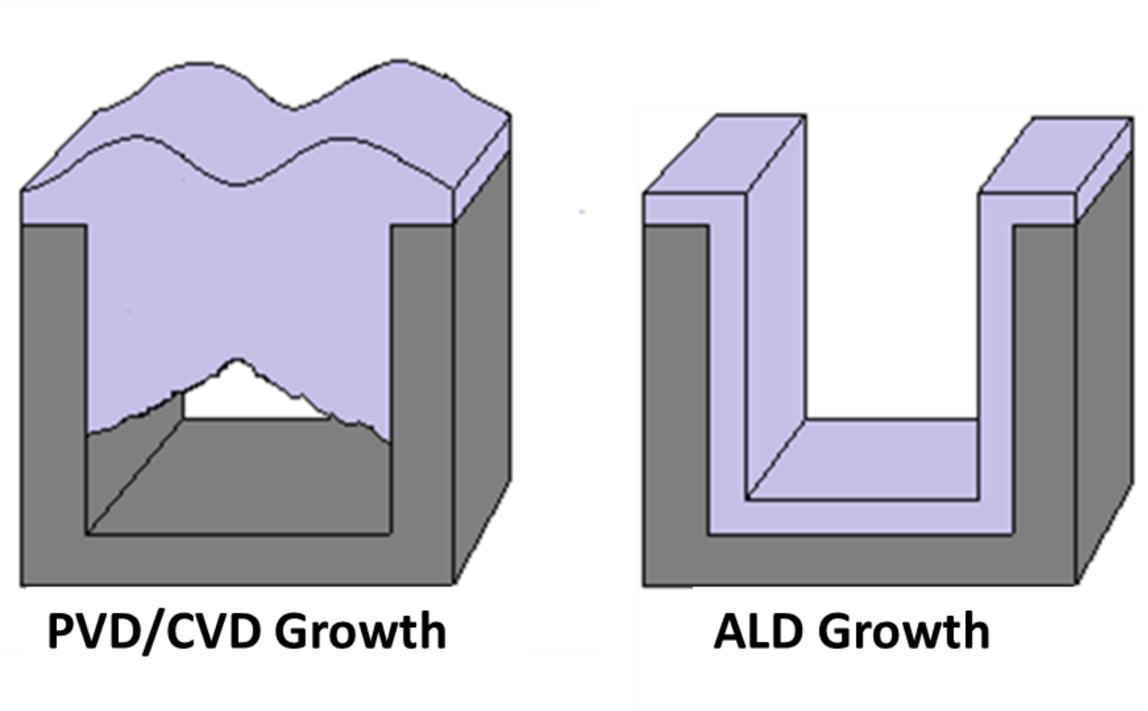

Unlike CVD, where high temperatures result in uncontrolled decomposition growth, ALD processes are defined by a self-limited growth mechanism, where depositions are carried out below the thermal decomposition temperature threshold of the precursors. The hallmark of ALD growth is exhibited by the saturation curve (**Figure 7**),[3] where a plot of growth rate versus precursor pulse length eventually plateaus. A constant growth rate occurs beyond when the precursor has reacted with all available surface reactive sites (this is called the saturative dose). If the precursor is thermally stable at the deposition temperature, no further film growth can occur once the minimum surface saturative dose has been delivered.

Figure 7. General saturation curve for an ALD process. Region 1 indicates sub-saturative growth, while region 2 indicates saturative growth.

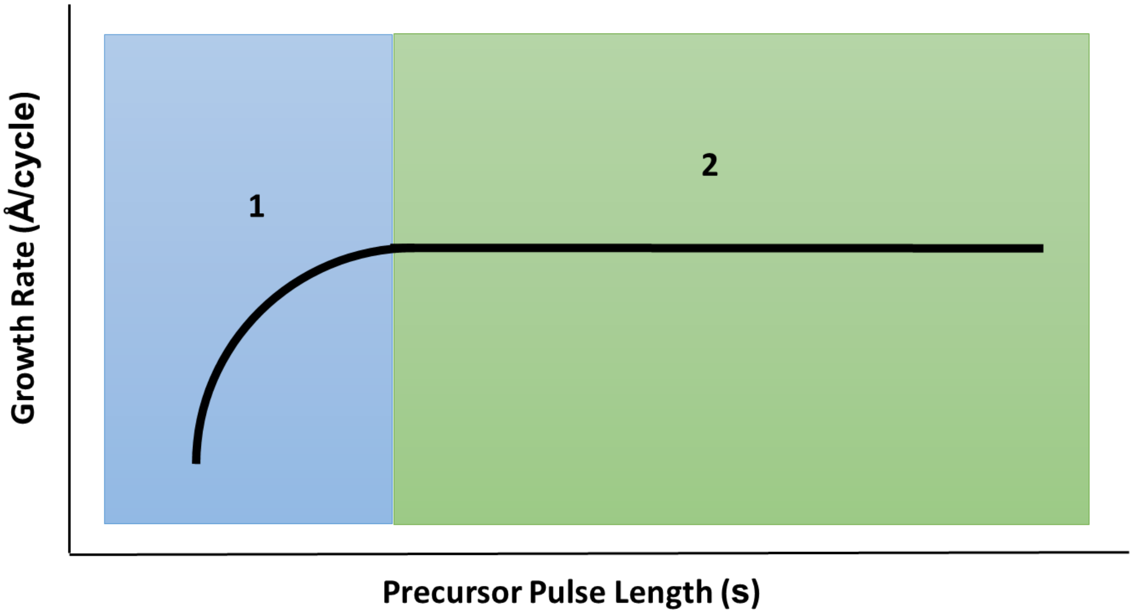

Many ALD growth processes also demonstrate a region where the growth rate is independent of substrate temperature (**Figure 8**). The temperature range where chemisorption of the precursor to the substrate is optimal results in self-limited growth, affording a constant growth rate, is called the ALD window. The ALD window, which can range from a few degrees to over one hundred, and is unique to the deposition process.[3]

Figure 8. General ALD window. The various regions depict insufficient reactivity (solid line, region 1), precursor condensation (dashed line, region 1), the ALD window (region 2), surface deactivation (dashed line, region 3) and precursor self-decomposition (solid line, region 3).

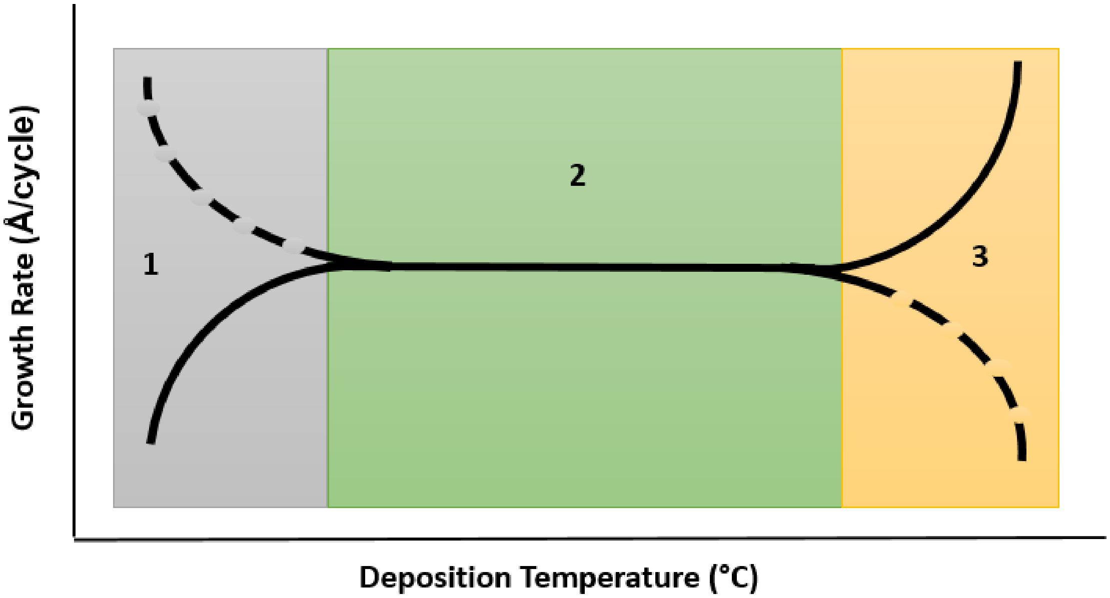

The final characteristic of an ALD process is that the film thickness usually increases linearly with the number of cycles (**Figure 9**).[3] When plotted, the slope of this line indicates the saturative growth rate, while the extrapolated y-intercept gives insight into potential nucleation issues (for ideal processes, the intercept is the origin). Linear growth with increasing number of cycles allows for precise control over film thickness. These properties make ALD well suited as the primary deposition technique for the manufacturing of continually minimizing microelectronic device components.[1-3, 19]

Figure 9. General thickness *versus* number of cycles plot. Normal ALD growth proceeds in a linear fashion, and can be described using the equation y = mx +b. The slope, or "m," is the growth rate for the process. The y-intercept of the graph, or "b," should ideally be zero.

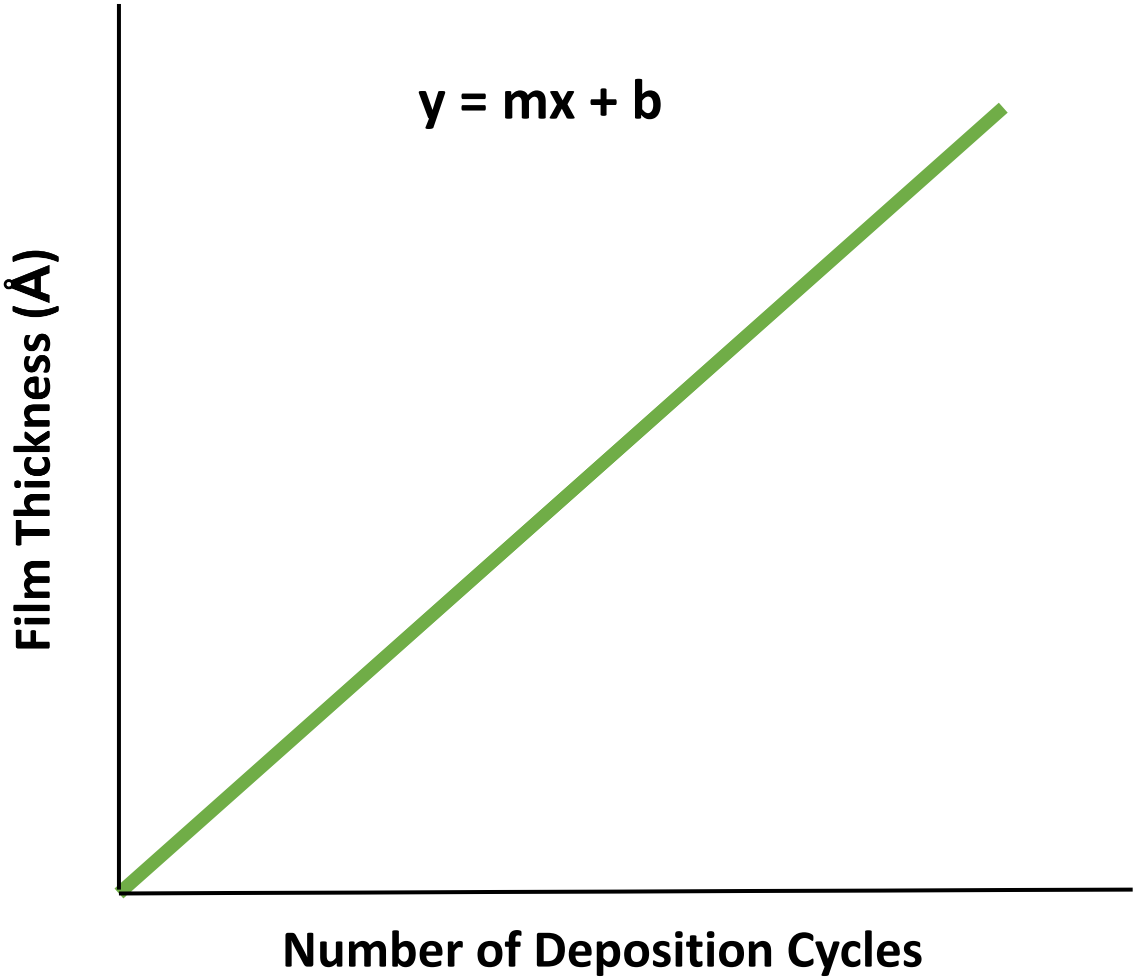

The four-step ALD cycle creates a self-limiting growth mechanism that enables precise thickness and highly conformal growth (**Figure 10**).[1-3] In the first step, the first precursor is pulsed into the reaction chamber, where it reacts with or adsorbs on the substrate surface until the surface reactive sites are exhausted, forming a single monolayer. An inert gas is then pulsed into the chamber to remove any excess precursor and reaction products. After the inert gas purge, a second precursor is pulsed into the chamber, reacting with the newly formed monolayer to form a monolayer of the desired material. Another inert gas purge is then performed and the process is repeated until the desired film thickness is achieved. Since the growth rate per cycle is constant, the film thickness can be precisely controlled by varying the number of cycles.[1-3]

Figure 10. General ALD cycle.

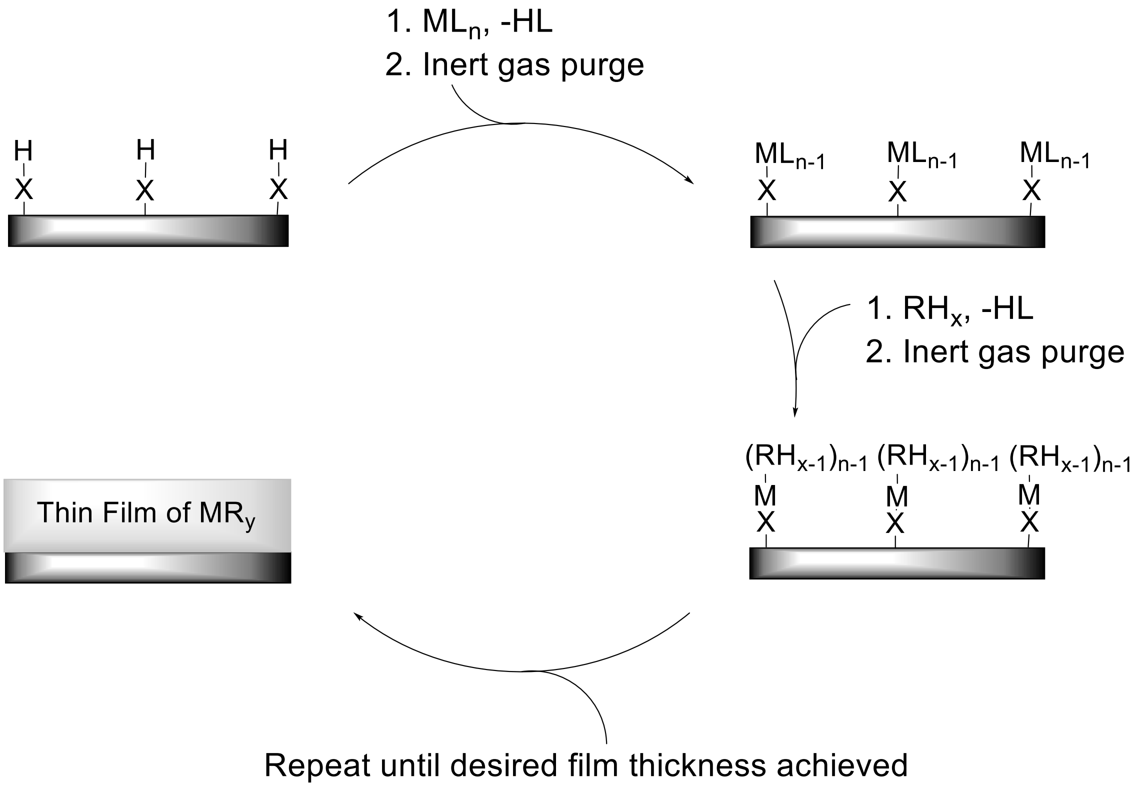

For best results, ALD precursors should have the following properties: high volatility to allow rapid introduction into the reaction chamber, high thermal stability to avoid CVD-like decomposition growth, high reactivity toward the second reducing co-reagent at the deposition temperature, rapid reactivity with surface reactive sites, and the ability to form volatile reaction products to afford high purity materials. Many CVD precursors are not thermally stable at deposition temperatures, making them suitable for decomposition reactions.[3] Decomposition reactions of the precursors are undesirable in ALD, since these reactions may result in loss of self-limiting growth and higher impurity incorporation is possible. A lack of suitable precursors available with all desired properties necessitates the need for the development of new ALD precursors and processes to allow for industrial-scale application of ALD.[3]

The two main methods of ALD processes are thermal ALD and plasma-enhanced (PEALD). Thermal ALD uses a heated reaction chamber, in which film growth driven by thermodynamics occurs.[3] PEALD uses plasma species as co-reactants in the deposition process. These plasma species are highly-reactive, high-energy radicals, with H_2, N_2, NH_3, and O_2 used as common sources.[20-22] An advantage of using PEALD is that it can enhance the reactivity of precursors at much lower temperatures than CVD.[20-22] However, plasma processes often give poor conformal coverage due to hydrogen atom recombination on the surface of the substrate, and can damage the substrates.[3, 22] Thermal ALD alleviates the problems posed by PEALD, but few processes are reported for the first-row transition metals, with many occurring above the precursor decomposition temperature (leading to CVD-like growth).

1.2.4 Area-Selective ALD

Another challenge in device manufacturing is substrate-selective deposition.[23] Substrate-selective ALD is a technique where the desired thin film preferentially grows on one type of substrate surface over another (**Figure 11**). Substrate-selective growth is receiving attention in the fabrication of microelectronic devices, since deposition on only the intended portion of a device surface can eliminate complicated etching steps from the fabrication process and minimize expensive and poisonous reagent use.[23]

Figure 11. Comparison of normal ALD growth to substrate-selective ALD growth.

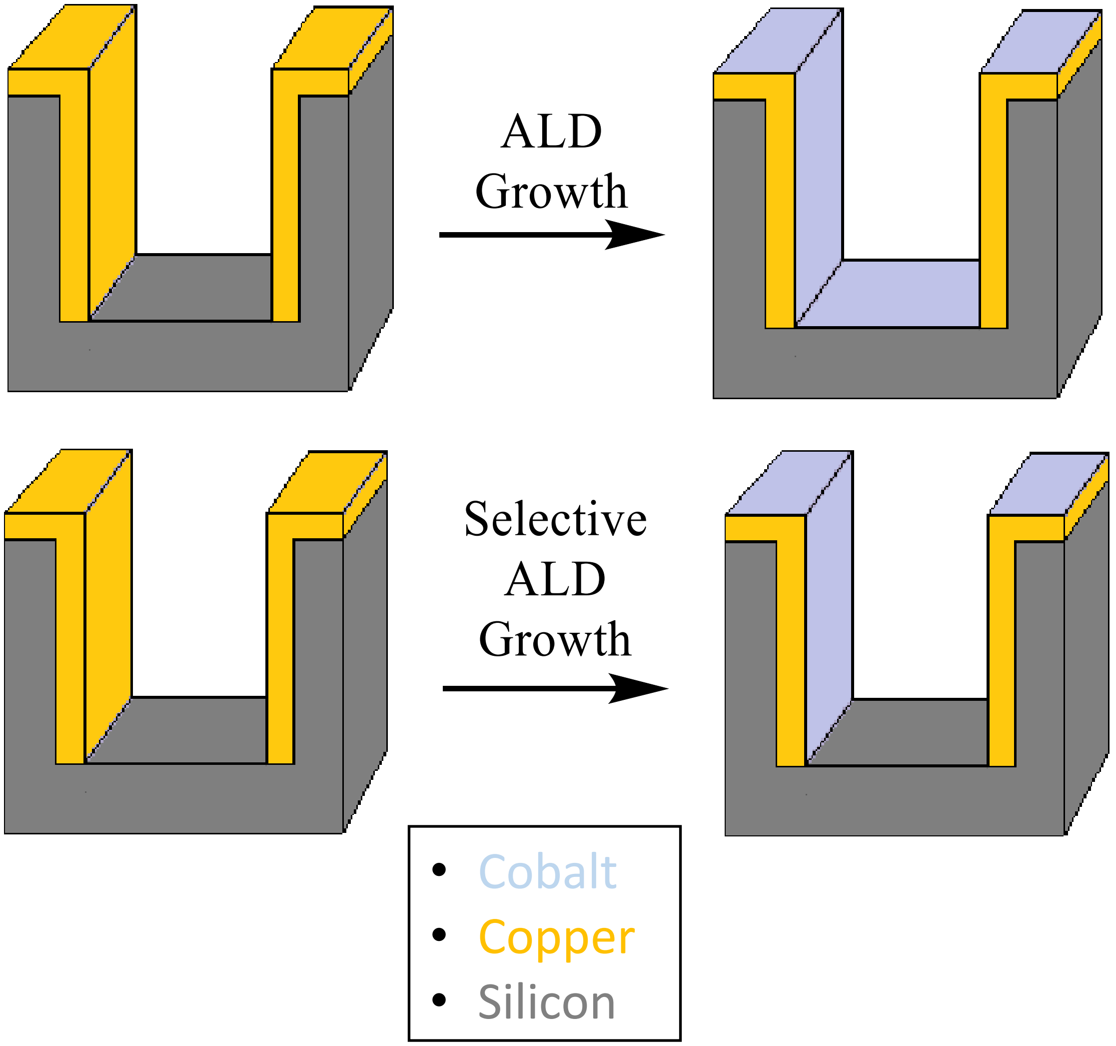

Despite the considerable interest, there are few reported processes for substrate-selective growth, especially for selective growth of metallic thin films. Selectivity can be achieved by tailoring the surface chemistry of the precursor and substrate, such as fluorinating the substrate surface to inhibit growth, using hydrogen to inhibit growth, and using spontaneously adsorbing molecular assemblies, as known as self-assembled monolayers (SAMs), as blocking layers.[23] These methods have been demonstrated to grow metals selectively on desired substrates. Selectivity can also be inherent to a process, where the precursor chemistry only occurs with certain substrates to deposit films.[23] In a recent publication from Bent and co-workers, partial fluorination of the horizontal surfaces of a silicon fin array nanostructure surface using the hydrophobic interactions of CF_x was used to inhibit growth. This led to platinum ALD growth observed only on the non-fluorinated surfaces (sidewall surfaces) for up to 500 growth cycles.[24] Parsons and co-workers demonstrated selective growth of tungsten metal thin films using WF_6 and SiH_4, with hydrogen during the tungsten precursor pulse to inhibit growth on SiO_2 without affecting tungsten metal growth on silicon substrates.[25] The most commonly reported substrate-selective depositions make use of (SAMs) as blocking layers,[26-31] which have been demonstrated to grow selectively metals on desired substrates. An example of the use of SAMs for substrate-selective growth of metallic thin films is the work by Leskelä and co-workers.[30] Octadecyltrimethoxysilane was employed to form SAMs on oxide substrate surfaces, to block the growth of iridium thin films, using $Ir(acac)_3$ (acac = 2,4-pentadione) and O_2 at 225 °C, for 1000 growth cycles.

Selectivity can also be inherent to a process where the precursor chemistry only proceeds to afford films on certain substrates.[23, 32-34] Using the copper precursor $Cu(tmhd)_2$ (tmhd = 2,2,6,6-tetramethylheptane-3,5-dionate) and H_2, metallic copper thin films were selectively deposited on palladium surfaces over SiO_2 and Si_3N_4 surfaces for 100 deposition cycles, at 135 – 230 °C.[32] Understanding the growth process in the initial stages is essential to the development of selective deposition processes. More exploration into selective processes is necessary, with few processes reported to date.

1.3 Applications and Challenges of the ALD of Transition Metal Containing Thin Films

ALD of the first-row transition metals is of great interest due to the relative abundance and inexpensive cost in comparison to the noble metals, and the many current and future applications of these metals (**Table 1**).[3, 20, 35-53] Copper is widely used as the replacement for aluminum interconnects in microelectronic devices.[3-5] Since copper poorly nucleates on SiO_2 and other dielectric materials, seed layers for the adhesion of copper are necessary.[3-5] The use of chromium and cobalt as seed layers for copper adhesion has been employed.[13] Copper also has a tendency to diffuse into SiO_2 and silicon at device fabrication temperatures.[3-5] The diffusion of copper into these substrates necessitates a barrier layer to prevent diffusion.[3-5] Manganese is being explored for use as a replacement for TaN as a diffusion barrier layer for copper features.[3, 46] Koike and co-workers have reported the use of a PVD sputtered copper/manganese alloy deposited on SiO_2, then annealed at 250 – 450 °C, as a self-forming copper diffusion barrier.[46-48] Upon annealing the copper/manganese alloy, the manganese atoms in the alloy migrated toward the SiO_2 interface, forming a 2 – 8 nm thick $MnSi_xO_y$ layer.[46-48] This $MnSi_xO_y$ layer served as a diffusion barrier in between the copper and SiO_2 layers, which maintained integrity for 100 h at 450 °C.[47] Deposition by PVD methods has limitations (*vide supra*) which can be alleviated by depositing the copper/manganese alloy by thermal ALD. Winter and co-workers have reported a process where layers of copper/manganese/copper were deposited on SiO_2 by thermal ALD, with the migration of the manganese atoms toward the SiO_2 layer was observed.[49] These results show promise of the self-forming $MnSi_xO_y$ barrier layer by ALD. Nickel, cobalt, and iron are useful in applications requiring magnetic materials, such as magnetoresistive random access memory (MRAM).[3] Films containing titanium, such as Ti/TiN, are used as liners to prevent the diffusion of copper into dielectric materials.[20] Films containing titanium oxides have also been explored for use in lithium ion battery development recently.[50] Vanadium oxide films have received attention for the wide scope of applications in catalysis, electrochromic devices, and solid-state batteries.[51-53]

Table 1. Applications and electrochemical potentials of first row transition metals in microelectronic devices.[3, 20, 35-54]

Element	**Reduction**	**E° (V)**	**Uses**
Cu	$Cu^{2+} + 2e^{-} \rightleftharpoons Cu^{0}$	**0.3419**	**Interconnects**
Ni	$Ni^{2+} + 2e^{-} \rightleftharpoons Ni^{0}$	**–0.257**	**Contacts, electrodes, magnetic materials**
Co	$Co^{2+} + 2e^{-} \rightleftharpoons Co^{0}$	**–0.280**	**Cu diffusion barrier, liner and cap for Cu, magnetic materials, $CoSi_2$ contacts**
Fe	$Fe^{2+} + 2e^{-} \rightleftharpoons Fe^{0}$	**–0.447**	**Magnetic materials**
Mn	$Mn^{2+} + 2e^{-} \rightleftharpoons Mn^{0}$	**–1.185**	**Self-forming Cu diffusion barriers**
Cr	$Cr^{2+} + 2e^{-} \rightleftharpoons Cr^{0}$	**–0.913**	**Cu seed layers**
V	$V^{2+} + 2e^{-} \rightleftharpoons V^{0}$	**–1.175**	**Catalysts, electrochromic materials, solid-state batteries**
Ti	$Ti^{2+} + 2e^{-} \rightleftharpoons Ti^{0}$	**–1.630**	**Cu diffusion barrier, solid-state batteries**

Deposition by ALD enables thin films with the uniform thickness and high conformality necessary for these device components. However, many current first row transition metal precursors do not have all of the necessary properties for an ALD precursor, making the growth of these films challenging. To achieve high purity in metal films, precursors must be highly reactive towards a reducing co-reagent. The challenge posed by current transition metal precursors is their low reactivity towards common reducing co-reagents at deposition temperatures.[3] This difficulty stems from the negative electrochemical potentials of M(II) to M(0) (M = Ti, V, Cr, Mn, Fe, Co, Ni), as displayed in **Table 1**.[54] Additionally, the precursors must be thermally stable at the deposition temperature or CVD-like decomposition growth may occur. Due to the low reactivity of the current metal precursors toward available reducing agents, many depositions require high temperatures, resulting in CVD-like growth. These difficulties necessitate the development of new ALD processes, using reducing co-reagents that are more reactive toward the transition metal precursors. The body of this work will focus on the development of substrate selective ALD processes for cobalt and nickel metal in view of their many current and future applications.

1.3.1 Applications and Current ALD Processes for Cobalt Metal

Cobalt metal thin films have received increased interest in recent years due to the many applications, such as magnetic materials,[36] precursors to $CoSi_2$ contacts,[37] and interconnect materials (as a possible replacement for copper)[44] in many future applications that require components to be < 10 nm.[8] The drive to decrease dimension size for these features will require ALD growth of cobalt metal. Additionally, cobalt metal can be used as a material for the liners and caps of copper features in microelectronics devices,[38-42, 45] with the cobalt liners serving as seed layers for copper growth and the cobalt caps preventing the electromigration of copper. In order for cobalt metal to be used in this capacity, selective deposition of cobalt on copper is essential.

The growth of cobalt metal thin films by CVD processes has been extensively explored.[39, 55-67] The precursor μ^2-η^2-(^{t}Bu-acetylene)Co(CO)$_6$ (CCTBA) and H_2 have been used to deposit cobalt metal thin films by CVD at 150 °C to afford low resistivity (32.0 μΩ cm) cobalt metal films, however, high carbon and oxygen contamination was observed.[61] A recent report used the precursor $(C_5H_5)Co(\eta^4\text{-}CH_2CHC(Me)CH_2)$ and H_2 at 400 °C to deposit cobalt metal by CVD.[61] Although these films were high-purity cobalt metal, the surface roughness was high.[66] CVD growth has also been employed for the selective deposition of metallic cobalt films on precleaned-copper patterned wafers, which also contained dielectric surfaces, using cobalt carbonyl precursors.[39, 67] Many of the precursors (**Chart 1**) used in CVD contain one or more carbonyl group, making them impractical for use as ALD precursors. The low thermal energy required to remove carbonyl groups from molecules, results in the thermal decomposition of the precursor and high carbon and oxygen contamination of the deposited films,[68] which is undesirable for ALD processes. Although deposition of cobalt metal films by CVD has been well developed, the drive for microelectronic device miniaturization (< 10 nm) requires cobalt thin films to be deposited by ALD to meet size standards for future uses.

Chart 1. Examples of common cobalt precursors for thin film depositions.

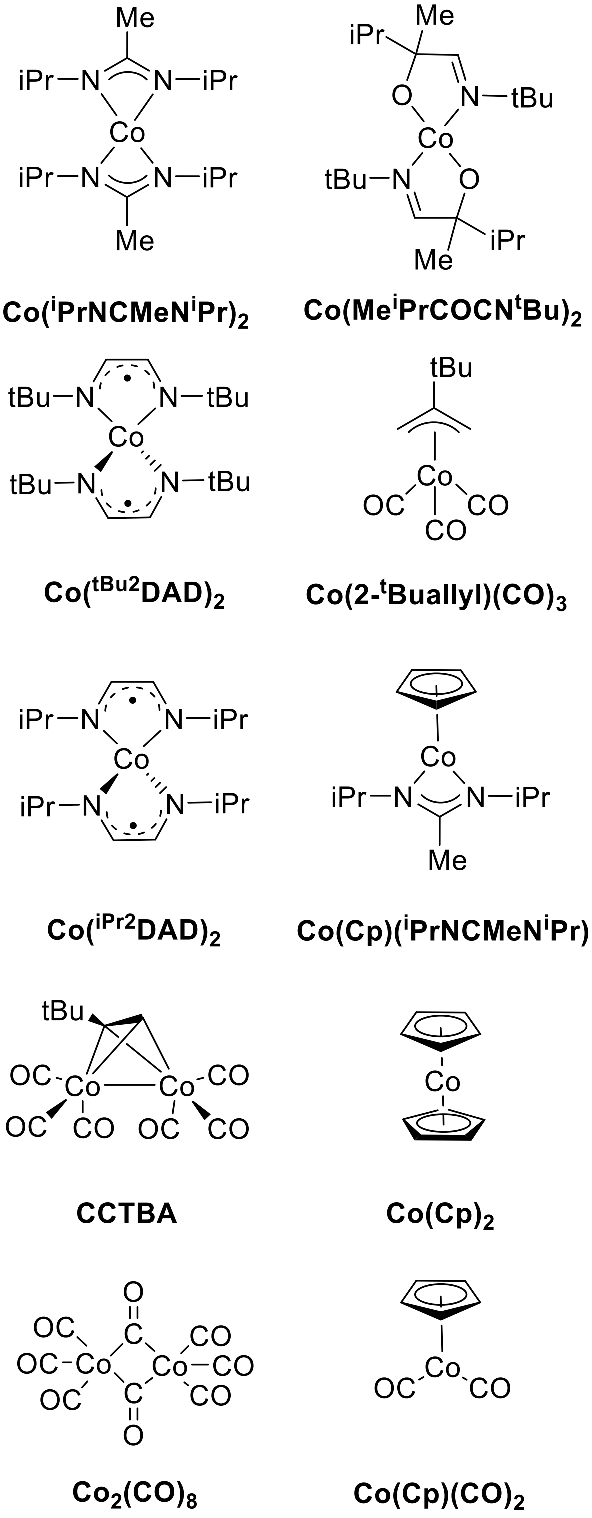

Co(^{i}PrNCMeN^{i}Pr)$_2$

Co(Me^{i}PrCOCN^{t}Bu)$_2$

Co(^{tBu2}DAD)$_2$

Co(2-^{t}Buallyl)(CO)$_3$

Co(^{iPr2}DAD)$_2$

Co(Cp)(^{i}PrNCMeN^{i}Pr)

CCTBA

Co(Cp)$_2$

Co$_2$(CO)$_8$

Co(Cp)(CO)$_2$

PEALD processes for the deposition of cobalt metal thin films have been reported.[68-75] The use of the precursor $Co(Cp)(CO)_2$ with various plasma species has been reported numerous times for PEALD growth of cobalt metal thin films.[68, 72, 74-75] The use of NH_3 plasma at 150 – 300 °C to afford thin films of cobalt metal, had the highest purity, and the lowest film resistivities (~20 μΩ cm) of these processes.[68] Saturative behavior for the precursors was not observed, suggesting that CVD growth is likely for this process, with the thermal decomposition of 150 °C reported for $Co(Cp)(CO)_2$.[72] The purity of the deposited cobalt metal films was further increased, with a decrease in resistivity observed (~10 μΩ cm) for the PEALD process using $CoCp_2$ and NH_3 plasma, however, the conformality of these films was poor.[68, 74] PEALD cobalt film processes were also reported using the precursors $Co(MeCp)_2$,[69] $Co(Cp)(^{i}PrNC(Me)N^{i}Pr)$,[71] $Co_2(CO)_8$,[72-73] and CCTBA,[76] with all of these processes suffering from high resistivities (90 – 140 μΩ cm) resulting from high carbon and oxygen contamination. The use of PEALD improved the quality of the films, in comparison to analogous CVD processes, by decreasing the impurities (from unremoved ligands) and therefore decreasing the resistivity of the films.[76] However, *vide supra*, thermal ALD is preferred in the industrial manufacturing of these thin films.

The cobalt amidinate precursor, $Co(^{i}PrNCMeN^{i}Pr)_2$, has been employed in several thermal ALD processes for the deposition of cobalt metal.[26, 28, 77-81] $Co(^{i}PrNCMeN^{i}Pr)_2$ has a reported decomposition temperature of 215 – 225 °C.[80] In deposition processes reported for the growth of cobalt metal by ALD using $Co(^{i}PrNCMeN^{i}Pr)_2$ and H_2 or NH_3 as co-reactants, the deposition temperatures were 300 – 350 °C, with a low growth rate of 0.12

Å/cycle, and a high resistivity of 46 μΩ cm (compared to bulk cobalt resistivity of 6.24 μΩ cm[82]). [50-54] This process was also used for selective growth of cobalt metal for as many as 1000 growth cycles, implementing octadecyltrichlorosilane (OTC) as a blocking layer.[26] The OTC layer was selectively grown on Si(001) surfaces, to prevent growth on Si(001) surfaces in favor of growth on SiO_2 surfaces.[26] $Co(^iPrNCMeN^iPr)_2$ coupled with NH_3 plasma at 350 °C was also attempted for the selective growth of cobalt metal, however, the plasma was found to deteriorate the OTC layer, preventing selective growth.[28] These reported processes have deposition temperatures well above the cobalt precursor decomposition temperature. A CVD component to the film growth is likely, despite the observed saturation of $Co(^iPrNCMeN^iPr)_2$.

Selective deposition of cobalt metal on Si-H substrates over SiO_2 substrates was reported employing Co(2-*tert*-butylallyl)$(CO)_3$ and 1,1-dimethylhdrazine as co-reactants at a deposition temperature of 140 °C.[83] However, no data to support precursor saturation were reported for this process. Cobalt metal has also been deposited with $Co(Me^iPrCOCN^tBu)_2$ and $BH_3(NHMe_2)$ at the deposition temperature of 180 °C.[84] Although saturation for the precursors was reported, which confirmed self-limiting growth by this process, film growth only occurred on ruthenium substrates after a nucleation period, with no further growth seen after 1,000 deposition cycles.[84] This process also suffers from a low growth rate of 0.07 Å/cycle.[84]

Few thermal ALD processes have been reported to date, with many occurring above the precursor decomposition temperature, which suggests that these processes have large CVD-growth components to them. Operating above the thermal decomposition temperature of the precursor can also result in impurities incorporated into the films, which in turn can result in defects and higher resistivities. These risks make processes with large CVD-growth components undesirable for industrial manufacturing.

1.3.2 Applications and Current ALD Processes for Nickel Metal

Nickel metal thin films have applications in microelectronic devices as electrodes and contacts in transistors,[85] as a precursor material for NiSi and $NiSi_2$,[85] and as seed layers for copper deposition.[86] Nickel metal CVD has employed several nickel precursors (**Chart 2**) toward the deposition of nickel metal films. Nickel metal CVD has been achieved by the pyrolysis of $Ni(Cp)_2$ at $\geq$ 550 °C.[87] The pyrolysis of $Ni(dmamp)_2$ at $\geq$ 250 °C has also been employed to deposit nickel metal by CVD.[88] The use of $Ni(MeCp)_2$ with H_2 as a co-reactant for the CVD of metallic nickel films was attempted at 300 °C, but the deposited nickel film reacted with the silicon substrate to produce a mixture of NiSi and $NiSi_2$ films instead.[85] Although nickel metal films with high-purity and low resistivity were obtained, as discussed previously, many future applications will require components to be < 10 nm. CVD growth has limited ability to coat features conformally at this size, which calls for ALD growth of nickel metal.

Chart 2. Examples of common nickel precursors for thin film depositions.

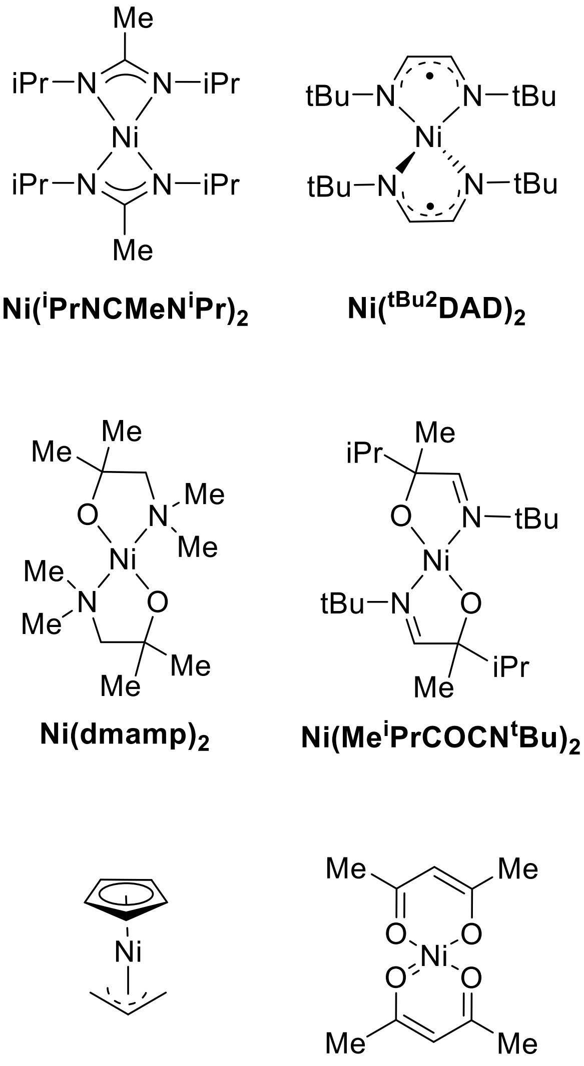

Ni(^{i}PrNCMeN^{i}Pr)$_2$

Ni(^{tBu2}DAD)$_2$

Ni(dmamp)$_2$

Ni(Me^{i}PrCOCN^{t}Bu)$_2$

Ni(Cp)allyl

Ni(acac)$_2$

Metallic thin films of nickel were deposited *via* PEALD by employing the precursor Ni(dmamp)$_2$ along with NH_3 or H_2 plasma as co-reactants at 250 °C.[89] The growth rates reported for these processes are 2.0 Å/cycle with the use of NH_3 plasma, and 0.8 Å/cycle with the use of H_2 plasma. The PEALD of nickel metal using Ni(dmamp)$_2$ and H_2 plasma at 220 °C was also reported, with a growth rate of 1.55 Å/cycle.[90] Although these plasma processes produce nickel metal thin films with high growth rates, thermal ALD is the preferred method for industrial manufacturing.

Indirect thermal ALD processes for the growth of metallic nickel metal films have been reported. These processes used the deposition of NiO, with the subsequent reduction of NiO to nickel metal by either H_2 plasma reduction[86] or annealing at high temperatures under forming gas.[91] These methods are less desirable than a direct thermal ALD process for nickel metal due to the use of plasma and high annealing temperatures, which can damage device components during manufacturing.[3, 22]

Nickel metal thermal ALD was reported using $Ni(^iPrNCMeN^iPr)_2$ and H_2 at a deposition temperature of 250 °C.[81] $Ni(^iPrNCMeN^iPr)_2$ has a reported decomposition temperature of 180 °C.[77] CVD-like film growth is likely despite the observed saturation of $Ni(^iPrNCMeN^iPr)_2$, similar to the analogous cobalt process reported using $Co(^iPrNCMeN^iPr)_2$, considering the deposition temperature is well above the decomposition temperature of the precursor. The precursor $Ni(Me^iPrCOCN^tBu)_2$ and $BH_3(NHMe_2)$ were employed toward the ALD growth of nickel metal at the deposition temperature of 180 °C.[84] Although saturation for each precursor was reported (which confirmed self-limiting growth by this process), film growth only occurred on ruthenium substrates after a nucleation period, with no further growth seen after 1,000 deposition cycles (as seen with the analogous process for cobalt metal). With few direct nickel metal thermal ALD processes available, new processes for nickel metal are desirable.

1.4 Thesis Objective

The overall objective of this research was to develop new processes for the selective deposition of first row transition metal thin films by ALD, with a focus on cobalt and nickel metal. Suitable ALD precursors were identified to complete this goal, and then in-depth deposition studies were performed. Once high quality ALD processes were developed for metallic thin films, substrate-selective deposition studies were carried out. Resultant films were analyzed by scanning electron microscopy (SEM), energy dispersive spectroscopy (EDS), powder X-ray diffractometry (PXRD), atomic force microscopy (AFM), X-ray photoelectron spectroscopy (XPS), and four-point-probe resistivity measurements. The results herein describe the substrate selective deposition of metallic cobalt thin films by ALD for a recently developed process, using bis(1,4-di-*tert*-butyl-diaza-1,3-butadiene)cobalt, $Co(^{tBu2}DAD)_2$, and formic acid.[34, 82] Additionally, the use of alkyl amines as reducing co-reagents was demonstrated when reacted with $Co(^{tBu2}DAD)_2$ and bis(1,4-di-*tert*-butyl-diaza-1,3-butadiene)nickel, $Ni(^{tBu2}DAD)_2$, respectively, to give the corresponding metallic thin film by ALD. The substrate-selective deposition using alkyl amines as co-reagents for cobalt and nickel metal for these processes was also demonstrated.

CHAPTER 2 SUBSTRATE SELECTIVITY IN THE LOW TEMPERATURE, THERMAL ATOMIC LAYER DEPOSITION OF COBALT METAL THIN FILMS FROM BIS(1,4-DI-*TERT*-BUTYL-1,3-DIAZADIENYL)COBALT AND FORMIC ACID

Portions of the text in this chapter were reproduced from "Substrate selectivity in the low temperature atomic layer deposition of cobalt metal films from bis(1,4-di-tert-butyl-1,3-diazadienyl)cobalt and formic acid," Kerrigan, M. M.; Klesko, J. P.; Rupich, S. M.; Dezelah, C. L.; Kanjolia, R. K., Chabal, Y. J.; Winter, C. H. *The Journal of Chemical Physics,* **2017**, 146, 052813 with the permission of AIP Publishing permission. All rights to the work are retained by the authors and any reuse requires permission of the authors.

2.1 Introduction

Our group recently reported an ALD process for cobalt metal thin films using Co(^{tBu2}DAD)$_2$ and formic acid (**Figure 12)**.[82] This process exhibits saturative growth behavior, in the ALD window of 170 – 180 °C. The cobalt metal films were of high-purity (confirmed by XPS), with low resistivity of 13 – 19 $\mu\Omega$ cm, a high growth rate of 0.95 Å/cycle, and no growth on non-metallic surfaces.[82] This chapter describes the in-depth studies of the early stages of deposition of cobalt metal by ALD using Co(^{tBu2}DAD)$_2$ and formic acid on metallic and dielectric substrates.[34] Inherent selectivity has also been demonstrated for the growth of cobalt metal thin films on metallic substrates over dielectric substrates,[34] and will herein be described.

Figure 12. General reaction scheme for the ALD growth of cobalt metal from Co(^{tBu2}DAD)$_2$ and formic acid.

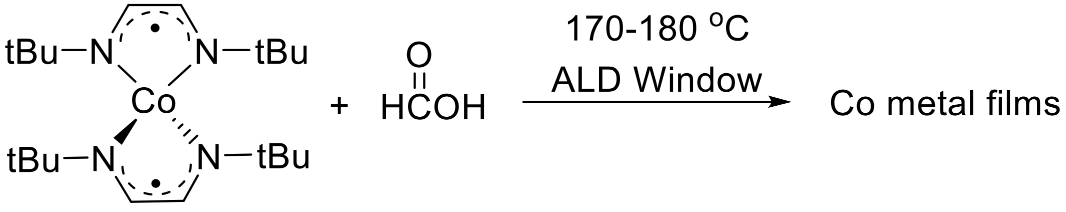

2.2 Results and Discussion

2.2.1 Film growth on ruthenium, platinum, and copper substrates

Figure 13 shows plots of thickness versus number of cycles for cobalt metal growth on ruthenium, platinum, and copper substrates at 180 °C for 25, 50, 100, 150, and 250 cycles using the growth conditions described in the experimental section, found at the end of this chapter. For both platinum and copper surfaces, the plots were linear with growth rates of 0.98 Å/cycle, with cross-sectional SEM revealing continuous films at all thicknesses (**Figure 14**). These values are within experimental error of the 0.95 Å/cycle growth rate that we reported for the $Co(^{tBu2}DAD)_2$ and formic acid process on ruthenium substrates between 250 and 2000 cycles and at 1000 cycles on platinum and copper substrates.[82] Cobalt films grown with 25 cycles (~2.5 nm thick) can be measured with our electron microscope, but these thickness values have higher uncertainties than measurements made of thicker films. Accordingly, the presence of cobalt on the substrates was also probed qualitatively by EDS for films grown with 25, 50, and 100 cycles. All samples grown on platinum and copper substrates showed cobalt signals in the EDS spectra (**Figure 15**). The fact that the growth rates on platinum and copper substrates with 25 to 250 cycles are identical to those observed from 250 to 2000 cycles on ruthenium substrates and at 1000 cycles on platinum and copper,[82] coupled with the observation of cobalt signals in all of the EDS spectra, implies that normal ALD growth occurs even at 25 cycles on platinum and copper substrates.

Figure 13. Plot of thickness versus number of cycles for cobalt metal growth on ruthenium, platinum, and copper substrates at 180 °C.

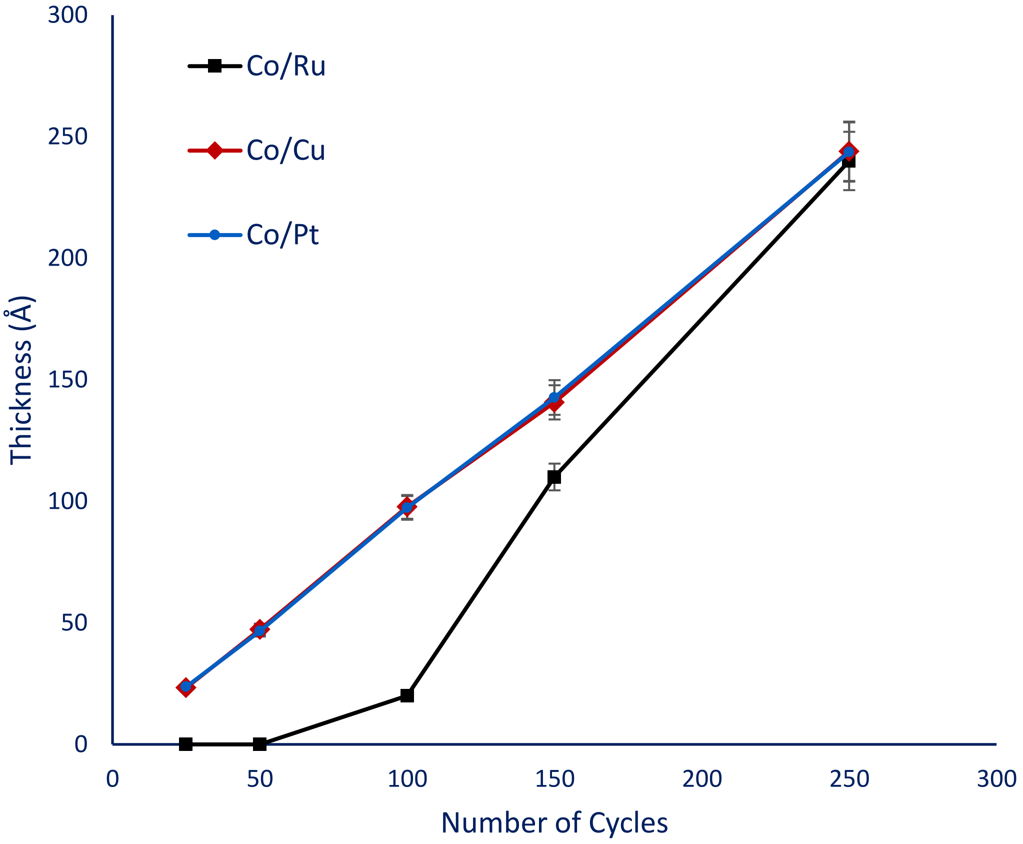

Figure 14. Cross-sectional SEM of a 14 nm thick cobalt metal film grown at 180 °C, on a) a platinum substrate b) a copper substrate.

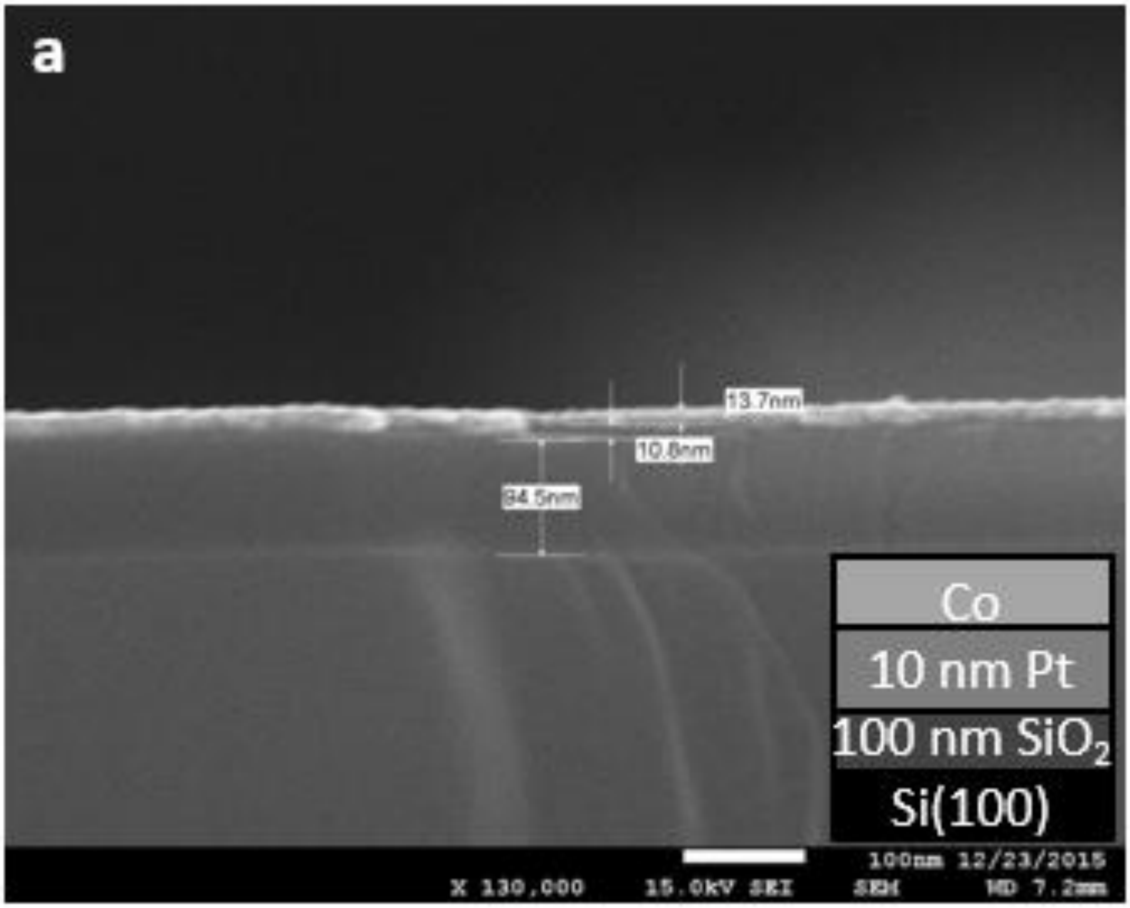

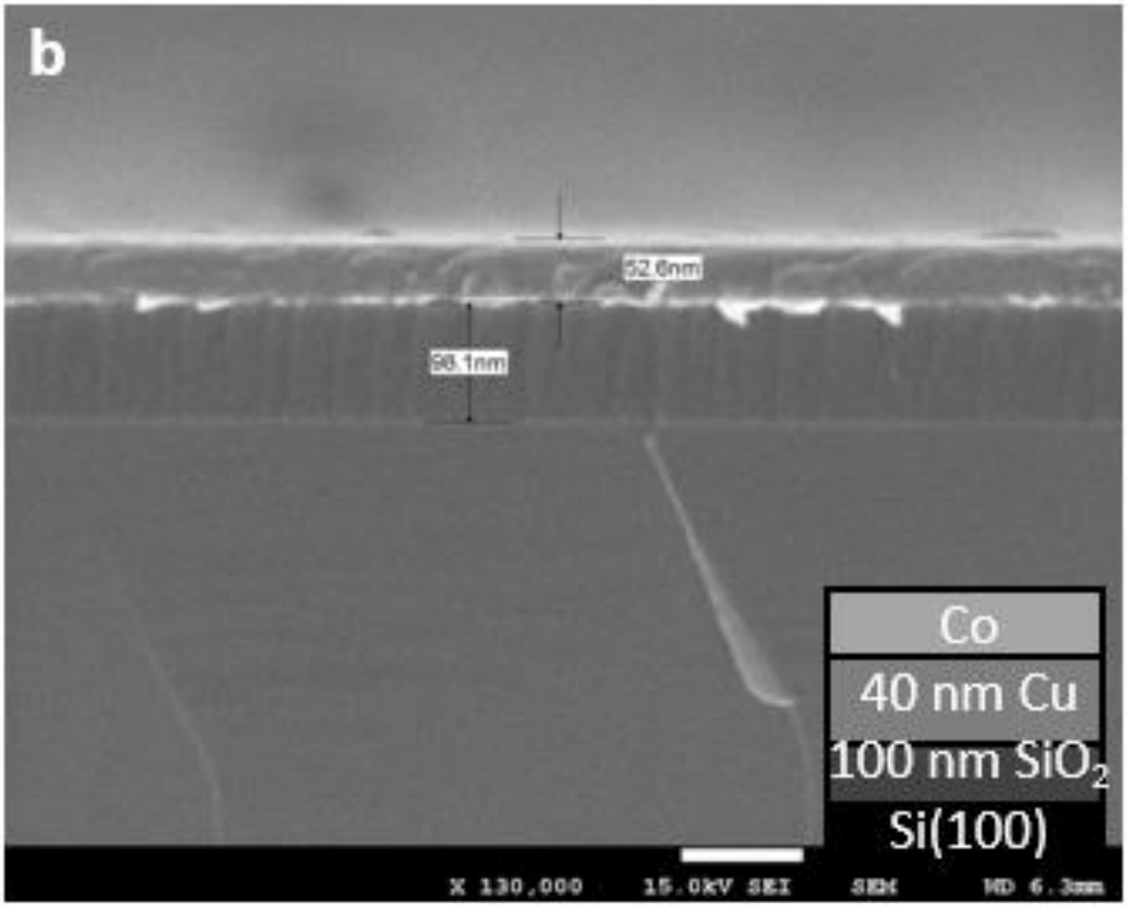
b
52.0nm
98.1nm
Co
40 nm Cu
100 nm SiO$_2$
Si(100)
X 130,000
15.0kV SEI
SEM
WD 6.3mm

Figure 15. EDS spectrum for 25 cycles (~2.5 nm) of cobalt metal grown at 180 °C, on a) a platinum substrate and b) a copper substrate.

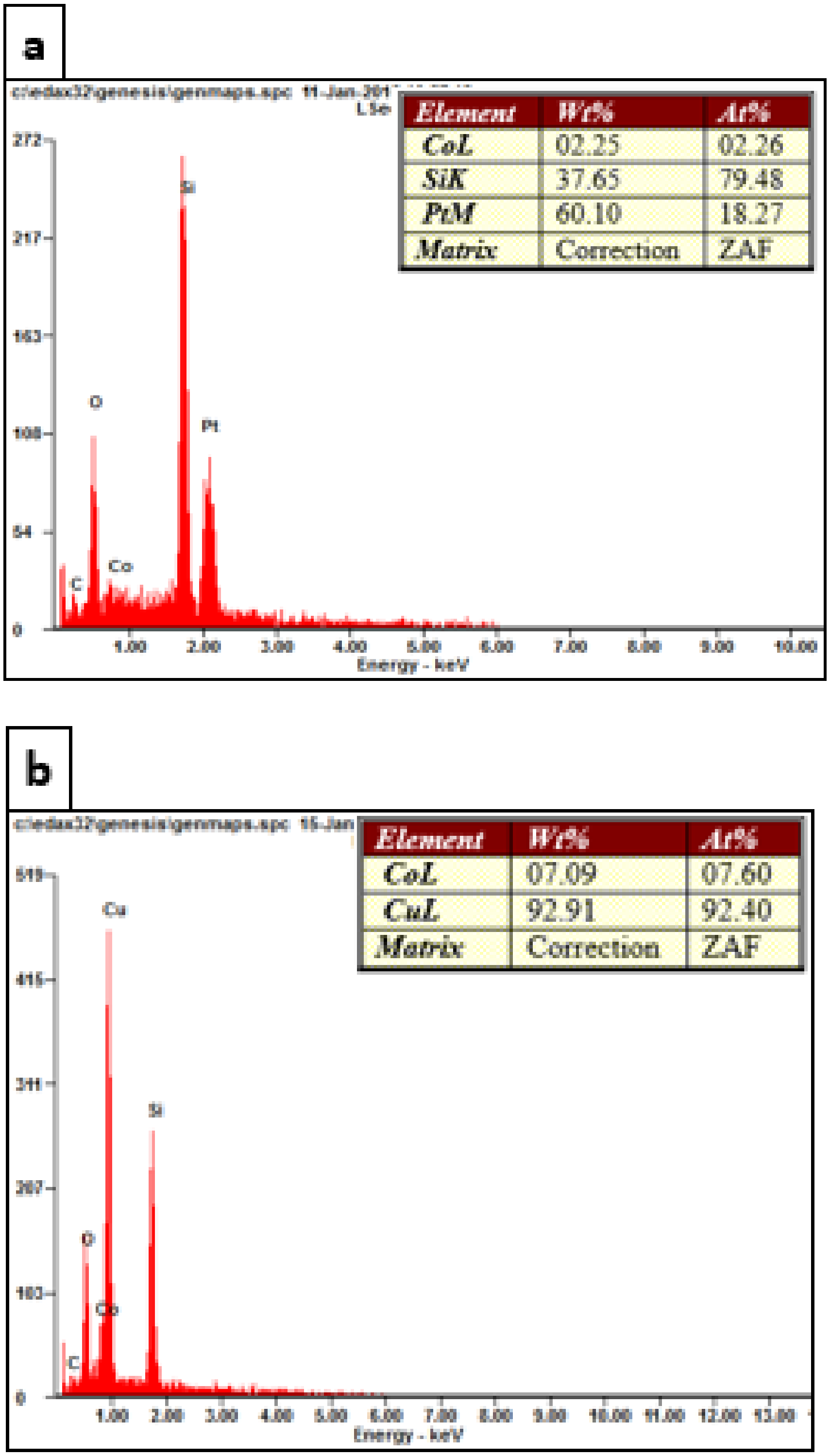

Element	Wt%	At%
CoL	02.25	02.26
SiK	37.65	79.48
PtM	60.10	18.27
Matrix	Correction	ZAF

Element	Wt%	At%
CoL	07.09	07.60
CuL	92.91	92.40
Matrix	Correction	ZAF

In contrast to the linear growth behavior on platinum and copper substrates, cobalt growth on ruthenium substrates showed a delay at 180 °C of up to 250 cycles before the saturative growth rate ensued, beyond which a linear plot of thickness versus number of cycles was observed with a normal growth rate of 0.95 Å/cycle.[82] No detectable film growth (< 2 nm) was observed by SEM after 25 and 50 growth cycles. After 100 cycles, a uniform thickness, ~2 nm continuous layer was observed by SEM. At 150 cycles, a ~10 nm thick cobalt film was observed. At 250 cycles and beyond, the normal 0.95 Å/cycle growth rate was obtained. Between 100 and 150 cycles on ruthenium substrates, the film thickness increased from ~2 nm to 10 nm, which corresponds to a growth rate of ~1.6 Å/cycle.[82] This value is much higher than the 0.95 Å/cycle growth rate observed between 250 and 2000 cycles on ruthenium substrates. In our previous paper, we reported that a CVD-like experiment conducted with $Co(^{tBu2}DAD)_2$ (5.0 s)/N_2 purge (10.0 s) and no formic acid pulses at 180 °C for 1000 cycles on a ruthenium substrate led to a film thickness of 13 – 15 nm.[82] For comparison, $Co(^{tBu2}DAD)_2$ undergoes thermal decomposition to cobalt metal in the solid state upon heating to ~235 °C, and should thus be thermally stable at 180 °C.[92] Accordingly, it appears that there is a nucleation delay of about 100 cycles in the ALD growth process, during which no cobalt growth is observed by SEM (< 2 nm). This delay may occur because of an oxidized ruthenium surface,[93] which could inhibit cobalt metal nucleation until treatment with $Co(^{tBu2}DAD)_2$ and formic acid can expose reactive surface sites. Between 100 and 150 cycles, the very high growth rate (~1.6 Å/cycle) suggests that the ruthenium/cobalt surface promotes the decomposition of $Co(^{tBu2}DAD)_2$ in a CVD-like fashion to afford a layer that covers the ruthenium surface (~10 – 15 nm).

Once the ruthenium surface is covered by a cobalt layer (150 – 250 cycles), normal self-limited ALD growth ensues. It is not fully clear why the growth behavior on ruthenium substrates is different than on platinum and copper substrates. However, nucleation in noble metal ALD processes is difficult, and many ruthenium ALD processes exhibit delays of up to several hundred cycles before normal growth ensues.[93] Factors that affect nucleation in noble metal ALD have been discussed and surface treatments can affect nucleation.[94] In the present work, the ruthenium substrates were used as received, and no pretreatments were carried out. Ruthenium surfaces are often oxidized,[93] which could affect cobalt metal nucleation. It is possible that various pretreatments of the ruthenium substrates could reduce or even eliminate the nucleation delay observed herein.

AFM was used to probe the surface topologies of films grown at 150 cycles (~14 nm thick) on platinum and copper substrates (**Figure 16**). On platinum (**Figure 16a**), the cobalt film had an rms surface roughness of 0.6 nm, compared to an rms surface roughness for the uncoated platinum substrate of 0.19 nm. This rms roughness corresponds to 4% of the film thickness, and indicating a very smooth film. **Figure 16b** shows the AFM image of the cobalt film on a copper substrate. The rms surface roughness for the full 2 x 2 μm^2 region was 2.4 nm, and was 1.1 nm for the inset showing a 0.7 x 0.7 μm^2 region that did not contain any surface particles. For comparison, the rms value of the uncoated copper substrate was 0.69 nm. The surface contains widely spaced 30 – 125 nm diameter particles, as well as 30 – 60 nm diameter pits. The particles and pits originate from the copper substrates, since the AFM image of the uncoated substrates shows similar features. These surface features may originate from surface oxidation of the copper by air.[95] While AFM studies of thin cobalt films on ruthenium substrates were not carried out because of the nucleation delay at early growth stages, a 105 nm thick cobalt film on a ruthenium substrate grown at 180 °C had an rms surface roughness of 0.98 nm, compared to a value of 0.42 nm for the uncoated ruthenium substrate.[82] Accordingly, films grown from $\mathrm{Co(^{tBu2}DAD)_2}$ and formic acid at 180 °C give very smooth films on ruthenium and platinum substrates. Films on copper substrates also have low rms surface roughnesses, although some pits and particles are observed due to the copper substrate.

Figure 16. AFM images of 15 nm thick cobalt metal film grown on a) platinum and b) copper. The inset shows a smooth region of the cobalt on copper film. Cobalt on platinum: rms = 0.6 nm. Cobalt on copper: rms = 2.4 nm, inset rms = 1.1 nm.

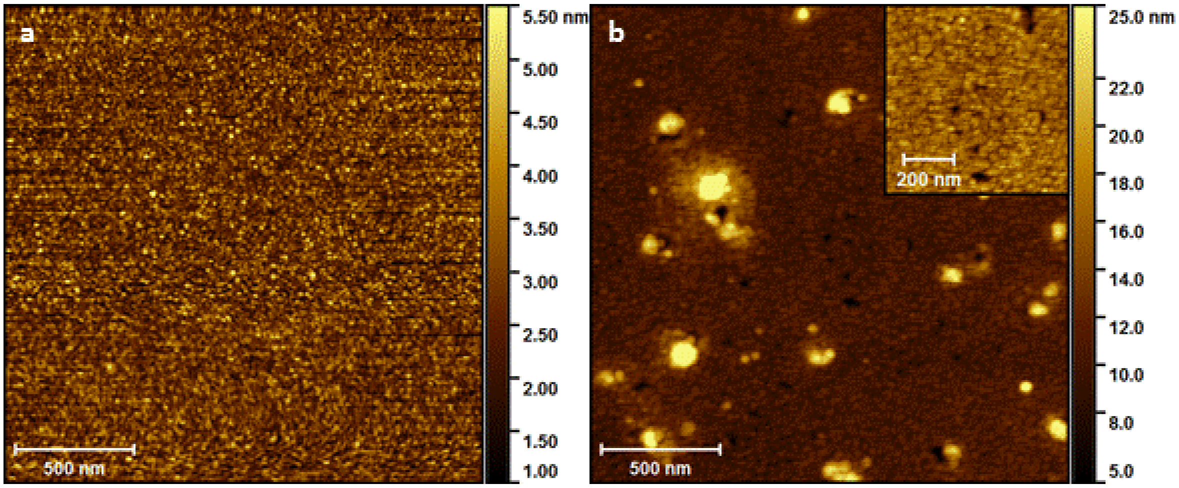

The resistivities of the films grown on ruthenium, platinum, and copper substrates were measured for samples grown from $\mathrm{Co(^{tBu2}DAD)_2}$ and formic acid at 180 °C with 25, 50, 100, 150, and 250 cycles (**Table 2**). On ruthenium, the resistivities range from 49 – 56 μΩ cm up to 100 cycles, which is similar to the resistivity value of the uncoated ruthenium substrates (~52 μΩ cm). The similarity of these resistivity values to that of the ruthenium substrate is consistent with the lack of observed film growth at 25 and 50 cycles. The slightly decreased resistivity at 100 cycles (49 μΩ cm) might correlate with the ~2 nm thick cobalt layer observed by SEM. At 150 cycles, the resistivity value decreased to 35.9 μΩ cm, which can be attributed to the ~10 nm thick cobalt layer. At 250 cycles, the resistivity dropped to 18.5 μΩ cm for the ~25 nm thick cobalt layer, which is within the 13-19 μΩ cm range observed for 95 nm thick ALD cobalt metal films grown at 180 °C from $Co(^{tBu2}DAD)_2$ and formic acid.[82] As noted above, normal ALD growth on ruthenium substrates begins at about 250 cycles. As a comparison, cobalt metal has a bulk resistivity of 6.24 μΩ cm at 20 °C.[82] For platinum substrates, the resistivity values of films grown with 25 (~2.5 nm thick layer) and 50 (~5 nm thick layer) cycles were 47.1 and 45.3 μΩ cm, which are close to that of the uncoated platinum substrate (~43 μΩ cm). Cobalt-platinum alloy films containing up to 55% platinum have room temperature resistivities between 45 and 52 μΩ cm, which are similar to the films grown with 25 and 50 cycles.[96] Accordingly, cobalt-platinum alloys cannot be ruled out at low film thicknesses (*vide infra*). At 100 cycles (~10 nm thick layer), the resistivity dropped to 34.3 μΩ cm, consistent with the thicker cobalt layer and more cobalt metal contributing to the resistivity. At 150 (~15 nm thick layer) and 250 (~25 nm thick layer) cycles, the resistivity values (20.1, 19.6 μΩ cm) were close to the 13 – 19 μΩ cm range observed for 95 nm thick cobalt metal films on ruthenium substrates that we reported previously.[82] On copper substrates, the resistivities of films grown with 25 (~2.5 nm thick layer), 50 (~5 nm thick layer), and 100 (~10 nm thick layer) cycles were identical to that of the uncoated copper substrates (1.7 μΩ cm). This observation is consistent with the conduction occurring through the copper substrate in these thin films, formation of a highly conductive copper-cobalt alloy, or the presence of a thin surface copper layer (*vide infra*). The resistivity of the film grown at 150 cycles (~15 nm thick layer) increased slightly to 2.9 µΩ cm. At 250 cycles (~25 nm thick) the resistivity of the cobalt layer (14.9 µΩ cm) was within the 13 – 19 µΩ cm range noted above for 95 nm thick cobalt metal films on ruthenium substrates.

Table 2. Resistivities of cobalt films grown on metallic substrates using Co(^{tBu2}DAD)$_2$ and formic acid.

Cycles	Ruthenium[a,b]	Copper[a,c]	Platinum[a,d]
25	56.1	1.7	47.1
50	54.3	1.7	45.3
100	49.0	1.7	34.3
150	35.9	2.9	20.1
250	18.5	14.9	19.6

[a] Values are in µΩ cm.
[b] The measured resistivity of the uncoated ruthenium substrate is 52.1 µΩ cm.
[c] The measured resistivity of the uncoated copper substrate is 1.7 µΩ cm.
[d] The measured resistivity of the uncoated platinum substrate is 42.6 µΩ cm.

Films about 14 nm thick grown on copper and platinum substrates with 150 cycles of ALD cobalt at 180 °C were analyzed by XPS to gain insight into the nucleations and film properties. Both films gave the expected thicknesses for a growth rate of ~0.95 Å/cycle, consistent with normal ALD growth. The film on platinum showed oxidized cobalt in the scan prior to argon ion sputtering, consistent with our earlier report of surface oxidation in cobalt metal films.[82] The carbon 1s ionizations in the as-deposited film were consistent with adventitious surface hydrocarbons and disappeared after 15 seconds of sputtering. The oxidized cobalt and oxygen ionizations disappeared after sputtering for 45 seconds, after which only cobalt metal was present. Upon sputtering for 15 seconds or longer, ionizations consistent with cobalt metal were observed (Co $2p_{3/2}$ 778.36 eV, Co $2p_{1/2}$ 793.46 eV) (**Figure 17a**). The oxygen level was 1.0% after sputtering for 75 seconds, and carbon and nitrogen levels were below the detection limits (<0.5%). For comparison, a cobalt metal standard sample showed Co $2p_{3/2}$ and Co $2p_{1/2}$ ionizations at 778.36 and 793.46 eV, respectively (**Figure 17b**). The surface of the standard sample also showed oxidized cobalt, oxygen, and carbon ionizations prior to sputtering. Upon argon ion sputtering of the standard cobalt sample for 15 seconds, the oxygen and carbon ionizations disappeared, the oxidized cobalt was absent, and the cobalt metal ionizations were observed. Platinum ionizations were absent in the scan of the cobalt film on platinum before sputtering, but appeared after 15 seconds of sputtering (Pt $4f_{7/2}$ 70.03 eV, Pt $4f_{5/2}$ 73.48 eV) and were identical to the binding energies observed for the platinum metal standard. These data are consistent with cobalt metal deposition on the platinum substrate, with some surface oxidation that likely occurs upon exposure of the film to ambient atmosphere. **Figure 18** shows the atomic concentrations of elements present in the film after various sputtering times. Notably, there is considerable intermixing of cobalt and platinum upon sputtering for 15 seconds or more. These data imply formation of an interfacial cobalt-platinum alloy, which likely contributes to the facile nucleation of the cobalt films on platinum substrates. The intermixing of cobalt and platinum increases throughout the 14 nm thick cobalt layer, and possibly continues into the 10 nm thick platinum layer. In related studies, ALD copper films have been shown to form interfacial alloys that enhance nucleation on palladium and platinum substrates, but not on ruthenium substrates.[33, 94, 97]

Figure 17. High-resolution XPS multiplex of a) the Co 2p region of a 14 nm thick cobalt film grown on a platinum substrate at 180 °C b) the Co 2p region of a cobalt metal standard.

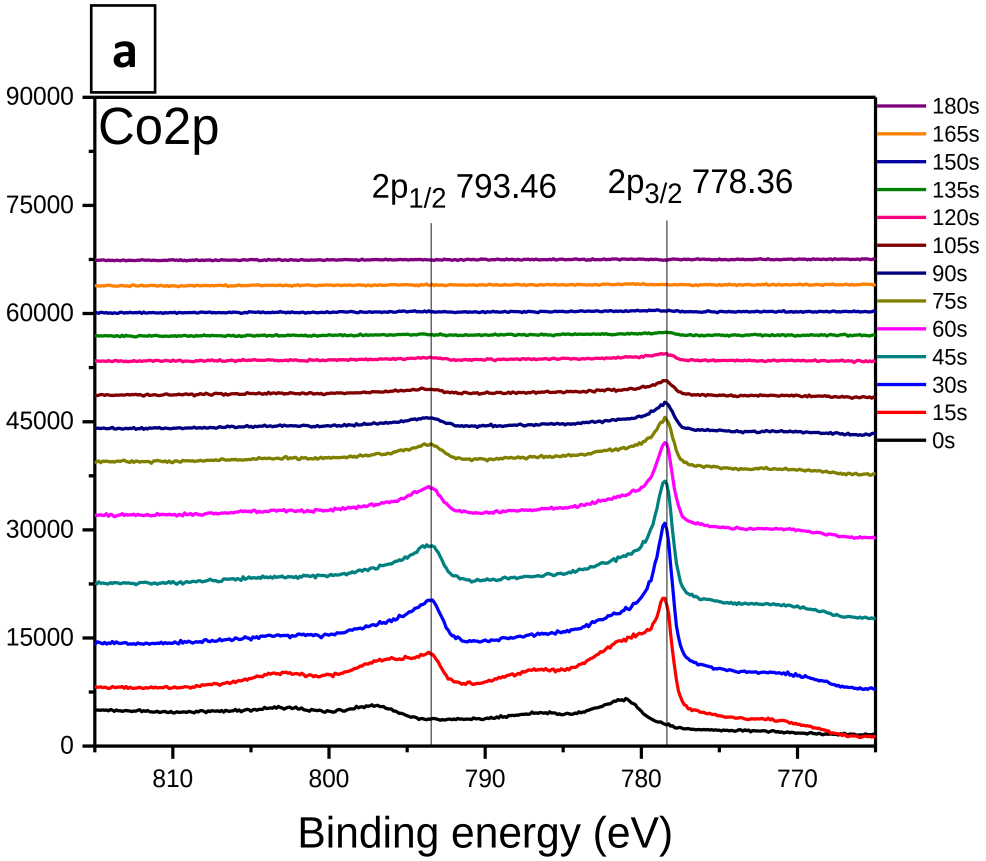

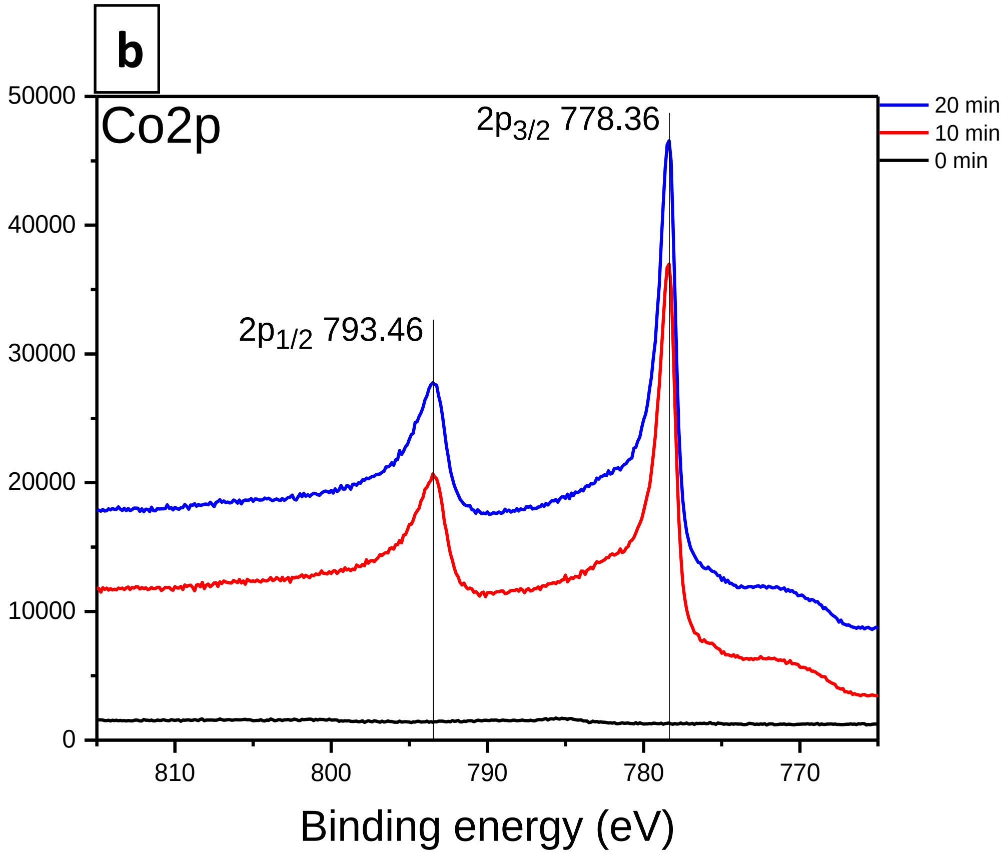
b
Co2p
2p3/2 778.36
2p1/2 793.46
20 min
10 min
0 min
50000
40000
30000
20000
10000
0
810
800
790
780
770
Binding energy (eV)

Figure 18. a) Plot of atomic concentration versus argon ion sputtering time, b) elemental compositions of a 14 nm thick cobalt film grown on a platinum substrate at 180 °C.

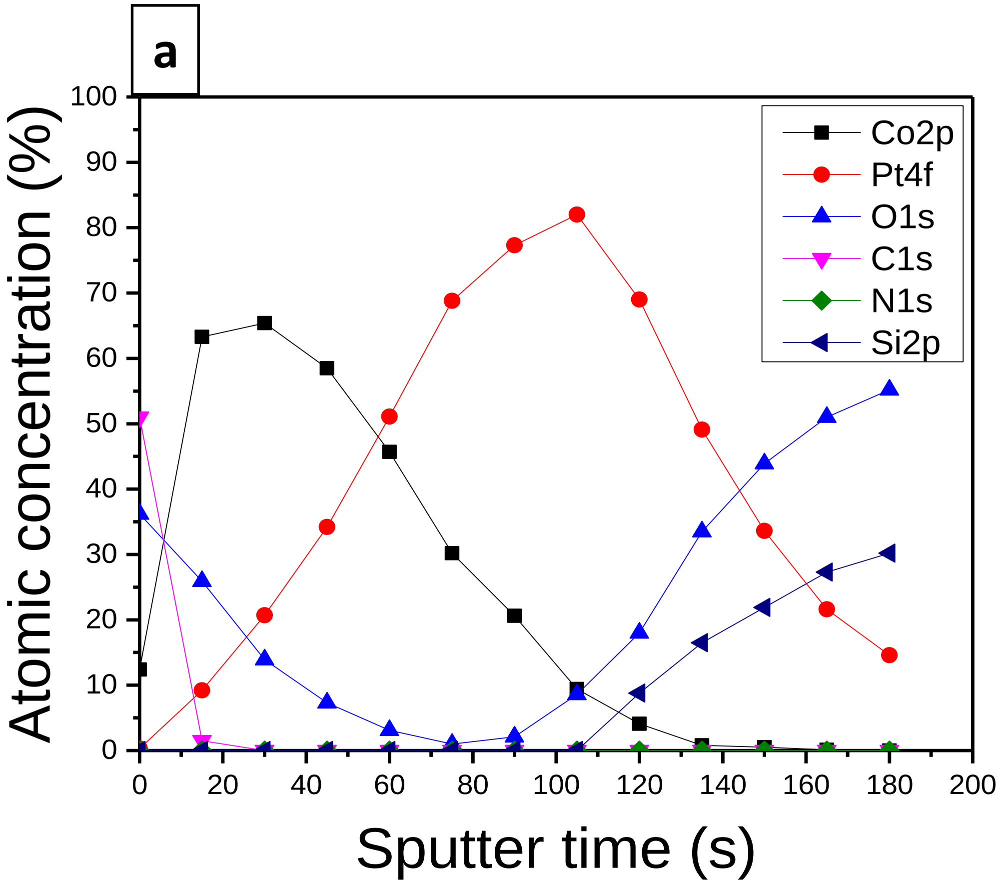

b

Sputter (s)	Co2p	Pt4f	O1s	C1s	N1s	Si2p
0	12.4	0.3	36.2	51.0	0.0	0.0
15	63.3	9.2	25.9	1.5	0.0	0.0
30	65.4	20.7	13.9	0.0	0.0	0.0
45	58.5	34.2	7.3	0.0	0.0	0.0
60	45.7	51.1	3.1	0.0	0.0	0.0
75	30.2	68.8	1.0	0.0	0.0	0.0
90	20.6	77.3	2.1	0.0	0.0	0.0
105	9.4	82.0	8.6	0.0	0.0	0.0
120	4.1	69.0	18.0	0.0	0.0	8.8
135	0.8	49.1	33.5	0.0	0.0	16.5
150	0.5	33.6	43.9	0.0	0.0	21.9
165	0.1	21.6	51.0	0.0	0.0	27.3
180	0.0	14.6	55.2	0.0	0.0	30.2

A 14 nm thick cobalt film grown on copper substrate was also studied by XPS. Unlike the cobalt films on platinum, XPS showed oxidized cobalt throughout the film, with underlying copper metal (**Figure 19**). Ionizations from cobalt metal were absent or of very low intensity. These data are consistent with complete oxidation of the cobalt film upon exposure to ambient atmosphere. Metallic copper is well known to undergo surface oxidation upon exposure to air.[95] A copper metal standard sample also showed surface oxidation, which disappeared upon sputtering for 15 seconds. It is possible that the oxidized copper on the substrate surface is reduced by the growing cobalt metal film, resulting in copper metal and cobalt oxide. Cobalt metal that grows on top of the cobalt oxide interfacial layer would be oxidized to cobalt oxide upon exposure to ambient air. **Figure 20** shows the atomic concentrations of elements present in the film after various sputtering times.

The oxygen and cobalt concentrations are similar throughout the film, consistent with the presence of cobalt oxide. Carbon and nitrogen levels were below the detection limits (<0.5%) after 60 seconds of sputtering. As above, there is considerable intermixing of the copper and cobalt layers. It is possible that the nucleation mechanism entails reaction of the surface copper oxides with the cobalt metal, to afford copper metal and cobalt oxide. This reduction process could lead to the observed intermixing. The element concentrations in **Figure 20** suggest both cobalt and copper in the 14 nm thick layer, with little copper at the surface of the film. The copper concentration increases with depth in the cobalt-containing layer. In related work, Gordon reported that a continuous, electrically connected 1.4 nm thick copper film could be grown by ALD at 190 °C on a 2 nm thick ALD cobalt layer.[78-79] Ekerdt also reported that the ALD growth of cobalt metal films on copper substrates using $Co(tBuNCEtNtBu)_2$ and H_2 at 265 °C led to intermixing of the copper and cobalt, and a surfactant-like copper layer ~2 nm thick was observed on top of the cobalt layer up 16 nm film thicknesses.[98] Unlike Ekerdt's work, we did not observe a copper surface layer by XPS, perhaps because of the presence of the copper oxides at initial stages of growth, or because of our lower 180 °C growth temperature. Prior to deposition, Ekerdt removed the copper oxide layer on the copper substrate by treatment with glacial acetic acid, presumably to afford a pristine copper metal surface. Accordingly, nucleations in the work of Ekerdt[98] and Gordon[78-79] are likely facilitated by interfacial metallic cobalt-copper alloy formation. Our substrates were not treated with acetic acid prior to depositions, so it is not clear if our nucleations on copper are promoted by interfacial metallic alloy formation or by reduction of the surface copper oxides by the cobalt metal.

Figure 19. High-resolution XPS multiplex of the Co 2p region of a 14 nm thick cobalt film grown on a copper substrate at 180 °C.

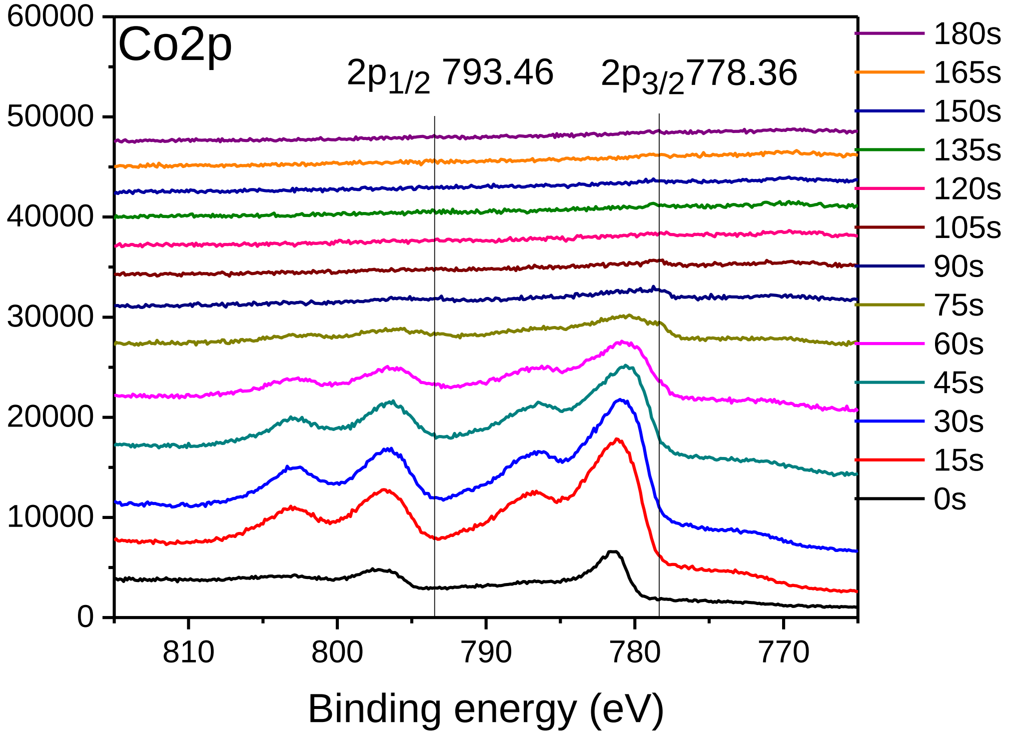

Figure 20. Plot of atomic concentration versus argon ion sputtering time of a 14 nm thick cobalt film grown on a copper substrate at 180 °C.

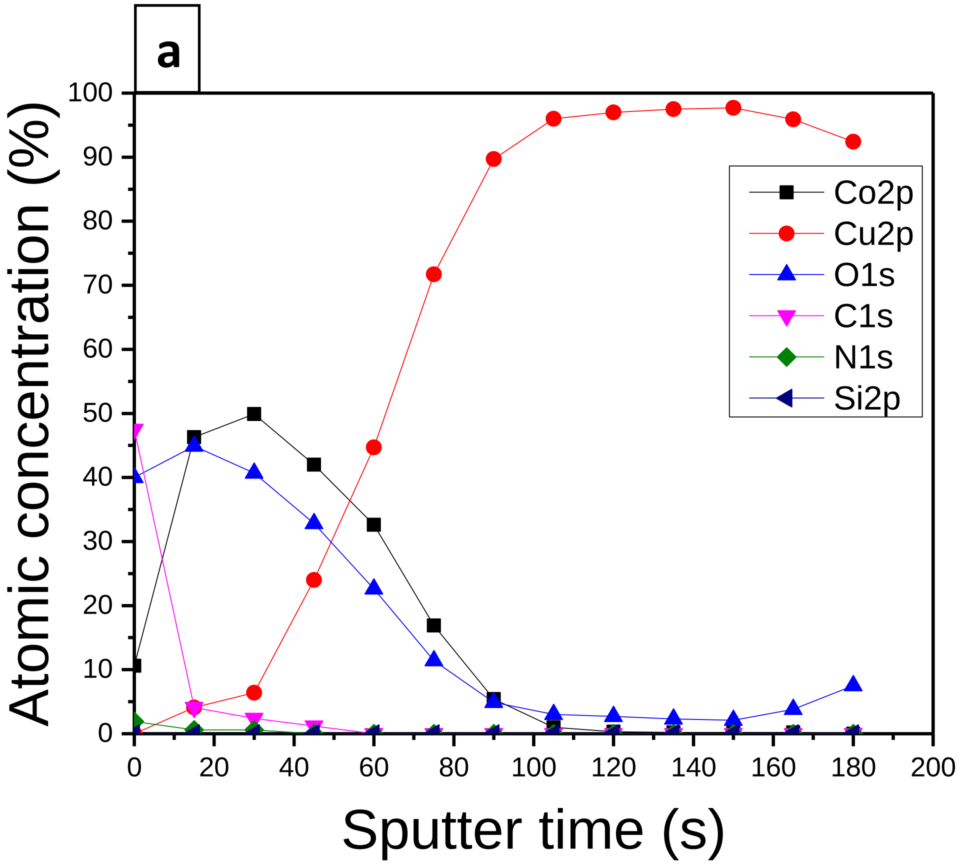

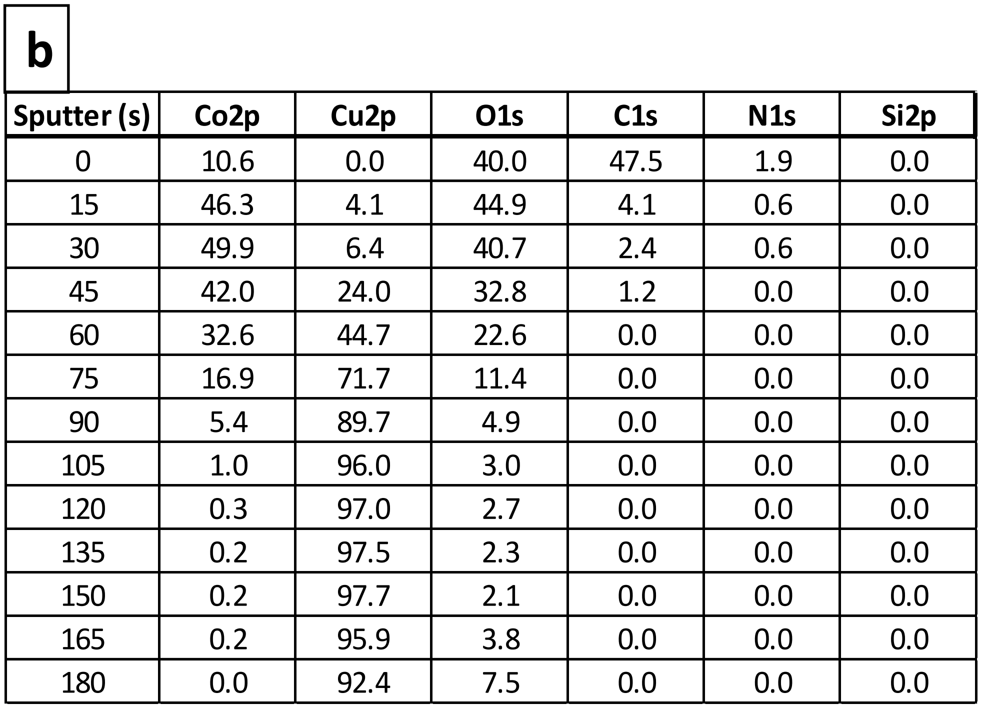

b

Sputter (s)	Co2p	Cu2p	O1s	C1s	N1s	Si2p
0	10.6	0.0	40.0	47.5	1.9	0.0
15	46.3	4.1	44.9	4.1	0.6	0.0
30	49.9	6.4	40.7	2.4	0.6	0.0
45	42.0	24.0	32.8	1.2	0.0	0.0
60	32.6	44.7	22.6	0.0	0.0	0.0
75	16.9	71.7	11.4	0.0	0.0	0.0
90	5.4	89.7	4.9	0.0	0.0	0.0
105	1.0	96.0	3.0	0.0	0.0	0.0
120	0.3	97.0	2.7	0.0	0.0	0.0
135	0.2	97.5	2.3	0.0	0.0	0.0
150	0.2	97.7	2.1	0.0	0.0	0.0
165	0.2	95.9	3.8	0.0	0.0	0.0
180	0.0	92.4	7.5	0.0	0.0	0.0

2.2.2 Attempted film growth on Si(100) with native oxide, Si-H, and CDO substrates

As part of the selectivity studies, cobalt metal ALD was attempted on Si(100), Si-H, and CDO substrates, using the conditions described above for growth on metal substrates. No film growth was observed by SEM on any of these substrates at up to 1000 cycles (**Figure 21a**), and EDS revealed no signals for cobalt in any of the samples (**Figure 21b**). Additionally, a CDO substrate was subjected to 150 cycles of ALD cobalt metal growth conditions at 180 °C as described above. The CDO substrate was then analyzed by XPS to determine if there was any cobalt metal on the surface. Inspection of the Co 2p region showed no ionizations for any cobalt species (**Figure 22**). The CDO substrate surface only showed the expected ionizations for carbon, silicon, and oxygen. Accordingly, cobalt metal does not nucleate on Si(100), Si-H, and CDO surfaces using Co(^{tBu2}DAD)$_2$ and formic acid at 180 °C.

Figure 21. a) Cross-sectional SEM of a CDO substrate after 1000 deposition cycles at 180 °C b) EDS of a CDO substrate after 1000 deposition cycles at 180 °C.

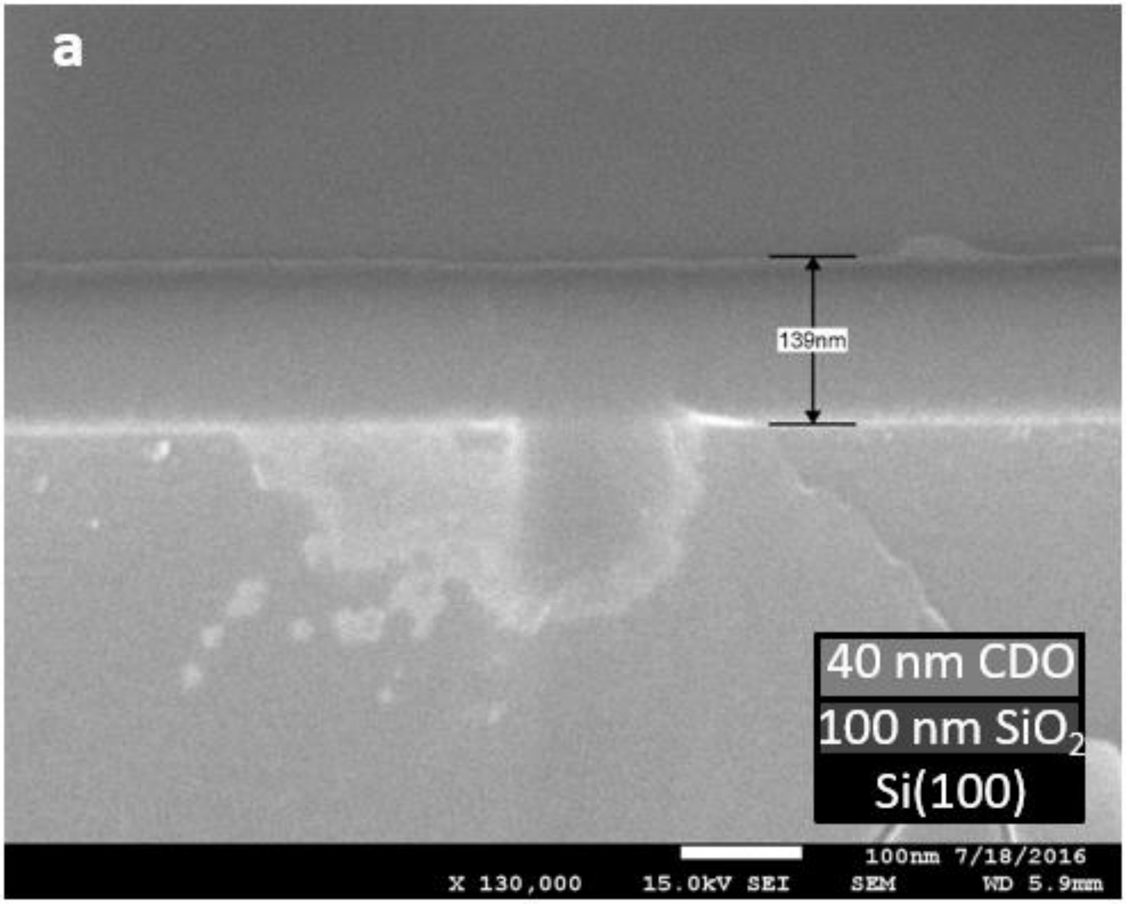

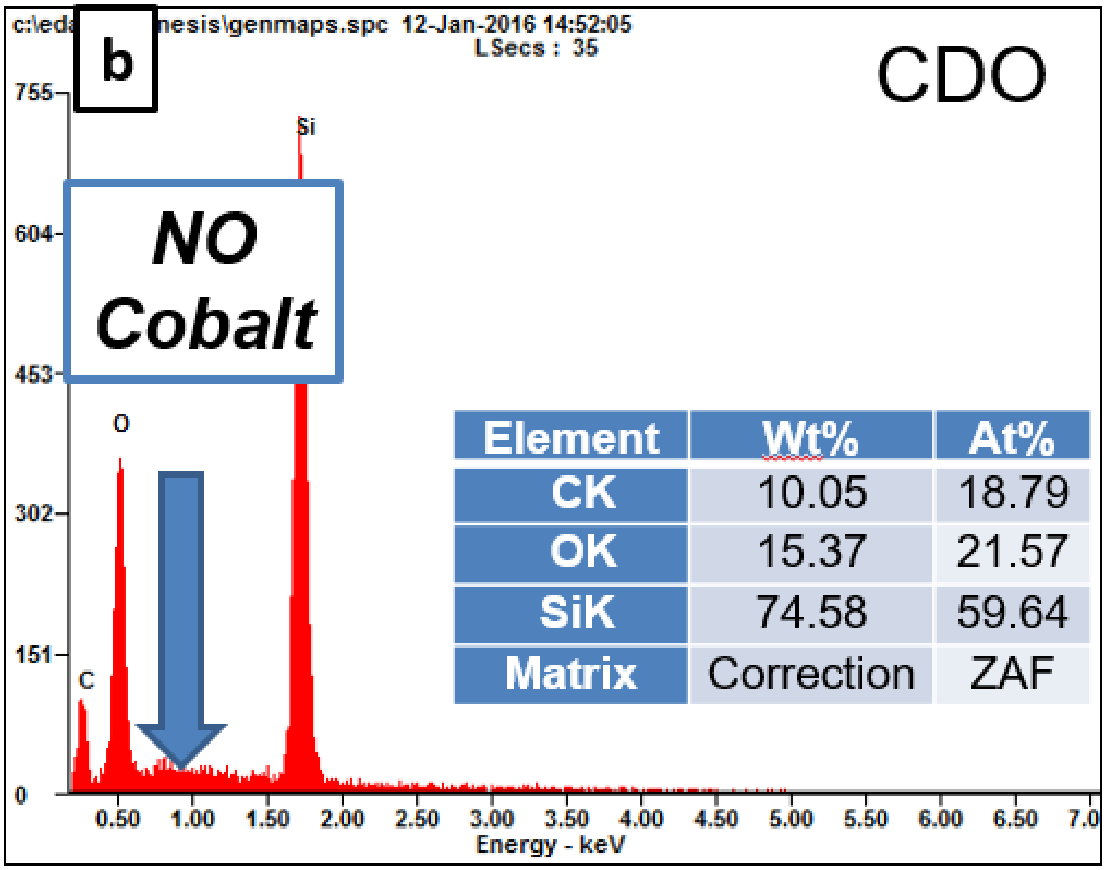

Element	Wt%	At%
CK	10.05	18.79
OK	15.37	21.57
SiK	74.58	59.64
Matrix	Correction	ZAF

Figure 22. High-resolution XPS multiplex of a CDO substrate after 150 deposition cycles at 180 °C.

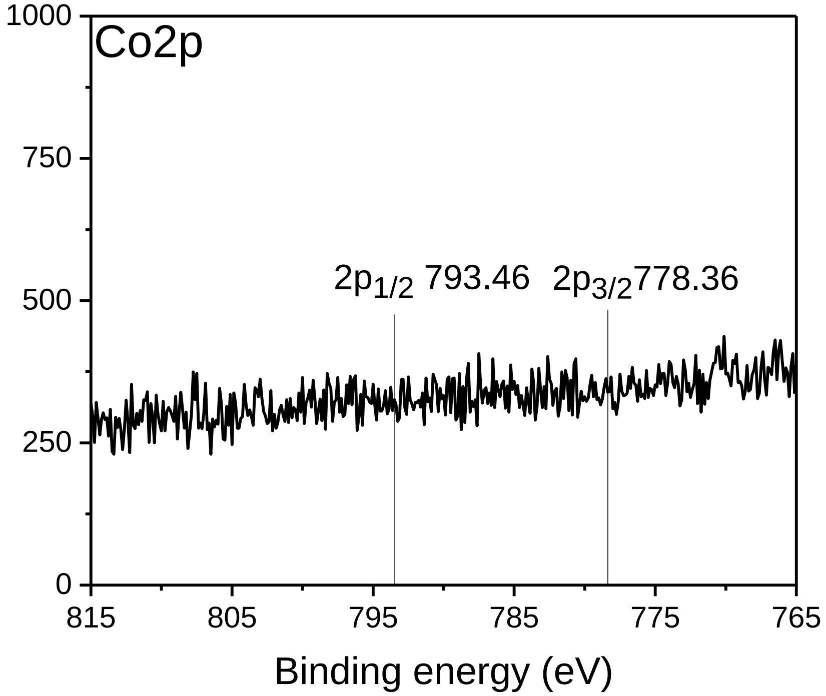

2.2.3 Film growth on thermal SiO_2 substrates

Unlike Si(100), Si-H, and CDO substrates, attempted ALD growth of cobalt metal films from $Co(^{tBu2}DAD)_2$ and formic acid at 180 °C on 100 nm thick thermal SiO_2/Si(100) substrates led to growth of continuous films. These films were non-conductive and did not show the metallic sheen of cobalt metal films. Films grown with 500 cycles were 35 nm thick, but were also 35 nm thick after 1000 cycles, suggesting very different behavior than the cobalt metal growth on metallic substrates described above. EDS analysis of a 35 nm thick film grown with 500 cycles showed a cobalt signal (**Figure 23**), indicating that the layer contained cobalt. The substrate with the 35 nm thick film grown with 500 cycles (**Figure 24a**) was rinsed with deionized water and was then blown dry with a stream of clean, dry air. Subsequent SEM analysis showed that the film had completely dissolved and only the thermal SiO_2 layer was observed (**Figure 24b**). This experiment demonstrates that the material deposited on SiO_2 is water soluble. For comparison, 25 nm thick cobalt metal films on ruthenium, platinum, and copper substrates were unaffected by rinses with deionized water. A 35 nm thick film on thermal SiO_2 was probed with infrared spectroscopy, and showed absorptions at 1574 and 1349 cm^{-1} (**Figure 25**), in addition to the SiO_2 absorptions. For comparison, a commercial sample of anhydrous copper(II) formate tetrahydrate showed absorptions at 1551 and 1359 cm^{-1}. Sodium formate shows carbon-oxygen stretches in the infrared spectrum at 1567 and 1366 cm^{-1}.[99] Finally, a 35 nm thick film on thermal SiO_2 was rinsed with deionized water to dissolve the film, dried with a stream of clean, dry air, and then subjected to analysis by infrared spectroscopy. The absorptions at 1574 and 1349 cm^{-1} were not present on the water-rinsed substrate. These observations are consistent with the formation of cobalt(II) formate on the thermal SiO_2 substrates. The fact that cobalt(II) formate layers grow only on the 100 nm thick thermal SiO_2 substrates, and not on Si(100) with native oxide (1-2 nm), must be related to reactions of the thick SiO_2 layer with formic acid, which then lead to cobalt(II) formate upon subsequent treatment with $Co(^{tBu2}DAD)_2$. There is not enough SiO_2 on Si(100) with native oxide substrates to afford detectable amounts of cobalt(II) formate.

Figure 23. EDS of ~35 nm of film after 500 deposition cycles on SiO_2.

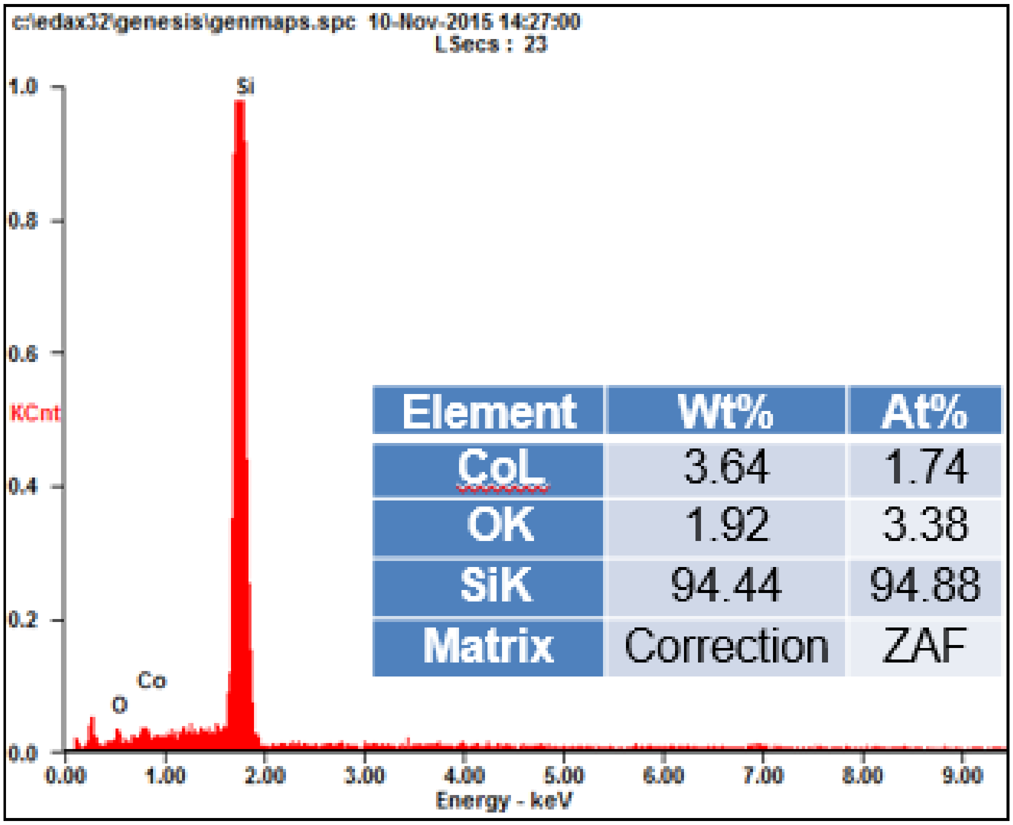

Element	Wt%	At%
CoL	3.64	1.74
OK	1.92	3.38
SiK	94.44	94.88
Matrix	Correction	ZAF

Figure 24. Cross-sectional SEM of ~35 nm of film after 500 deposition cycles on SiO_2, a) before deionized water rinse and b) after deionized water rinse.

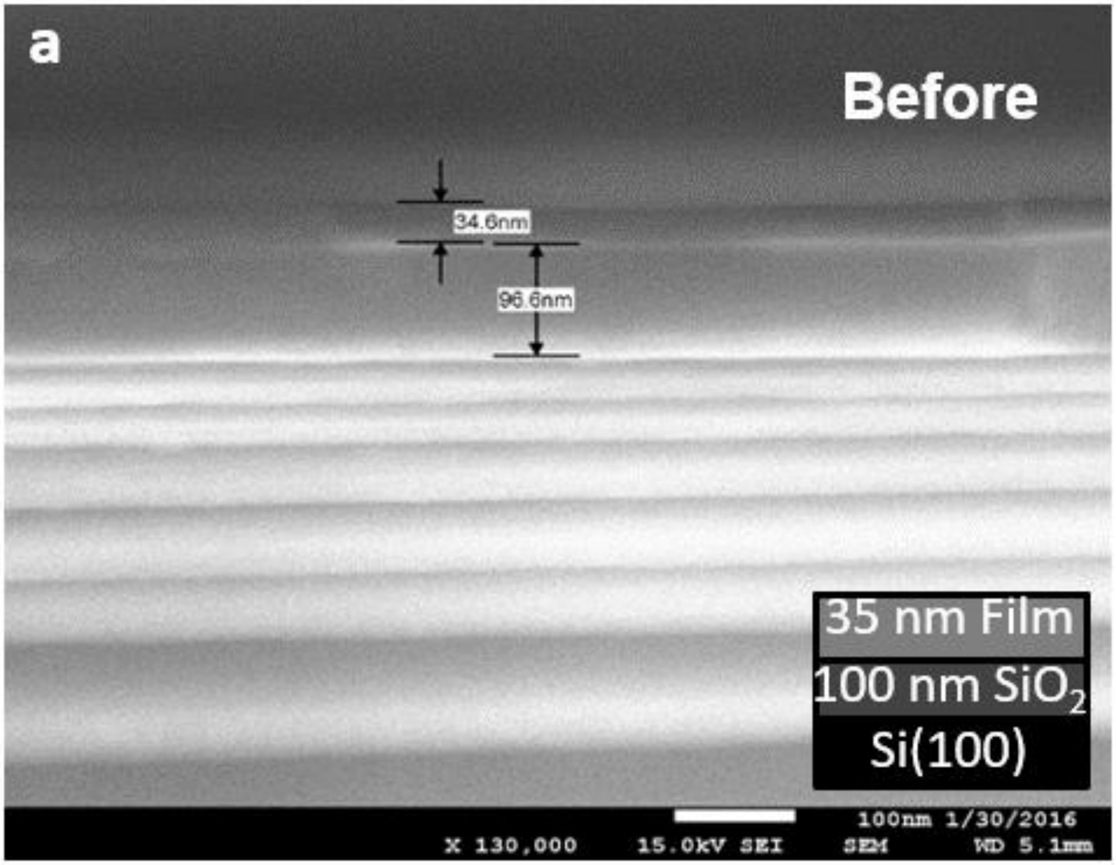

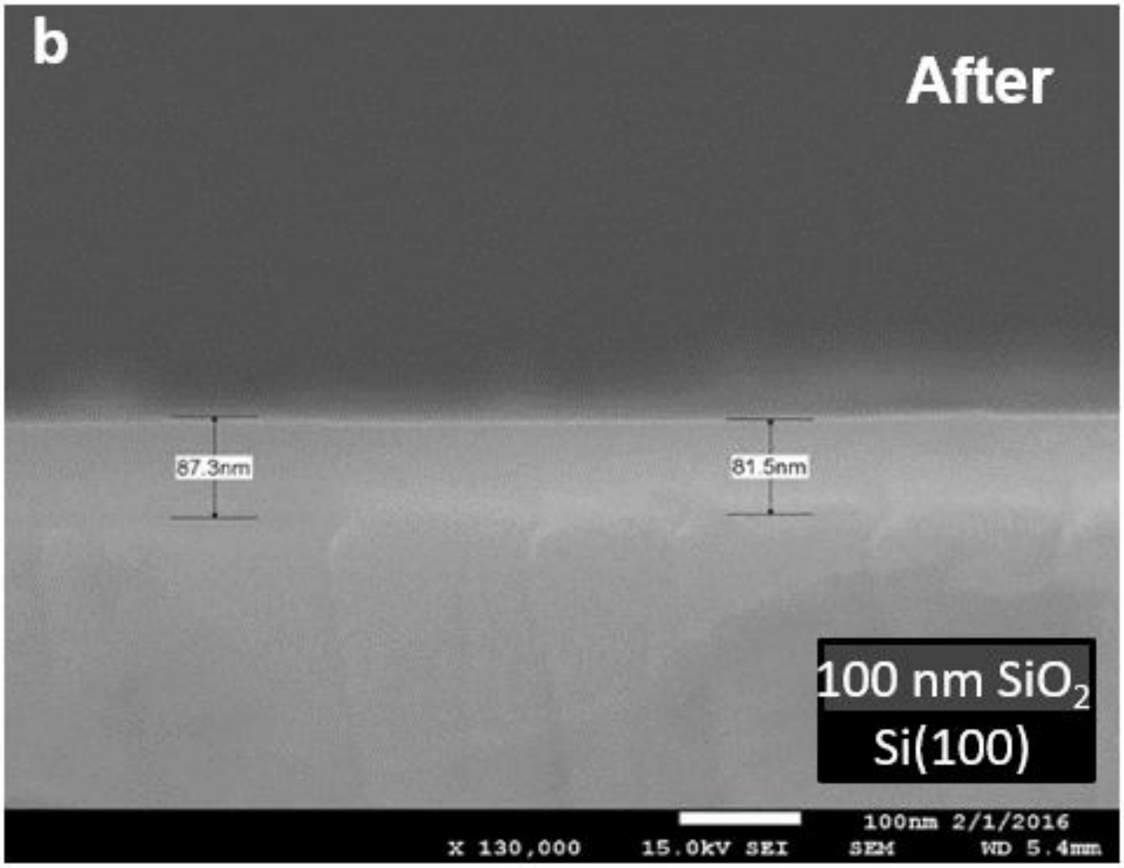
b
After
87.3nm
81.5nm
100 nm SiO_2
Si(100)
100nm 2/1/2016
X 130,000
15.0kV SEI
SEM
WD 5.4mm

Figure 25. Infrared spectrum of ~35 nm of film after 500 deposition cycles on SiO_2.

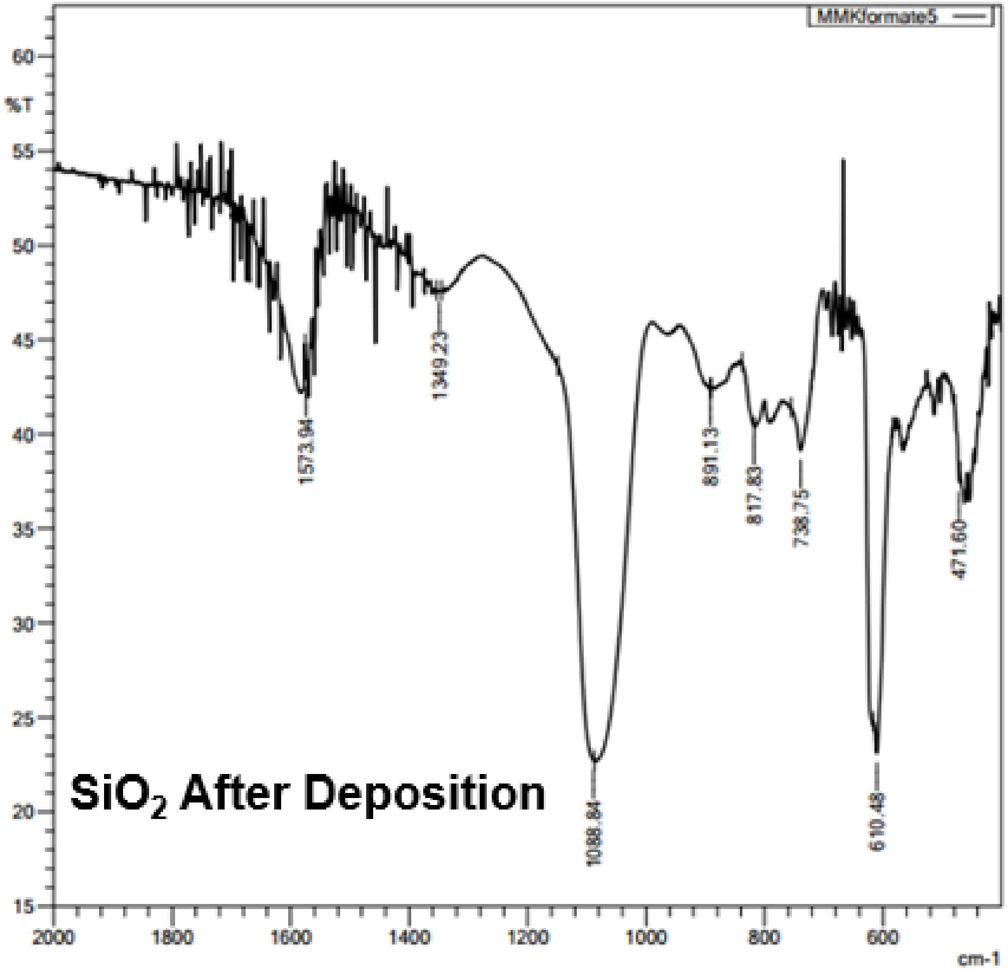

2.2.4 ALD selectivity temperature window

We next sought to define the “area-selective ALD temperature window”, which is the temperature range where inherent selectivity for metal surfaces is observed but no growth occurs on dielectric surfaces. Depositions were carried out with the pulse sequence described above, but the substrate temperatures were varied to determine the temperature dependence of the selective ALD processes. Since < 20 nm thick cobalt metal films are desired in device fabrication, each deposition was run with 250 cycles (~25 nm thick films on metal substrates). Depositions were performed at 160, 170, 180, 190, 200, and 220 °C on Si(100), Si-H, and CDO substrates to observe the temperature at which nucleation begins to occur. Temperatures of 230 °C and higher were avoided, since self-decomposition of Co(^{tBu2}DAD)$_2$ to cobalt metal occurs.[92] No film growth was observed by SEM from 160 to 200 °C on any of the substrates. At 220 °C, no film growth was detected on Si(100) or Si-H, however, CDO showed the formation of particles on the surface. Attempts were made to characterize the surfaces of the CDO substrates containing the particles that were deposited at 220 °C. No cobalt signals were observed with EDS, which is consistent either with the particles not containing cobalt or, more likely, with insufficient signal to noise to observe the cobalt EDS signal from widely spaced particles. Therefore, cobalt metal films from Co(^{tBu2}DAD)$_2$ and formic acid have a substrate selectivity temperature window for growth on metals and not on Si(100), Si-H, and CDO from 160 to 200 °C (**Figure 26**). The selectivity window for growth on metals over Si(100) and Si-H spans 160 to 220 °C. SiO_2 substrates are a special case, since cobalt(II) formate appears to form on these surfaces at 180 °C.

Figure 26. Area-selective ALD temperature windows, where no growth was observed on Si(100), Si-H, and CDO substrates after 250 cycles.

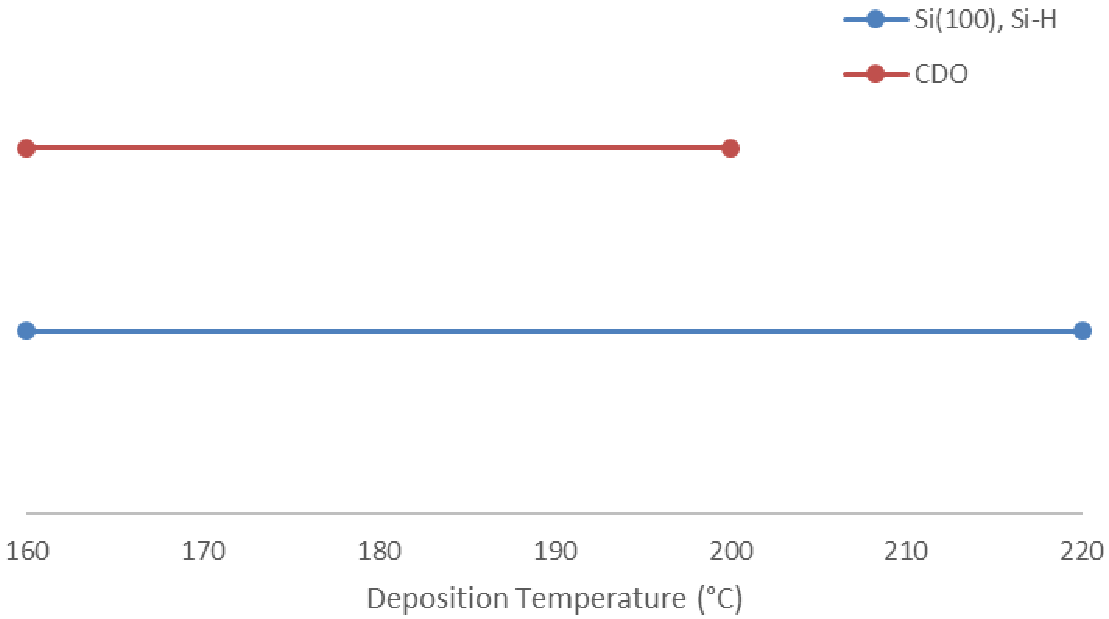

2.3 Conclusions

The growth of metallic cobalt was demonstrated on a variety of metallic substrates (platinum, copper, and ruthenium) using Co(^{tBu2}DAD)$_2$ and formic acid as precursors. Linear growth on platinum and copper substrates was observed for ≥ 25 cycles (~ 25 Å thick), showing no nucleation delay for this process on these substrates. Growth of metallic cobalt films on ruthenium shows a delay in normal growth behavior before 250 cycles. This is likely due to oxidation of the substrate surface, which is then reduced during the initial cycles.[93] The observed growth rate of 0.98 Å/cycle matched that of the previously reported growth rate of cobalt deposited on ruthenium between 250 and 2000 cycles.[82] This suggests that normal ALD growth occurs on platinum and copper substrates immediately, likely through facile interfacial alloy formations. Bulk resitivities of cobalt films grown on copper and platinum at the early stages of growth (≤ 150 growth cycles) support the formation of interfacial alloys.[78-79, 96, 98] In contrast, the resistivities of cobalt films grown on ruthenium at the early stages of growth match that of the bare ruthenium wafer, which suggests no formation of alloys. XPS depth profiling shows significant intermixing of cobalt with the metallic substrate (platinum and copper) upon sputtering in each sample, supporting the hypothesis of the film growth proceeding via formation of interfacial alloys. AFM analysis showed smooth, continuous cobalt metal films on platinum and copper substrates, with rms surface roughnesses of 0.6 nm and 1.1 – 2.4 nm respectively. The higher rms surface roughness for the copper substrate is likely due to the surface roughness of the bare copper substrate, which also contained similar particle and pit features. Films of metallic cobalt were not observed on Si(100), SiO_2, Si-H, and CDO substrates up to 1000 cycles, which was confirmed by cross-sectional SEM and EDS, with the exception of the SiO_2 substrate. The SiO_2 substrate shows ~35 nm of material from ≥ 500 cycles, and has a peak which corresponds to cobalt present in EDS. The material was not conductive, suggesting that it is not cobalt metal. This material was hypothesized to be cobalt (II) formate, which is supported by infrared spectroscopy. Absorptions at 1574 and 1349 cm^{-1}, in addition to the SiO_2 substrate absorptions, were observed. Absorptions reported in the literature[99] for the infrared spectrum of sodium formate (1567 and 1366 cm^{-1}) correspond to those of the deposited material on SiO_2. The resulting material grown after 500 deposition cycles on the SiO_2 substrate was rinsed with deionized water post-deposition, due to the solubility of cobalt (II) formate in water. Rinsing the sample with water resulted in the removal of the material, confirmed by cross-sectional SEM and infrared spectroscopy. These results support the formation of cobalt (II) formate on the SiO_2

substrates. A selectivity window for the deposition of cobalt metal on metallic substrates over Si(100), Si-H, and CDO was observed from 160 to 200 °C. Particle deposition was observed on carbon-doped oxide substrates at 220 °C, with no film growth evident on Si(100) and Si-H at this temperature.

2.4 Experimental Section

A Picosun R-75BE ALD reactor was used for the thin film deposition experiments. The ALD reactor was operated under a constant stream of nitrogen (99.999%) at a pressure of 6-9 Torr. The deposition of cobalt metal thin films was studied with $Co(^{tBu2}DAD)_2$ and formic acid. $Co(^{tBu2}DAD)_2$ was prepared according to a literature procedure[92] and formic acid was purchased from Sigma Aldrich. In initial growth trials, the source temperature for $Co(^{tBu2}DAD)_2$ was found to be optimum at 130 °C under the reactor pressure. Substrate temperatures were varied between 160 and 240 °C. Nitrogen was used as both the carrier and purge gas and was purified from ambient air using a Texol GeniSys nitroGenerator. Film growth experiments used to assess selectivity were performed using the pulse sequence $Co(^{tBu2}DAD)_2$ (5.0 s)/N_2 purge (10.0 s)/formic acid (0.2 s)/N_2 purge (10.0 s) at 180 °C that was established in our previous report of cobalt metal ALD from $Co(^{tBu2}DAD)_2$ and formic acid.[82] For the selectivity temperature window experiments, the same pulse and purge sequence was used, but the deposition temperatures were varied as described in the text. ALD growth studies were performed on Ru (13 nm)/TaN (2 nm)/SiO_2 (100 nm)/Si(100), Cu (33 nm)/TaN (7 nm)/SiO_2 (100 nm)/Si(100), Pt (10 nm)/SiO_2 (100 nm)/Si(100), Si(100) with native oxide, Si-H, thermal SiO_2 (100 nm)/Si(100), and CDO (~40 nm)/SiO_2 (100 nm)/Si(100) substrates. Si-H substrates were prepared by treating

Si(100) with native oxide substrates with a 2% aqueous HF solution, followed by rinsing with deionized water and then drying with a stream of clean, dry air. The other substrates were used as received, except that they were rinsed sequentially with isopropanol and deionized water and then were dried with a stream of clean, dry air. One substrate of each kind, a 2 x 2 cm^2 coupon, was used in each experiment.

Film thicknesses were determined using cross-sectional SEM collected on a JEOL-6510LV electron microscope. The growth rates were determined by dividing the measured film thicknesses by the number of deposition cycles. Film thicknesses were measured at a minimum of three positions on each film to evaluate the uniformity. EDS was carried out on the JEOL-6510LV electron microscope using an Ametek EDAX system with Genesis Spectrum software. The accelerating voltage for the EDS measurements was 6 kV. AFM measurements were conducted using a VEECO Dimension 3100 operated in the tapping mode. XPS measurements were conducted using an Al Kα (1486.6 eV) X-ray source at a chamber base pressure of 10^{-10} Torr. Spectra were recorded using a 16-channel detector with a hemispherical analyzer. Sputtering was performed using argon ions supplied by an argon sputter gun positioned at a 45° angle with respect to the substrate normal. Each sample was sputtered over a 2 x 2 mm^2 area and measured over a 0.8 x 0.8 mm^2 area. Cobalt and copper metal standards were sputtered with 5 kV argon ions. An uncoated platinum substrate (Pt (10 nm)/SiO_2 (100 nm)/Si(100)) was used as a standard for platinum and was sputtered with 3 keV argon ions. The ALD-grown cobalt films on copper and platinum were sputtered with 3 keV argon ions. Sheet resistivity measurements were obtained using a Jandel 4-point probe in combination with a Keithley 2400 SourceMeter and a Keithley 2182A Nanovoltmeter. Infrared spectra were obtained on a Shimadzu IRTracer-100 spectrophotometer. All films grown on metal substrates passed the Scotch tape test.

CHAPTER 3 LOW TEMPERATURE GROWTH AND SUBSTRATE SELECTIVITY OF COBALT METAL THIN FILMS BY THERMAL ATOMIC LAYER DEPOSITION FROM BIS(1,4-DI-*TERT*-BUTYL-1,3-DIAZADIENYL)COBALT AND ALKYL AMINES

3.1 Introduction

The inherently selective process of ALD growth of cobalt metal from $Co(^{tBu2}DAD)_2$ and formic acid preferentially deposits on metallic substrates over non-metallic substrates.[34] This process affords not only excellent quality metallic cobalt thin films, but also desirable selectivity for applications of cobalt described in Chapter 1. However, formic acid is highly corrosive and can lead to damage of substrates and reactor parts, making it an undesirable co-reagent that could limit use of this deposition method in industrial manufacturing. It is imperative that a less corrosive ALD co-reactant be found as a suitable alternative to formic acid while still yielding high-purity cobalt metal, with high selectivity by low temperature ALD.

In this chapter, the growth of metallic cobalt was demonstrated on a variety of substrates using $Co(^{tBu2}DAD)_2$ and *tert*-butyl amine as precursors (**Figure 27**). When using *tert*-butyl amine, a growth rate of 0.98 Å/cycle was achieved in the ALD window of 170 – 200 °C. The resultant films were continuous, featured high-purity metallic cobalt films, and exhibited low resistivity values when grown on a metallic substrates. Trial depositions using other alkyl amines are also discussed in this chapter.

Figure 27. General reaction scheme for the deposition of cobalt metal thin films from Co(^{tBu2}DAD)$_2$ and *tert*-butyl amine by thermal ALD.

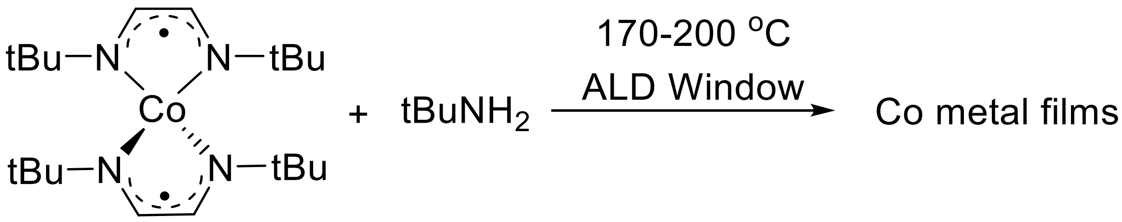

3.2 Results and Discussion

3.2.1 Low Temperature ALD Study of Cobalt Metal from Co(^{tBu}DAD)$_2$ and *tert*-butyl Amine

Experiments to demonstrate ALD growth of metallic cobalt using Co(^{tBu2}DAD)$_2$ and *tert*-butyl amine were performed on platinum substrates. First, self-limiting growth was established by varying the pulse length of one co-reagent at a time while keeping all other conditions constant, then plotting the growth rate as a function of precursor pulse length. Experiments to evaluate Co(^{tBu2}DAD)$_2$ saturation used a pulsing sequence of Co(^{tBu2}DAD)$_2$ (varied), purge (10.0 s), *tert*-butyl amine (0.2 s), purge (10.0 s) for 200 cycles, at a deposition temperature of 200 °C. Self-limited growth was observed after ≥ 3.0 s pulse lengths of Co(^{tBu2}DAD)$_2$, as evidenced by a constant growth rate of 0.98 Å/cycle (**Figure 28**). Saturation of *tert*-butyl amine was determined by varying the pulse length of *tert*-butyl amine, keeping all other deposition parameters constant. These experiments used a pulsing sequence of Co(^{tBu2}DAD)$_2$ (4.0 s), purge (10.0 s), *tert*-butyl amine (varied), purge (10.0 s) for 200 cycles, at a deposition temperature of 200 °C. Self-limited growth was observed after ≥ 0.1 s pulse lengths of *tert*-butyl amine, as evidenced by a constant growth rate of 0.98 Å/cycle (**Figure 29**).

Figure 28. Plot of growth rate of cobalt metal on platinum substrates *versus* pulse length of Co(^{tBu2}DAD)$_2$ after 200 cycles, using Co(^{tBu2}DAD)$_2$ and *tert*-butyl amine as precursors.

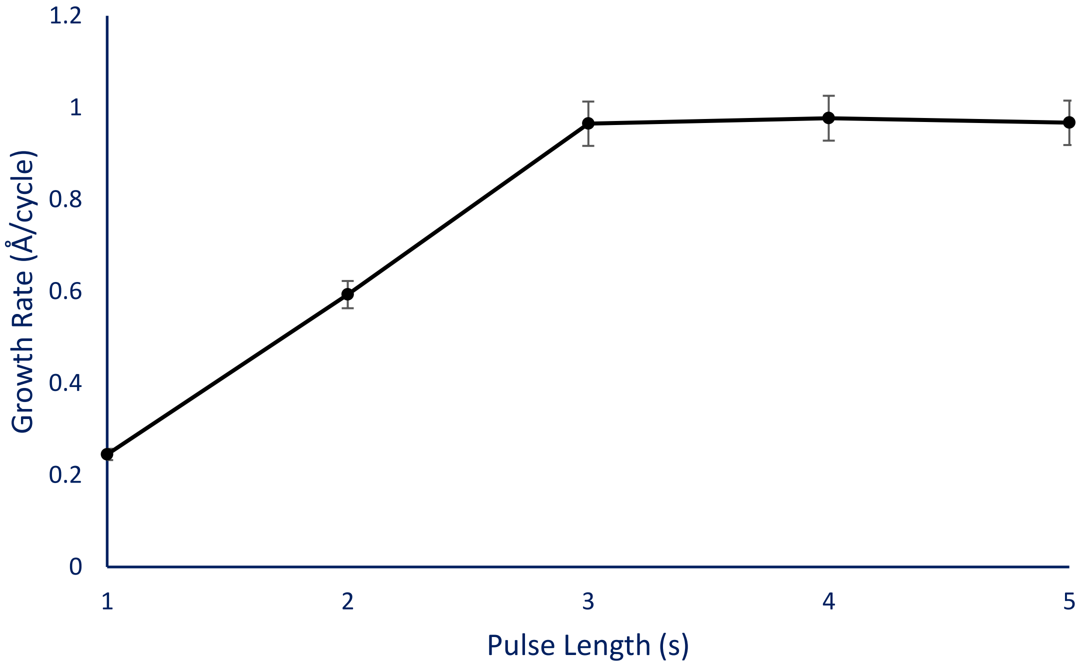

Figure 29. Plot of growth rate of cobalt metal on platinum substrates *versus* pulse length of *tert*-butyl amine after 200 cycles, using Co($^{\mathrm{tBu2}}$DAD)$_2$ and *tert*-butyl amine as precursors.

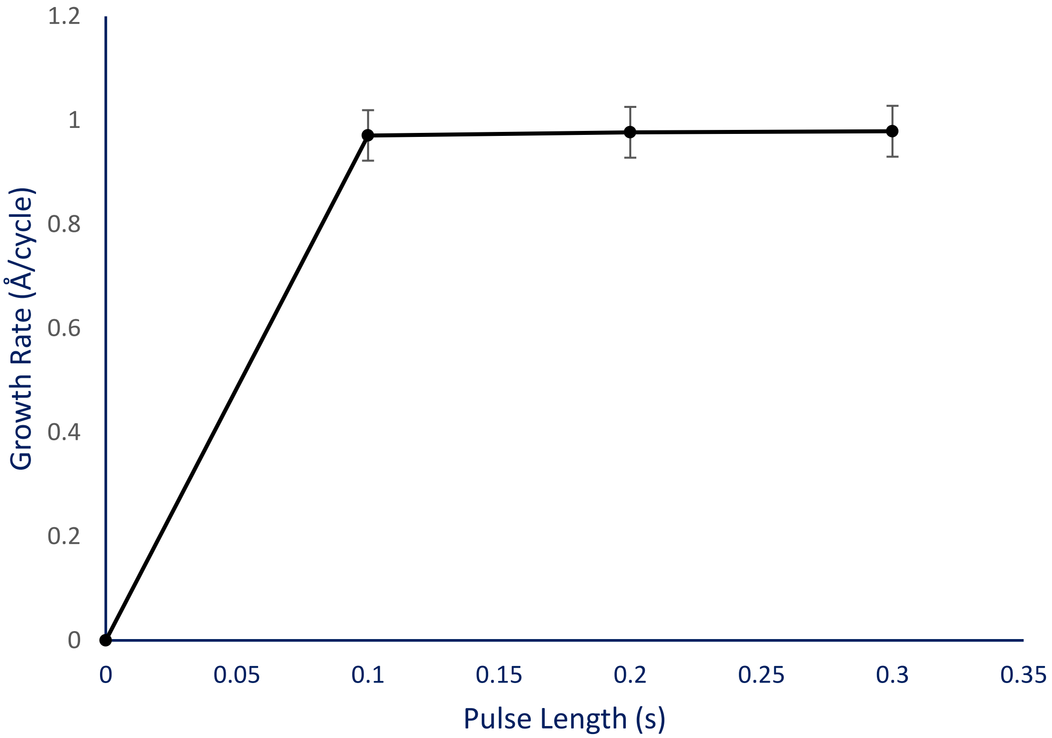

To assess temperature dependence, experiments to construct an ALD window were performed. Films were grown using a saturative pulsing sequence of Co($^{\mathrm{tBu2}}$DAD)$_2$ (4.0s), purge (10.0 s), *tert*-butyl amine (0.1 s), purge (10.0 s) at temperatures within 160 – 220 °C, each for 200 cycles. Due to the decomposition temperature of Co($^{\mathrm{tBu2}}$DAD)$_2$ (235 °C) higher temperatures were not evaluated.[92] A constant growth rate of 0.98 Å/cycle was observed between 170 – 200 °C for films deposited on platinum substrates (**Figure 30**). Cross-sectional SEM images revealed uniform, continuous films deposited on platinum in the ALD window.

Figure 30. Plot of growth rate *versus* deposition temperature for cobalt metal growth on platinum substrates after 200 cycles using Co($^{\mathrm{tBu2}}$DAD)$_2$ and *tert*-butyl amine.

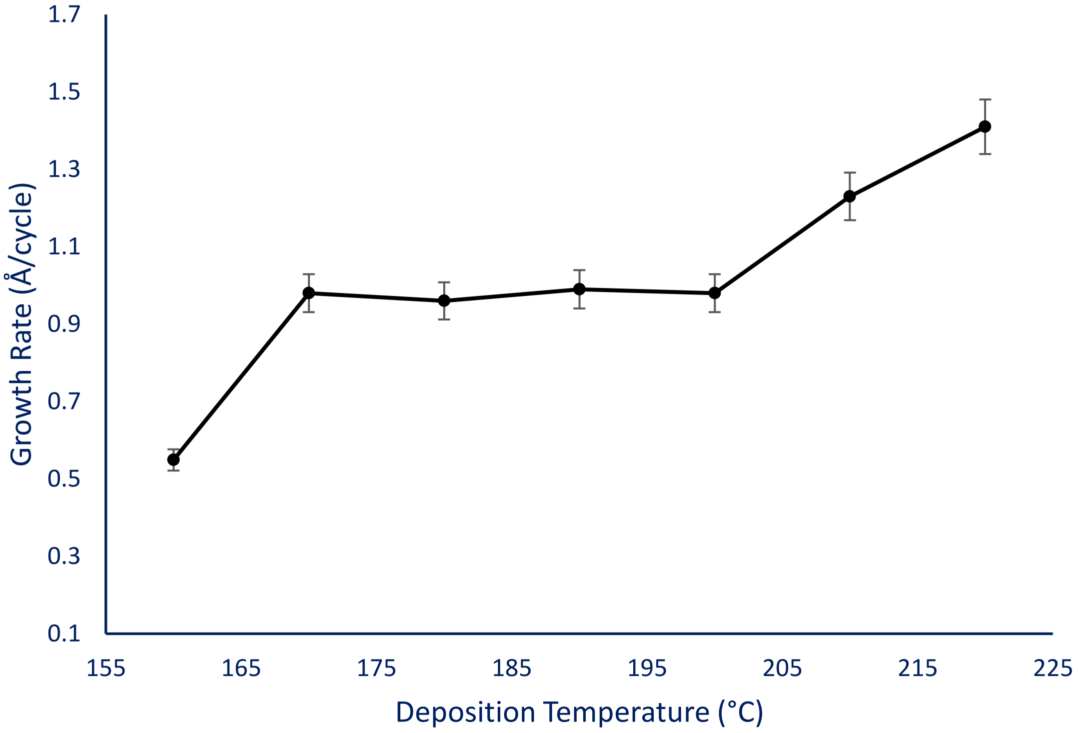

To evaluate the growth of this process as a function of number of ALD cycles, the same saturative dose pulsing sequence used for the ALD window determination was used, at a deposition temperature of 200 °C, while varying the number of cycles. The resulting plot shows a slope of 0.98 Å/cycle on platinum from 25 – 1000 cycles (**Figure 31**). The y-intercept of 0.095 is within experiment error of zero, indicating that as few as 25 cycles are needed to achieve normal ALD growth without a nucleation delay. Fewer than 25 deposition cycles was not explored, since the cross-sectional SEM measurements are limited by a minimum film thickness of ~2 nm.

Figure 31. Plot of thickness *versus* number of cycles for cobalt metal growth on platinum substrates at 200 °C using Co(^{tBu2}DAD)$_2$ and *tert*-butyl amine.

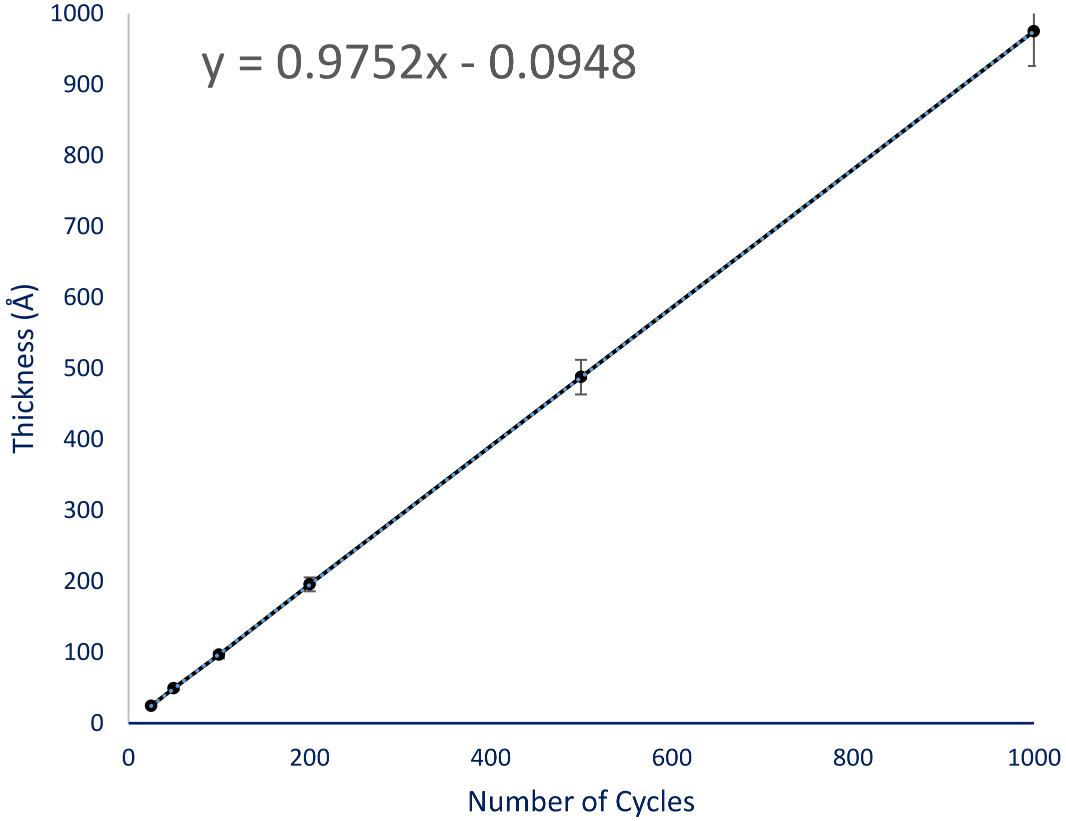

3.2.2 Characterization of Films Deposited by ALD using Co(^{tBu}DAD)$_2$ and *tert*-butyl amine

XRD was performed on a ~50 nm cobalt film grown on a platinum substrate to assess the degree of crystallinity of the as-deposited film (**Figure 32**). The XRD pattern displayed reflections consistent with that of crystalline cobalt metal (PDF#00-001-1254) with the remaining peaks consistent with that of the previously determined XRD pattern for the bare substrate.

Figure 32. X-ray diffraction pattern for ~50 nm thick cobalt metal film grown on a platinum substrate at 200 °C using Co(^{tBu2}DAD)$_2$ and *tert*-butyl amine.

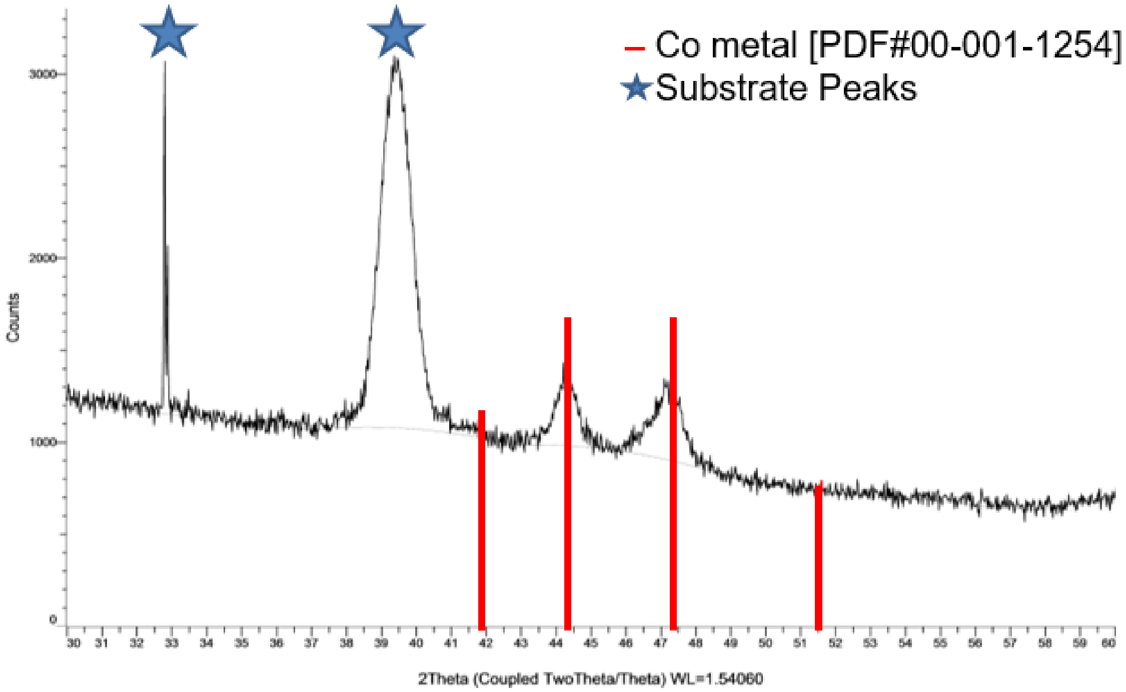

AFM was performed to examine the surface topologies of films of different thicknesses (~10 nm, 100 cycles and ~100 nm, 1000 cycles) grown on platinum substrates. The uncoated platinum substrate has been previously measured to have an rms roughness value of 0.19 nm.[34] The ~10 nm thick film had an rms roughness value of 0.22 nm over the full 5 x 5 μm^2 area (**Figure 33**), which corresponds to 2.2% of the total film thickness. The ~100 nm thick film had an rms roughness value of 3.07 nm over the full 5 x 5 μm^2 area (**Figure 34**), which corresponds to 3.07% of the total film thickness. These rms roughness values indicate that over a wide span of thicknesses, the as-deposited films from this process are extremely smooth.

Figure 33. Atomic force microscopy 5 x 5 μm^2 area image of a ~10 nm thick cobalt metal film (100 cycles) grown on a platinum substrate at 200 °C using Co(^{tBu2}DAD)$_2$ and *tert*-butyl amine; rms roughness = 0.22 nm.

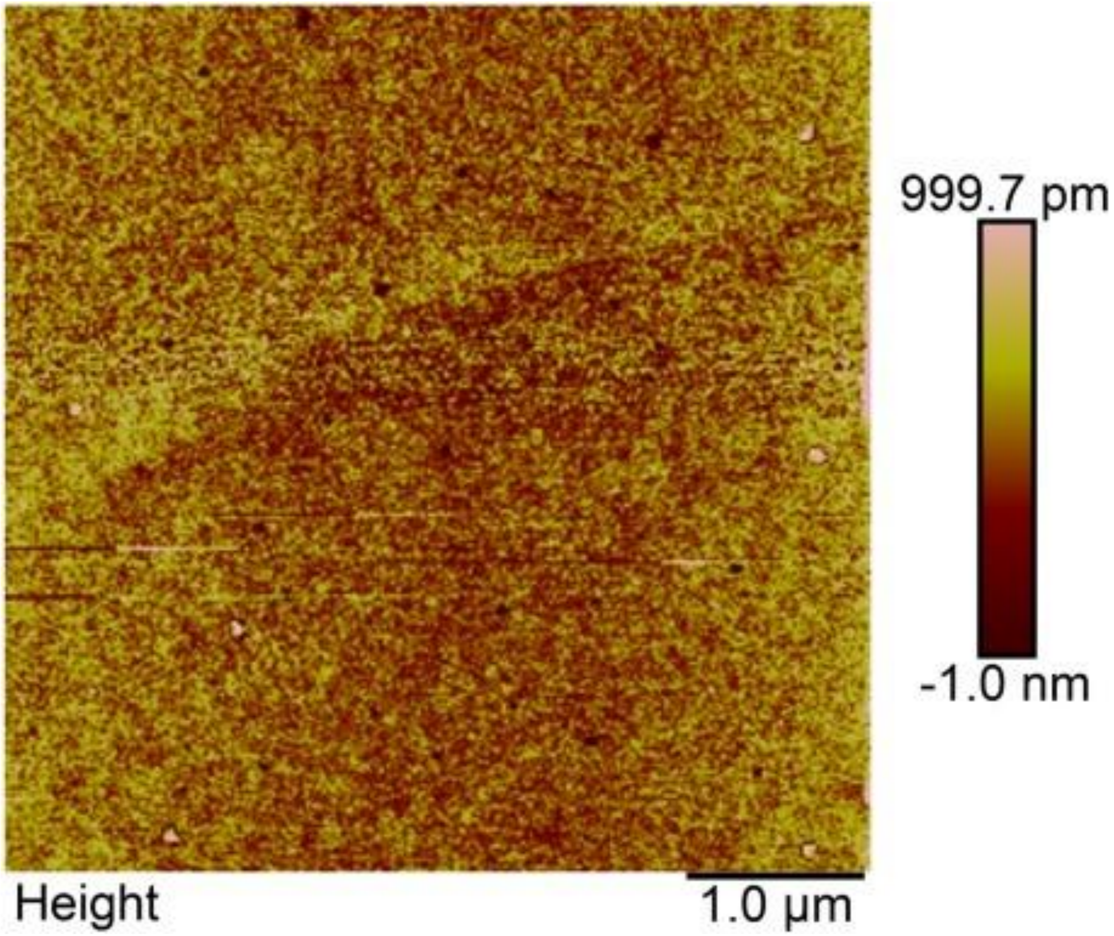

Figure 34. Atomic force microscopy 5 x 5 μm^2 area image of an ~100 nm thick cobalt metal film (1000 cycles) grown on a platinum substrate at 200 °C using Co(^{tBu2}DAD)$_2$ and *tert*-butyl amine; rms roughness = 3.07 nm.

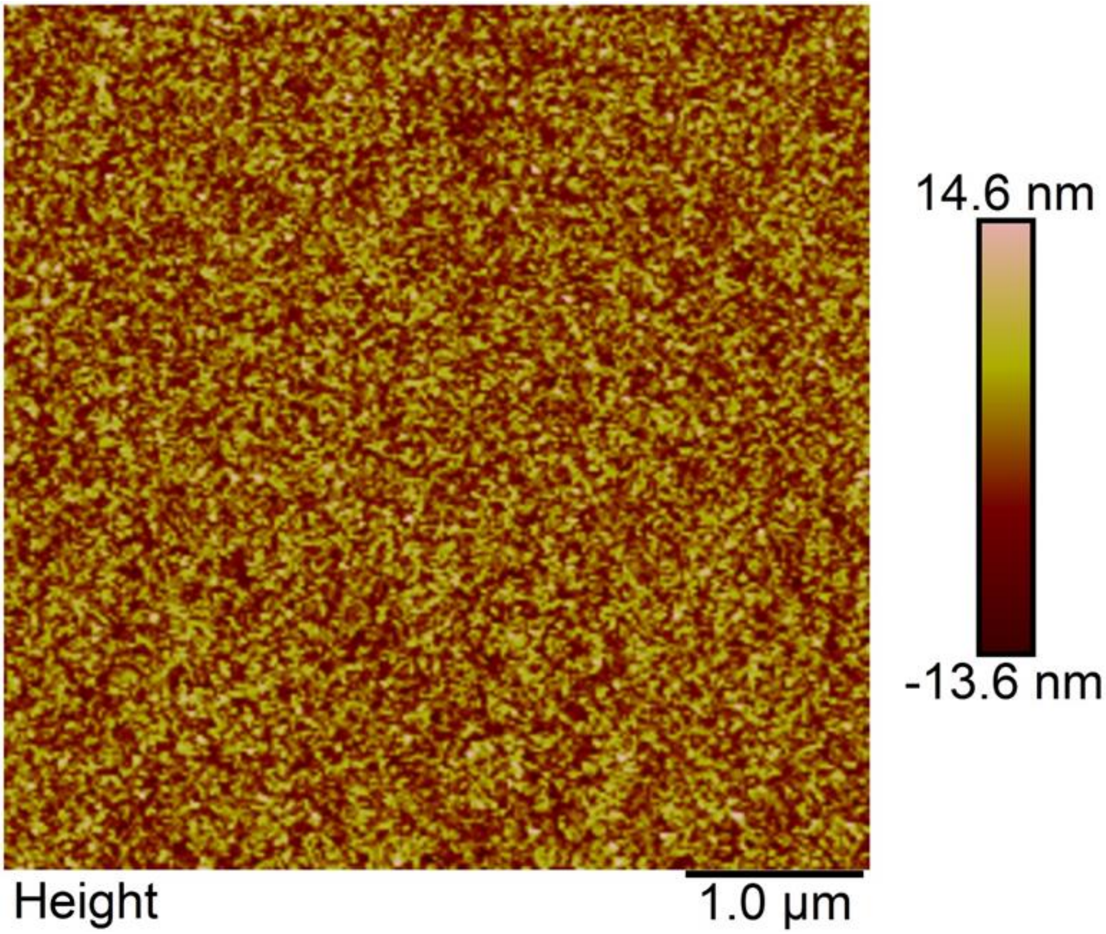

XPS was performed on samples deposited on platinum substrates at different deposition temperatures (170 and 200 °C) to assess the composition of the cobalt metal films grown over the span of the ALD window. A ~50 nm cobalt film (500 cycles) grown at 170 °C and a ~100 nm cobalt film (1000 cycles) grown at 200 °C were analyzed. Analysis of the high-resolution multiplex of the Co 2p core shell revealed binding energies which correspond to metallic cobalt (Co 2p$_{3/2}$ 778.11 eV and Co 2p$_{1/2}$ 793.15 eV) after as little as 0.5 minutes of sputtering, for both samples (**Figure 35a,b**). These binding energies are consistent with values obtained from a cobalt metal standard (Co $2p_{3/2}$ 778.11 eV and Co $2p_{1/2}$ 793.15 eV) (**Figure 35c**). XPS depth profiling was performed to assess the elemental composition of the films, which revealed > 98% pure cobalt metal upon sputtering, with trace impurities (< 1% each) of carbon, oxygen, and nitrogen (**Figure 36**). After 10 minutes of sputtering, of platinum and cobalt is observed, which may correspond to the formation of an interfacial alloy.[34]

Figure 35. High-resolution XPS multiplex of cobalt 2p region of a) 50 nm and b) 100 nm thick cobalt film grown on platinum using Co(^{tBu2}DAD)$_2$ and *tert*-butyl amine; c) reference cobalt film.

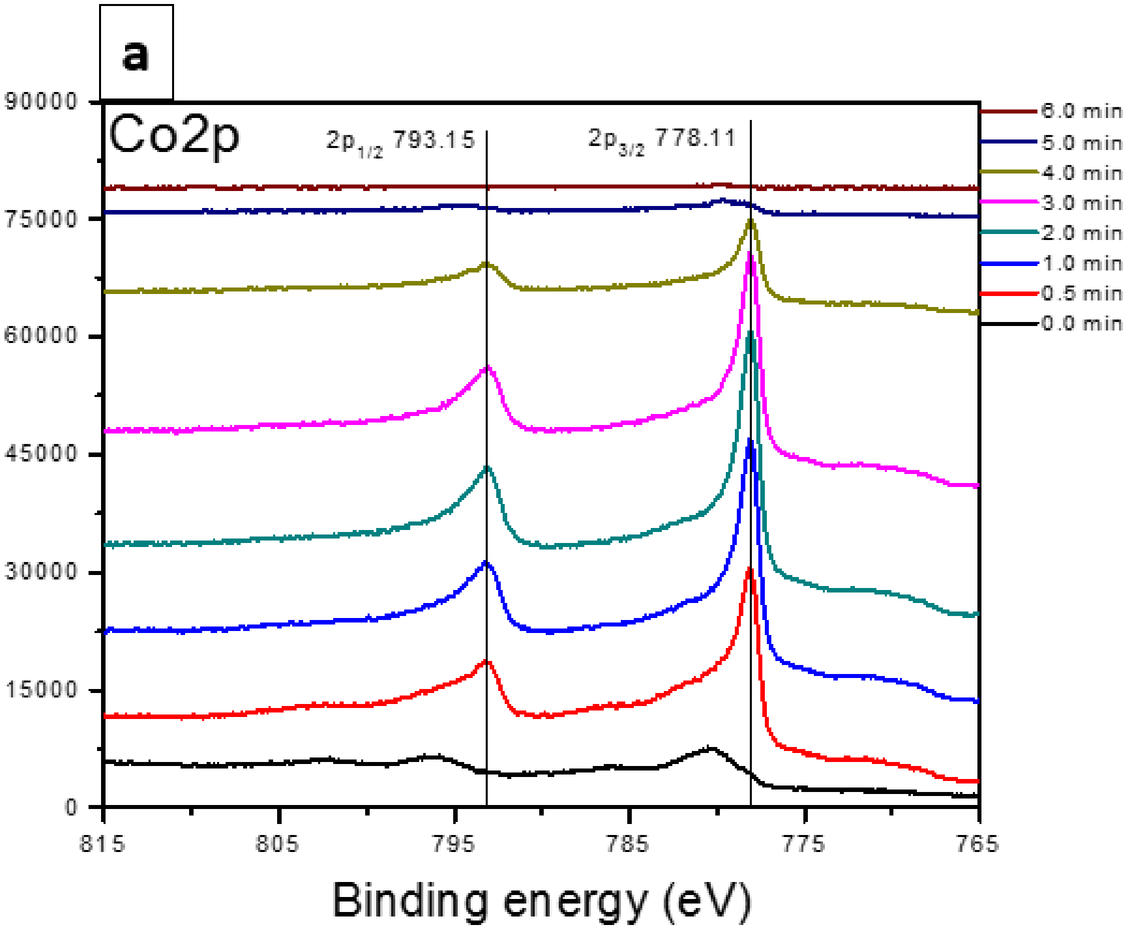

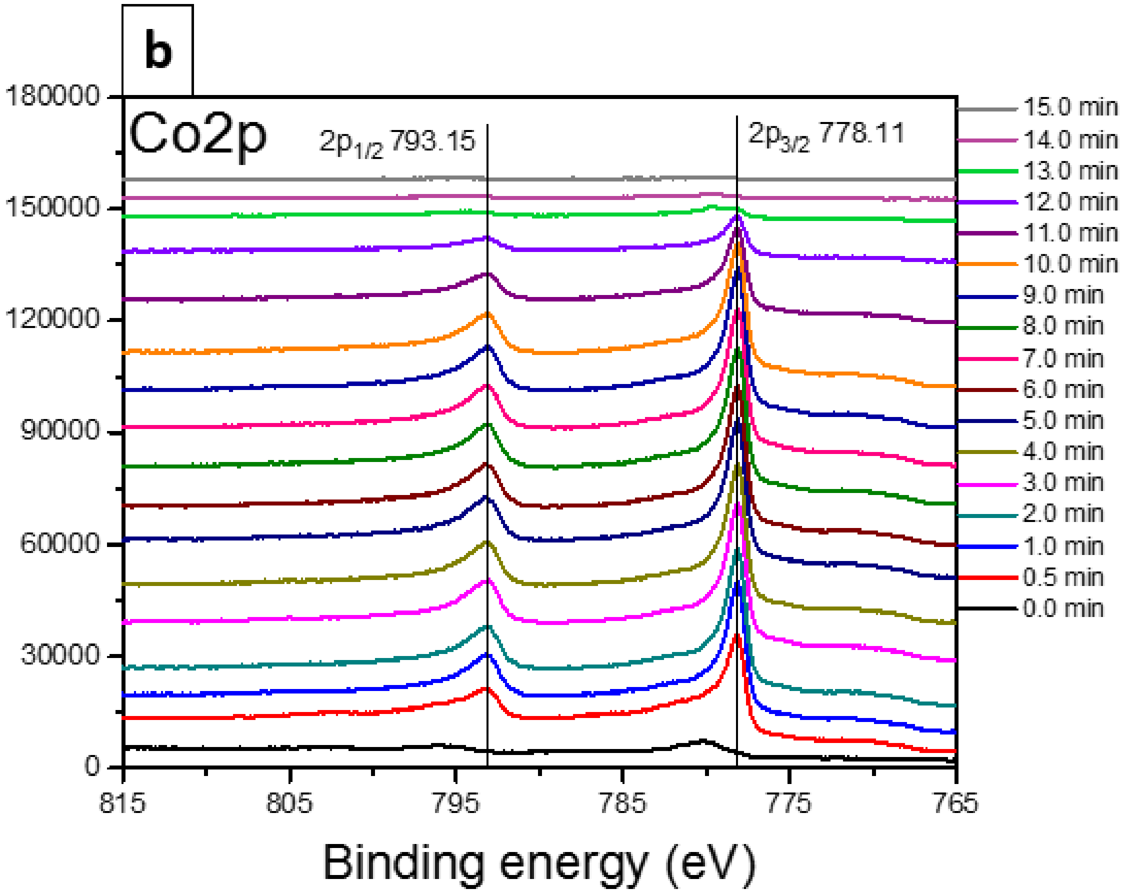
b
Co2p
$2p_{1/2}$ 793.15
$2p_{3/2}$ 778.11
180000
150000
120000
90000
60000
30000
0
815
805
795
785
775
765
Binding energy (eV)
15.0 min
14.0 min
13.0 min
12.0 min
11.0 min
10.0 min
9.0 min
8.0 min
7.0 min
6.0 min
5.0 min
4.0 min
3.0 min
2.0 min
1.0 min
0.5 min
0.0 min

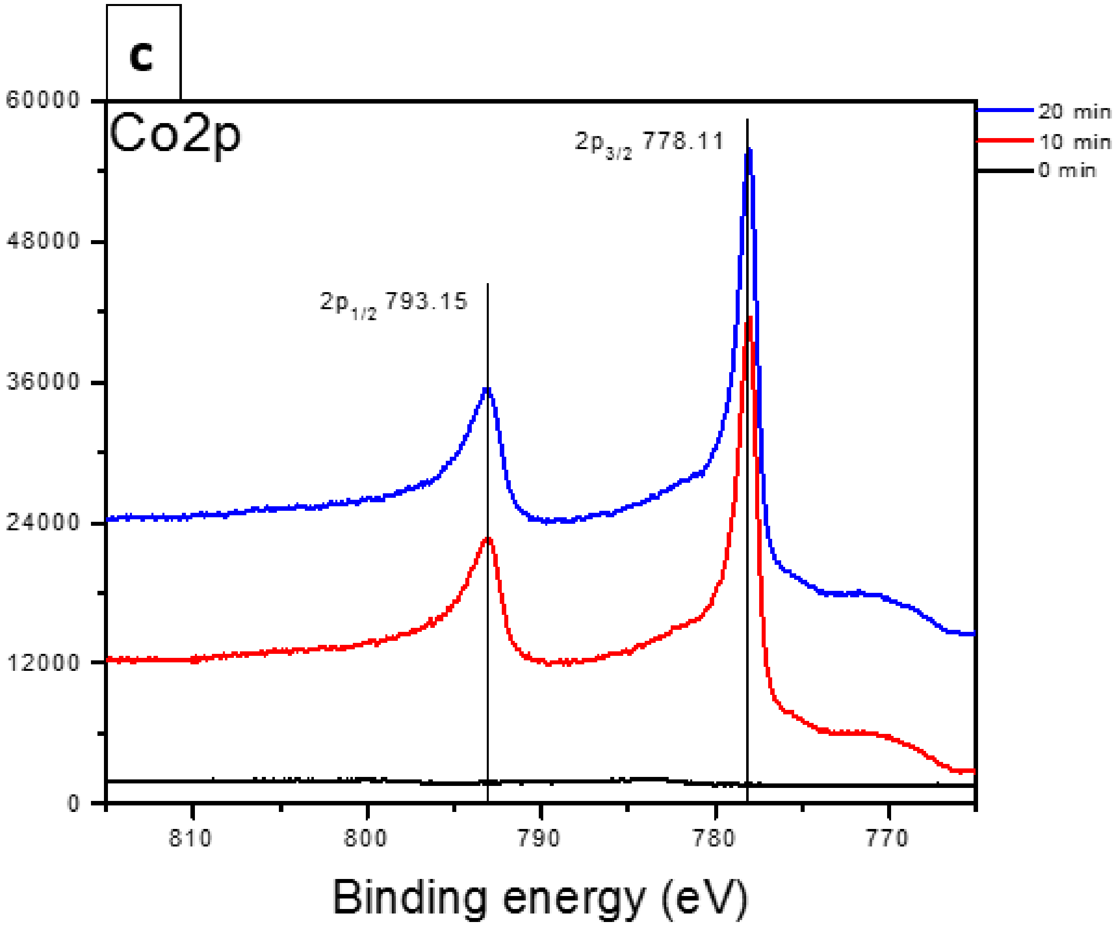
c
Co2p
2p$_{3/2}$ 778.11
2p$_{1/2}$ 793.15
20 min
10 min
0 min
60000
48000
36000
24000
12000
0
810
800
790
780
770
Binding energy (eV)

Figure 36. a) XPS depth profile and b) elemental compositions of a ~100 nm thick cobalt film grown on platinum at 200 °C, using Co(^{tBu2}DAD)$_2$ and *tert*-butyl amine.

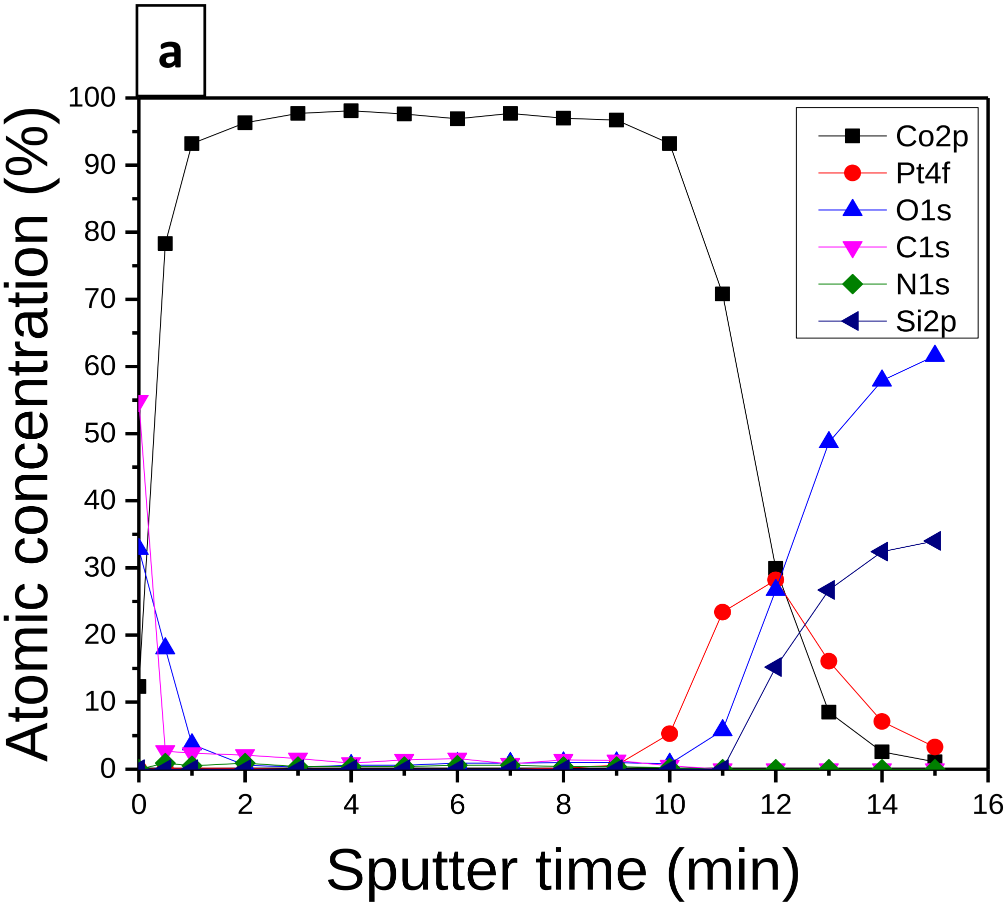

b

Sputter Time (min)	Co2p	Pt4f	O1s	C1s	N1s	Si2p
0.0	12.3	0.0	32.8	54.9	0.0	0.0
0.5	78.3	0.1	18.0	2.7	0.9	0.0
1.0	93.2	0.2	3.7	2.4	0.5	0.0
2.0	96.3	0.1	0.6	2.1	0.9	0.0
3.0	97.7	0.0	0.3	1.6	0.4	0.0
4.0	98.1	0.0	0.6	0.9	0.4	0.0
5.0	97.6	0.0	0.6	1.4	0.4	0.0
6.0	96.9	0.0	0.9	1.6	0.6	0.0
7.0	97.7	0.0	0.9	0.8	0.6	0.0
8.0	97.0	0.2	1.0	1.4	0.4	0.0
9.0	96.7	0.6	1.0	1.3	0.4	0.0
10.0	93.2	5.3	0.8	0.5	0.2	0.0
11.0	70.8	23.4	5.8	0.0	0.0	0.0
12.0	29.9	28.2	26.7	0.0	0.0	15.2
13.0	8.5	16.1	48.7	0.0	0.0	26.7
14.0	2.6	7.1	57.9	0.0	0.0	32.4
15.0	1.1	3.3	61.6	0.0	0.0	34.0

3.2.3 Description of Growth of Cobalt Metal on Metallic Substrates

The early stages of growth of metallic cobalt was assessed on a variety of metallic substrates (platinum, copper, and ruthenium), using Co(^{tBu2}DAD)$_2$ and *tert*-butyl amine as precursors (**Figure 37**). These experiments used the previously established saturative pulsing sequence of Co(^{tBu2}DAD)$_2$ (4.0 s), purge (10.0 s), *tert*-butyl amine (0.2 s), purge (10.0 s) for 25 – 500 cycles. Linear growth (0.98 Å/cycle) on platinum and copper substrates was observed for ≥ 25 cycles (~ 2.5 nm), and showed no nucleation delay. Growth of metallic cobalt films on ruthenium showed a delay in normal growth behavior before 200 cycles. The observed delay in normal growth on ruthenium is likely due to oxidation of the substrate surface, which is then reduced during the initial cycles, as described in Chapter 2.[34] Thicknesses were confirmed by cross-sectional SEM on platinum, copper, and ruthenium substrates (**Figure 38**).

Figure 37. Plot of thickness *versus* number of cycles for the early growth stages of cobalt metal on ruthenium, copper, and platinum substrates at 200 °C using Co(^{tBu2}DAD)$_2$ and *tert*-butyl amine.

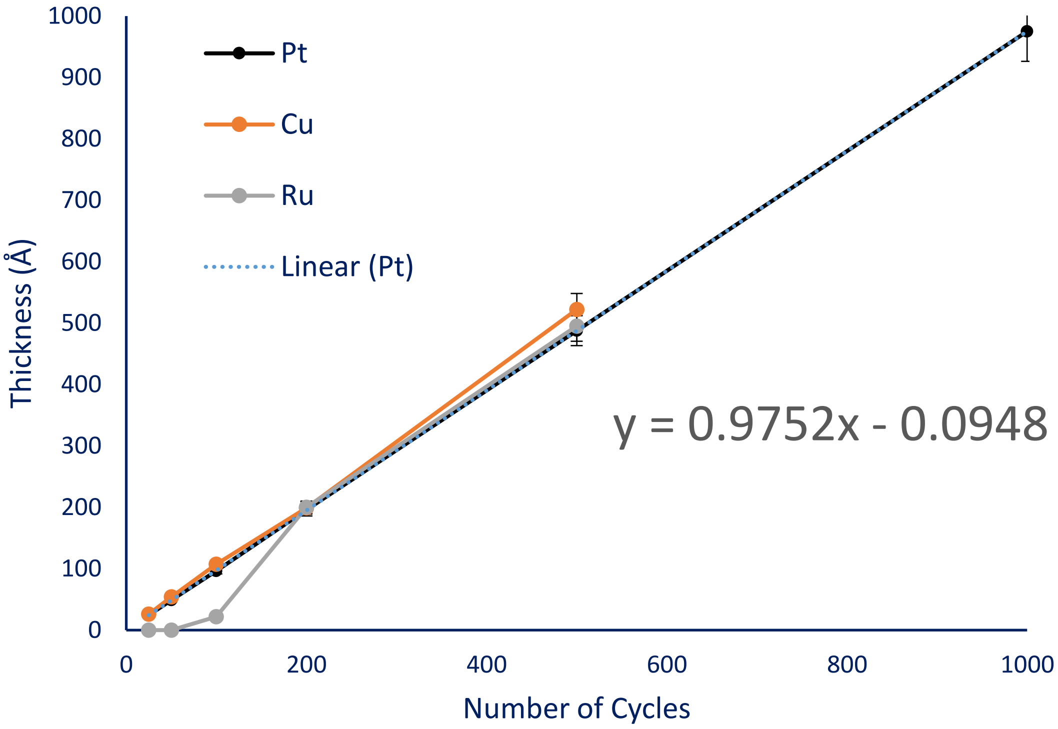

Figure 38. Cross-sectional SEM of a 20 nm thick cobalt metal film grown at 200 °C, on a) a platinum substrate b) a copper substrate.

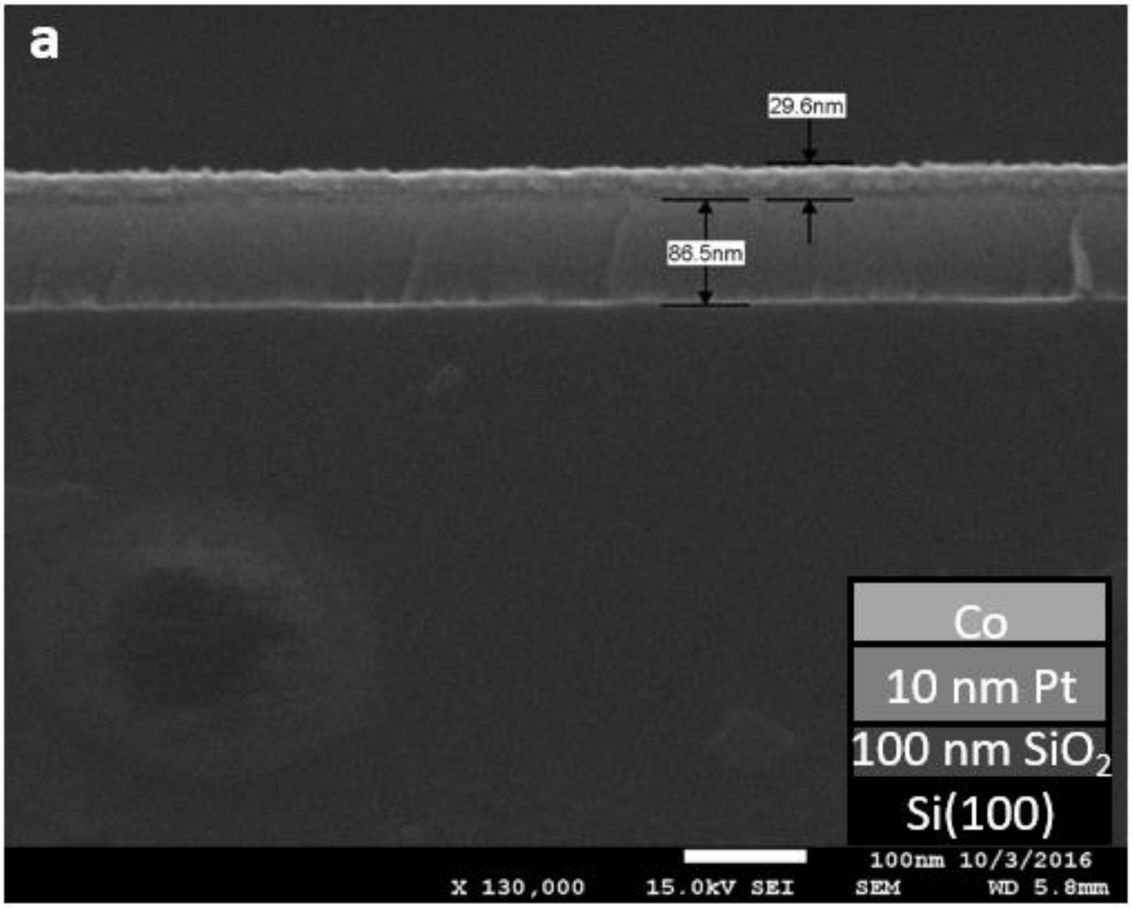

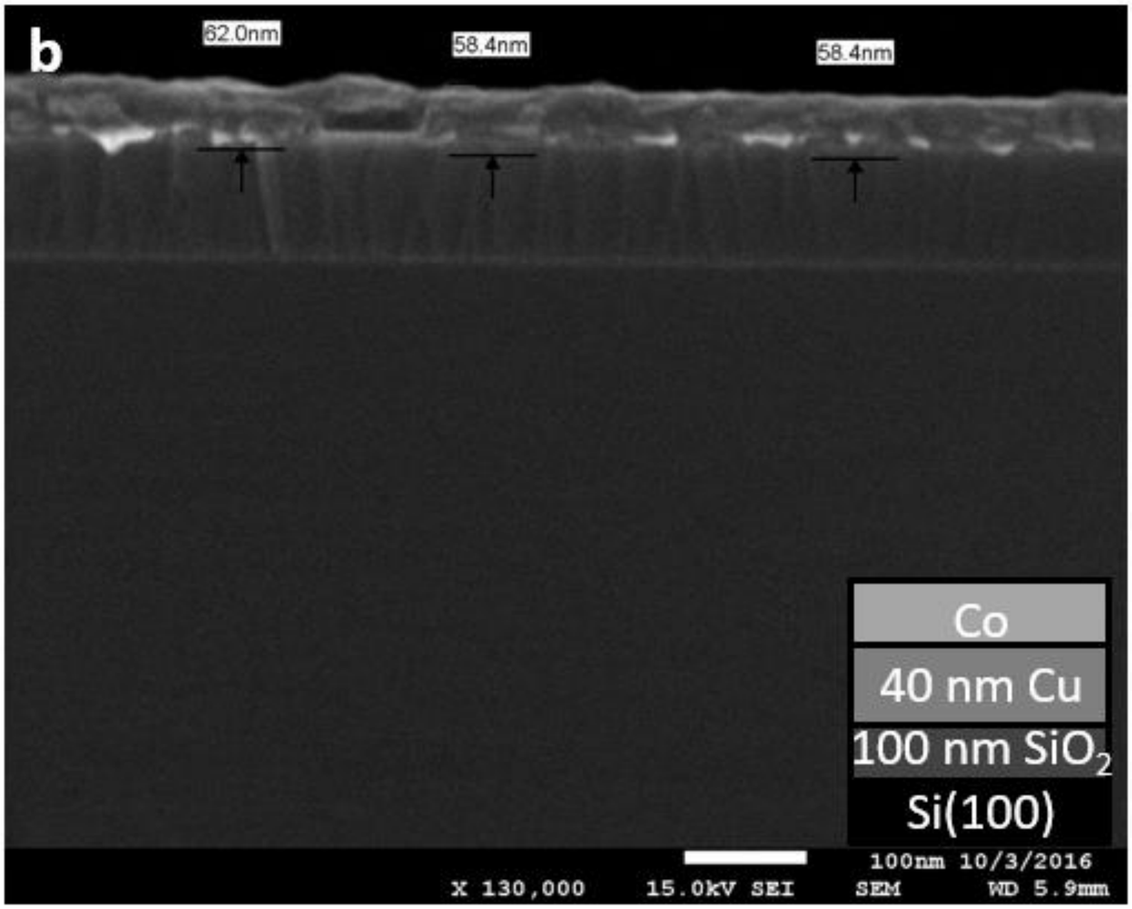

Bulk resistivities were measured for cobalt films deposited on platinum, copper, and ruthenium substrates (**Table 3**). Bulk resistivity was calculated as the product of sheet resistivity and film thickness. Bulk resitivities of cobalt films grown on platinum and copper at the early stages of growth suggest the formation of interfacial alloys.[34] In contrast, the resistivities of cobalt films grown on ruthenium at the early stages of growth match that of the bare ruthenium substrate, along with no growth observed by SEM, suggesting no formation of alloys. After 200 cycles, the resistivities of cobalt films grown on all of the metallic substrates are similar to that of resistivity value of 13.9 – 19.1 μΩ cm for a ~100 nm thick cobalt film grown on a platinum substrate.

Table 3. Resistivities of cobalt films grown on metallic substrates using Co(^{tBu2}DAD)$_2$ and *tert*-butyl amine.

Cycles	Ruthenium[a,b]	Copper[a,c]	Platinum[a,d]
25	55.8	1.7	46.9
50	55.4	1.7	44.7
100	48.6	2.3	36.8
200	19.1	13.9	18.9
500	15.5	14.4	14.2

[a] Values are in μΩ cm.
[b] The measured resistivity of the uncoated ruthenium substrate is 52.1 μΩ cm.
[c] The measured resistivity of the uncoated copper substrate is 1.7 μΩ cm.
[d] The measured resistivity of the uncoated platinum substrate is 42.6 μΩ cm.

3.2.4 Description of Attempted Growth of Metallic Cobalt on Non-Metallic Substrates

Film growth was attempted, under ALD conditions described previously in this chapter, on Si(100), SiO_2, Si-H, and CDO substrates. Films were not observed by SEM on any of these non-metallic substrates. The absence of cobalt metal films on these substrates up to 500 cycles was confirmed by cross-sectional SEM and EDS (**Figure 39)**.

Figure 39. a) Cross-sectional SEM of a CDO substrate after 500 deposition cycles at 200 °C b) EDS of a CDO substrate after 500 deposition cycles at 200 °C.

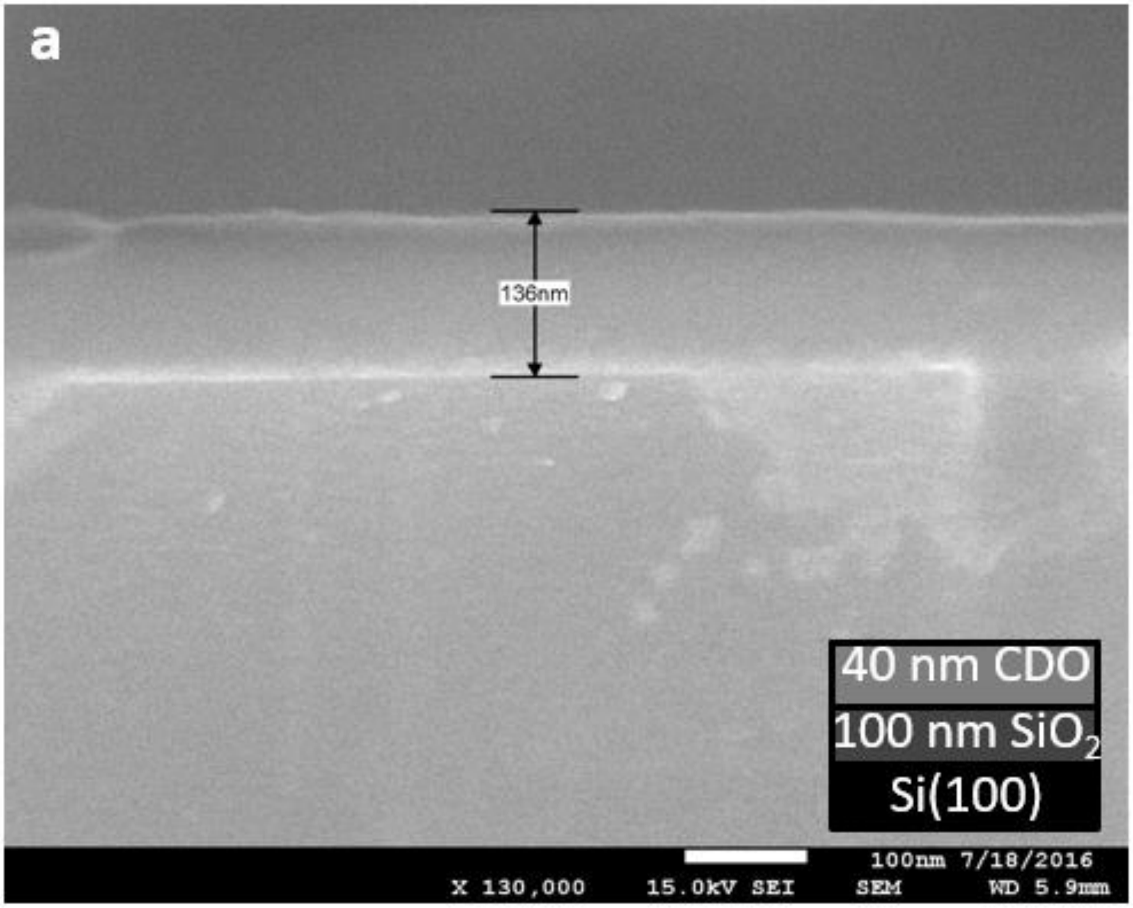

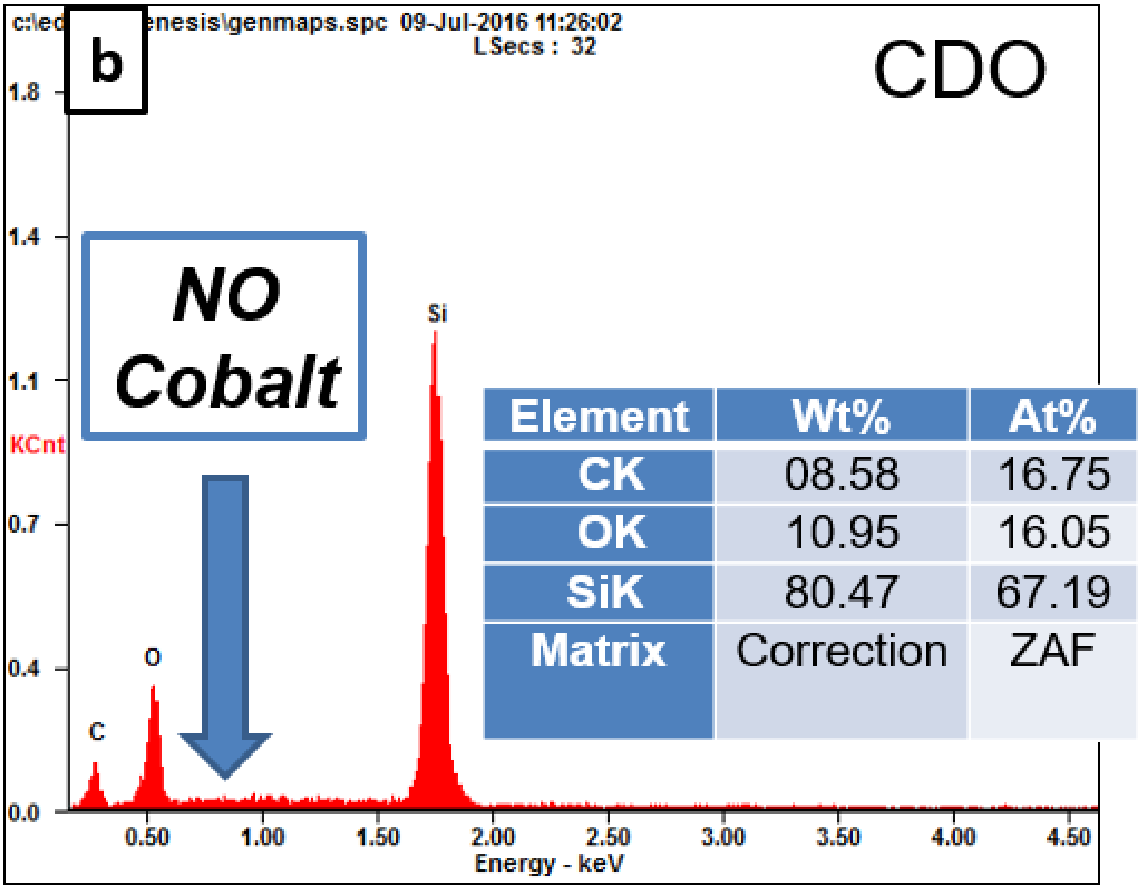

Element	Wt%	At%
CK	08.58	16.75
OK	10.95	16.05
SiK	80.47	67.19
Matrix	Correction	ZAF

The temperature dependence of substrate-selectivity of this process, known as the selectivity window, was explored. A series of 200-cycle depositions was carried out with the saturative precursor recipe of Co(^{tBu2}DAD)$_2$ (4.0 s), purge (10.0 s), *tert*-butyl amine (0.2 s), purge (10.0 s), at varying temperatures. Since applications for selective depositions will require ≤ 20 nm of cobalt metal, and the observed growth rate for this process is ~1.0 Å/cycle, a 200 cycle limit was imposed to provide relevant insights. The depositions were carried out from 160 – 220 °C (**Figure 40)**. None of the deposition temperatures resulted in the deposition of cobalt on any of the non-metallic substrates. The absence of cobalt metal films on these substrates was confirmed by cross-sectional SEM and EDS.

Figure 40. Area-selective ALD temperature windows, where no growth was observed on Si(100), Si-H, and CDO substrates after 200 cycles.

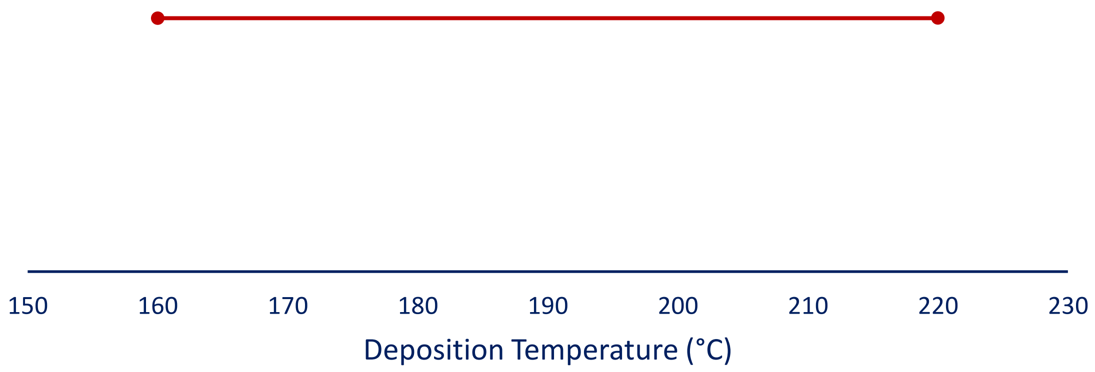

3.2.5 Trial Depositions for Cobalt Metal using Co(^{tBu2}DAD)$_2$ and Other Alkyl Amines

The growth of metallic cobalt was explored using diethyl amine and triethyl amine as alternative amine precursors. Films were grown using the pulsing sequence Co(^{tBu2}DAD)$_2$ (4.0 s), purge (10.0 s), diethyl amine (0.2 s)/ triethyl amine (0.2 s), purge (10.0 s) at a deposition temperature of 200°C, for 200 cycles. A growth rate of 0.97 Å/cycle was observed using diethyl amine on platinum substrates. (**Figure 41a**). The bulk resistivity of the resulting film was 21.3 μΩ cm. Films growth was not observed by cross-sectional SEM on Si(100), SiO$_2$, Si-H, and CDO substrates, and no further investigation was conducted on this process. Similarly, cobalt metal depositions on platinum substrates using triethylamine as a precursor resulted in no observable films (as confirmed by cross-sectional SEM) (**Figure 41b**). No further investigation was pursued.

Figure 41. Cross-sectional SEM after 200 deposition cycles at 200 °C using Co(^{tBu2}DAD)$_2$ and a) diethyl amine b) triethyl amine.

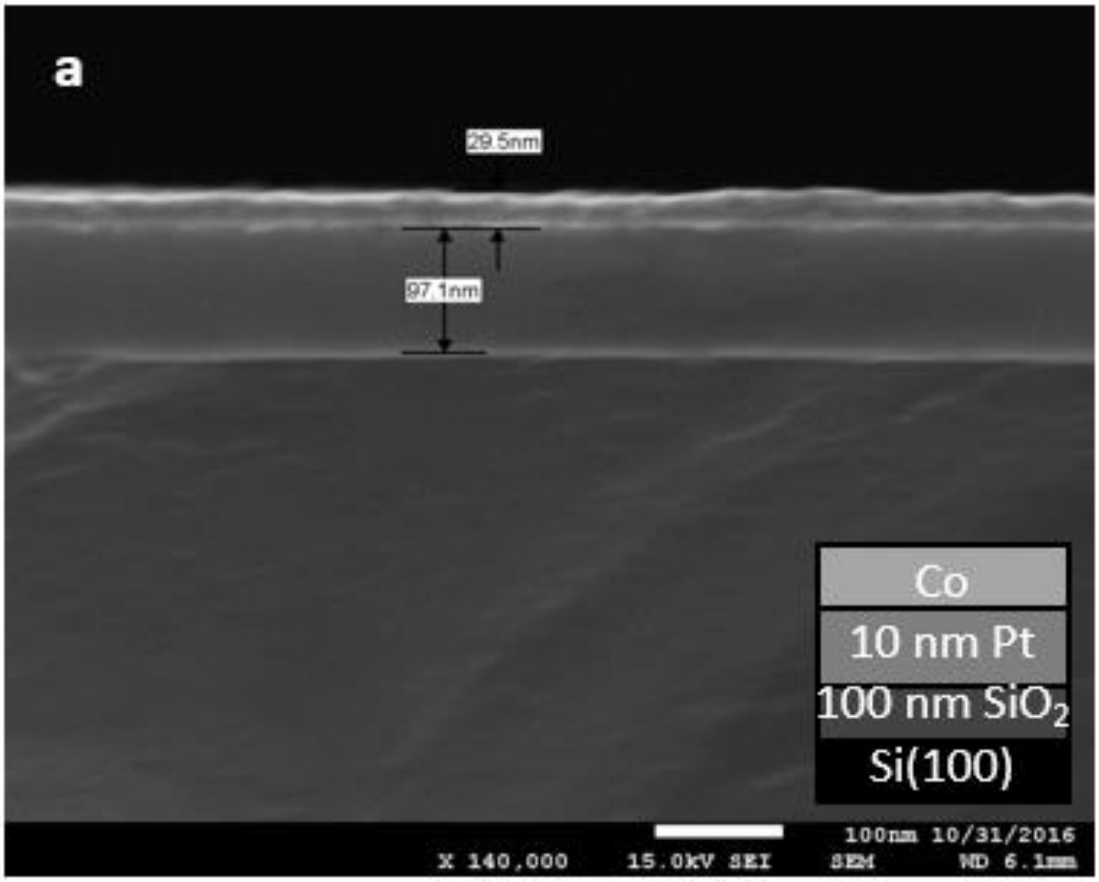

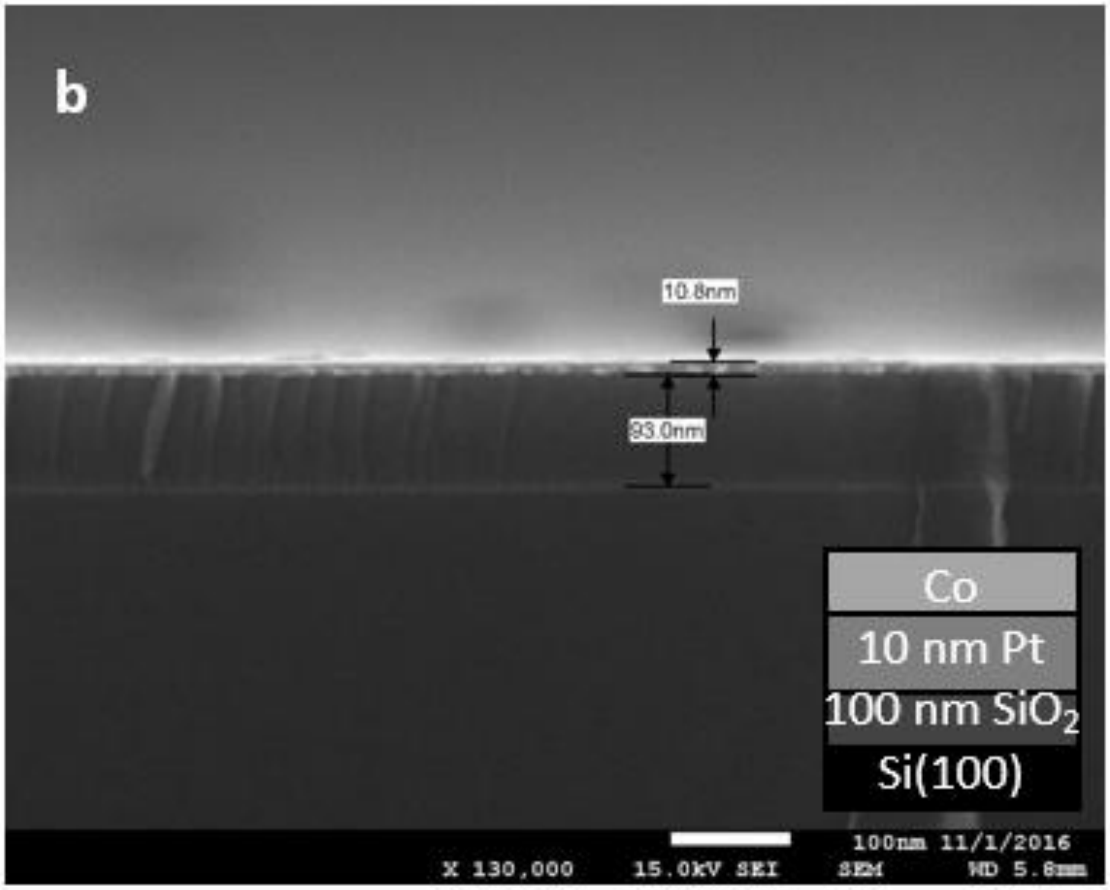

3.2.6 Effects of the Purity of the N_2 Carrier Gas on Film Growth

Initial experiments for the deposition of metallic cobalt using $\mathrm{Co(^{tBu2}DAD)_2}$ and *tert*-butyl amine were performed using N_2 purified from ambient air, produced from a nitrogen generator, as the carrier and purge gas. The exact purity of the produced N_2 was not determined, but was < 99.999% N_2, with trace impurities of oxygen. Films were grown using the pulsing sequence $\mathrm{Co(^{tBu2}DAD)_2}$ (4.0 s), purge (10.0 s), *tert*-butyl amine (0.2 s), purge (10.0 s) at a deposition temperature of 200°C, for a varying number of cycles. The growth rate obtained using the lower purity carrier gas was 0.33 Å/cycle (**Figure 42**). In contrast, the growth rate obtained with the ultra-high purity carrier gas was 0.98 Å/cycle.

The difference in growth rate for this process, with only the purity of the carrier gas varying, is likely due to the formation of cobalt (II) oxide in the deposited film. The presence of cobalt (II) oxide inhibits growth of the metallic cobalt film, since this process shows inherent selectivity for deposition on metallic substrates over non-metallic substrates. XPS analysis of a 100 nm thick cobalt film reveals oxidation throughout the film, even after eight minutes of argon ion sputtering (**Figure 43**). These results show the significant impact that the purity of the carrier gas has on the process using Co(^{tBu2}DAD)$_2$ and *tert*-butyl amine to deposit thin films of metallic cobalt.

Figure 42. Plot of thickness *versus* number of cycles for cobalt metal growth on platinum substrates at 200 °C using Co(^{tBu2}DAD)$_2$ and *tert*-butyl amine, using lower purity N$_2$ carrier gas.

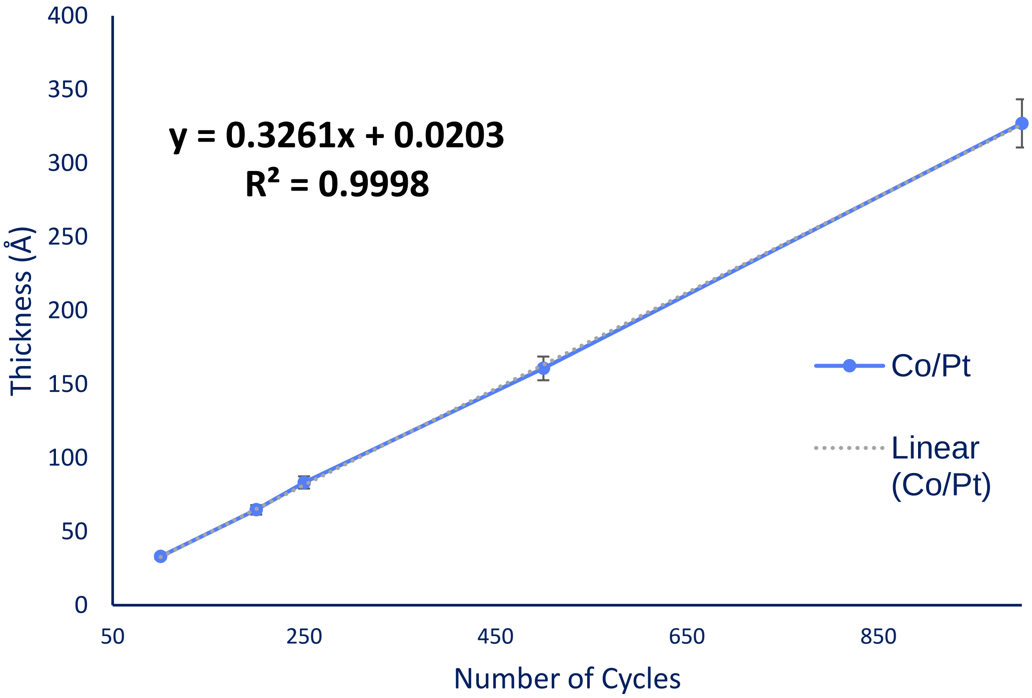

Figure 43. High-resolution XPS multiplex of cobalt 2p region of an 100 nm thick cobalt film grown on platinum, at 200 °C, using N_2 produced by a nitrogen generator, Co(^{tBu2}DAD)$_2$, and *tert*-butyl amine.

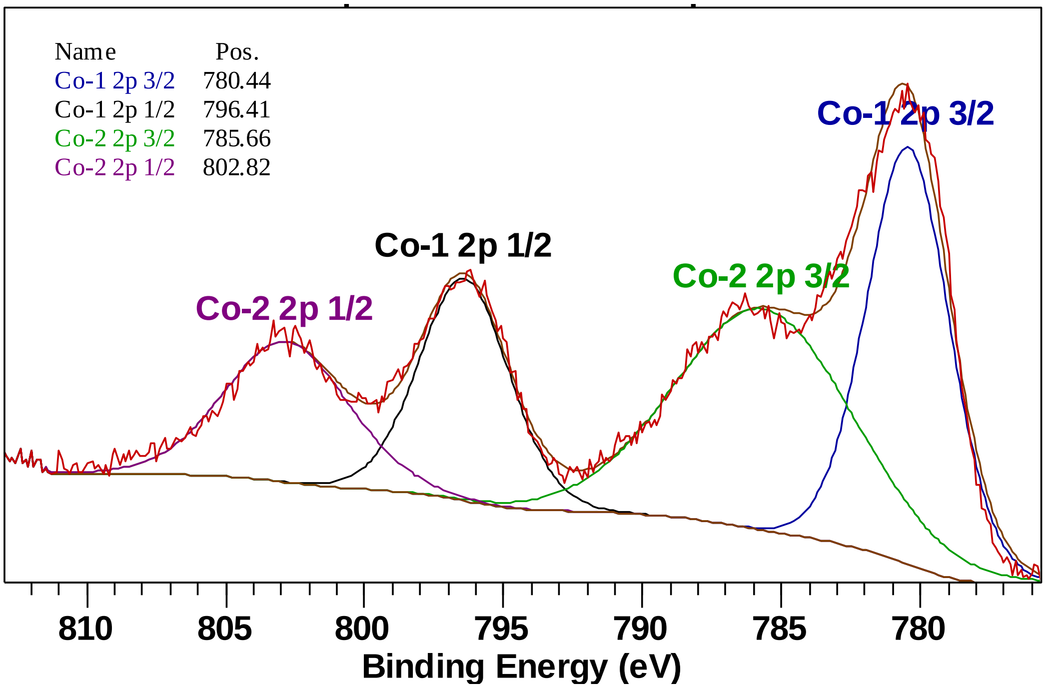

3.3 Conclusions

The growth of cobalt metal by low temperature thermal ALD from Co(^{tBu2}DAD)$_2$ and *tert*-butyl amine at 200 °C on various substrates was demonstrated. On platinum and copper substrates, a linear growth rate of 0.98 Å/cycle from 25 – 500 cycles was observed for plots of thickness versus the number of cycles. The y-intercept for this plot was within experimental error of zero, indicating no nucleation delay, with normal growth observed for as little as 2.5 nm of cobalt on platinum and copper substrates. Growth on ruthenium substrates showed a delay of 200 cycles before a normal growth rate was observed, with no films observed after 25 and 50 cycles. As described in previous work (Chapter 2), rapid growth is observed between 100 and 200 cycles, which suggests the occurrence of decomposition growth at the early stages of growth, and is likely due to surface oxidation of the ruthenium substrate. Cobalt metal films on platinum substrates after 100 cycles (~10 nm thick) and 1000 cycles (~100 nm) were analyzed by AFM, with respective rms surface roughnesses of 0.22 nm (2.2% of total thickness), and 3.07 nm (3.1% of total thickness). The rms roughness values show that these films are smooth and continuous over a wide range of thicknesses. XPS analyses reveal that this process deposits high-purity cobalt metal. Films grown on ruthenium, platinum, and copper substrates showed low resistivities of < 20 μΩ cm after 200 cycles. Growth of cobalt metal by this process is inherently selective for growth on metallic substrates over non-metallic substrates, with no film growth observed after 500 cycles on Si(100), Si-H, thermal SiO_2 and CDO substrates. Selective deposition of cobalt metal on metallic substrates over non-metallic substrates occurs over a selectivity window of 160 – 220 °C.

3.4 Experimental Section

A Picosun R-75BE ALD reactor was used for the thin film deposition experiments. Ultra-high purity nitrogen (99.999%, purchased from Airgas) was used as the carrier and purge gas for all depositions, with the exception of the depositions performed to assess the effect of the purity of the carrier gas. Nitrogen (< 99.999%) was used as both the carrier and purge gas and was purified from ambient air using a Texol GeniSys nitroGenerator, for experiments assessing the effect of the purity of the carrier gas. The ALD reactor had a constant flow of the same ultra-high purity nitrogen in the deposition chamber for all depositions, with a pressure of 6 – 9 Torr. The low-temperature ALD of metallic cobalt thin films was performed using $Co(^{tBu2}DAD)_2$ and *tert*-butyl amine as precursors. $Co(^{tBu2}DAD)_2$ was prepared according to a literature procedure.[92] All alkyl amines used in depositions (*tert*-butyl amine, diethyl amine, and trimethylamine) were purchased from Sigma Aldrich. In initial growth trials, the source temperature for Co(^{tBu2}DAD)$_2$ was found to be optimum at 130 °C under the reactor pressure, and Co(^{tBu2}DAD)$_2$ was delivered by a Picosun solid state booster, while *tert*-butyl amine was delivered by a vapor-draw ampule at 20 °C. Substrate temperatures were varied between 160 and 220 °C. Film growth experiments used to assess selectivity were performed using the pulse sequence Co(^{tBu2}DAD)$_2$ (4.0 s)/N$_2$ purge (10.0 s)/*tert*-butyl amine (0.2 s)/N$_2$ purge (10.0 s) at 200 °C. For the selectivity temperature window experiments, the same pulse and purge sequence was used, but the deposition temperatures were varied from 160 – 220 °C. ALD growth studies were performed on Ru (13 nm)/TaN (2 nm)/SiO$_2$ (100 nm)/Si(100), Cu (33 nm)/TaN (7 nm)/SiO$_2$ (100 nm)/Si(100), Pt (10 nm)/SiO$_2$ (100 nm)/Si(100), Si(100) with native oxide, Si-H, thermal SiO$_2$ (100 nm)/Si(100), and CDO (~40 nm)/SiO$_2$ (100 nm)/Si(100) substrates. Si-H substrates were prepared by treating Si(100) with native oxide substrates with a 2% aqueous HF solution, followed by rinsing with deionized water and then drying with a stream of clean, dry air. The other substrates were used as received, except that they were rinsed sequentially with isopropanol and deionized water and then were dried with a stream of clean, dry air. One substrate of each kind, a 2 x 2 cm^2 coupon, was used in each experiment.

Film thicknesses were determined using cross-sectional SEM collected on a JEOL-6510LV electron microscope. The growth rates were determined by dividing the measured film thicknesses by the number of deposition cycles. Film thicknesses were measured at a minimum of three positions on each film to evaluate the uniformity. EDS was carried out on the JEOL-6510LV electron microscope using an Ametek EDAX system with Genesis Spectrum software. The accelerating voltage for the EDS measurements was 6 kV. AFM measurements were conducted using a Bruker BioScope Catalyst AFM using contact mode. XPS measurements were conducted using an Al Kα (1486.6 eV) X-ray source at a chamber base pressure of 10^{-10} Torr. Spectra were recorded using a 16-channel detector with a hemispherical analyzer. Sputtering was performed using argon ions supplied by an argon sputter gun positioned at a 45° angle with respect to the substrate normal. Each sample was sputtered over a 2×2 mm^2 area and measured over a 0.8×0.8 mm^2 area. Cobalt metal standards were sputtered with 5 keV argon ions. An uncoated platinum substrate (Pt (10 nm)/SiO_2 (100 nm)/Si(100)) was used as a standard for platinum and was sputtered with 3 keV argon ions. The ALD-grown cobalt films on platinum were sputtered with 3 keV argon ions. Sheet resistivity measurements were obtained using a Jandel 4-point probe in combination with a Keithley 2400 SourceMeter and a Keithley 2182A Nanovoltmeter. All films grown on metal substrates passed the Scotch tape test.

CHAPTER 4 LOW TEMPERATURE GROWTH AND SUBSTRATE SELECTIVITY OF NICKEL METAL THIN FILMS BY THERMAL ATOMIC LAYER DEPOSITION FROM BIS(1,4-DI-*TERT*-BUTYL-1,3-DIAZADIENYL)NICKEL AND ALKYL AMINES

4.1 Introduction

The growth of nickel metal thin films by ALD has received growing interest due to the applications in microelectronic devices as electrodes and contacts in transistors,[85] as a precursor material for NiSi and $NiSi_2$,[85] and as seed layers for copper deposition.[86] Although nickel metal thin films have been deposited by various methods described in Chapter 1, few thermal ALD methods have been reported. Since the Co^{2+} and Ni^{2+} have similar electrochemical potentials of -0.28V and -0.26V to their metallic species,[54] respectively, we hypothesized that the use of alkyl amines would afford an analogous thermal ALD process for nickel metal from $Ni(^{tBu2}DAD)_2$.

In this chapter, the growth of metallic nickel was demonstrated on a variety of substrates using $Ni(^{tBu2}DAD)_2$ and *tert*-butyl amine as precursors (**Figure 44**). When using *tert*-butyl amine, a growth rate of 0.60 Å/cycle was achieved in the ALD window of 180 – 195 °C. The resultant films were continuous, featured high-purity metallic nickel films, and exhibited low resistivity values when grown on a metallic substrates. Trial depositions using other alkyl amines are also discussed in this chapter.

Figure 44. General reaction scheme for the deposition of nickel metal thin films from Ni(^{tBu2}DAD)$_2$ and *tert*-butyl amine by thermal ALD.

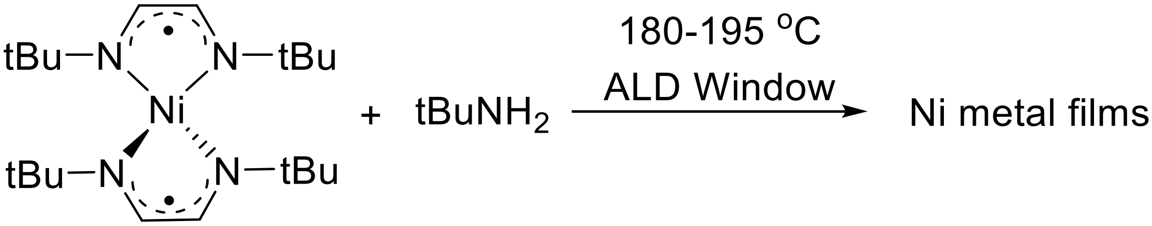

4.2 Results and Discussion

4.2.1 Low Temperature ALD Study of Nickel Metal from Ni(^{tBu2}DAD)$_2$ and *tert*-butyl Amine

Experiments to demonstrate ALD growth of metallic nickel using Ni(^{tBu2}DAD)$_2$ and *tert*-butyl amine were performed on platinum substrates. First, self-limiting growth was established by varying the pulse length of one co-reagent at a time while keeping all other conditions constant, then plotting the growth rate as a function of precursor pulse length. Experiments to evaluate Ni(^{tBu2}DAD)$_2$ saturation used a pulsing sequence of Ni(^{tBu2}DAD)$_2$ (varied), purge (10.0 s), *tert*-butyl amine (0.2 s), purge (10.0 s) for 500 cycles, at a deposition temperature of 180 °C. Self-limited growth was observed after ≥ 4.0 s pulse lengths of Ni(^{tBu2}DAD)$_2$, as evidenced by a constant growth rate of 0.60 Å/cycle (**Figure 45**). Saturation of *tert*-butyl amine was determined by varying the pulse length of *tert*-butyl amine, keeping all other deposition parameters constant. These experiments used a pulsing sequence of Ni(^{tBu2}DAD)$_2$ (5.0 s), purge (10.0 s), *tert*-butyl amine (varied), purge (10.0 s) for 500 cycles, at a deposition temperature of 180 °C. Self-limited growth was observed after ≥ 0.1 s pulse lengths of *tert*-butyl amine, as evidenced by a constant growth rate of 0.60 Å/cycle (**Figure 46**).

Figure 45. Plot of growth rate of nickel metal on platinum substrates *versus* pulse length of Ni(^{tBu2}DAD)$_2$ after 500 cycles, using Ni(^{tBu2}DAD)$_2$ and *tert*-butyl amine as precursors.

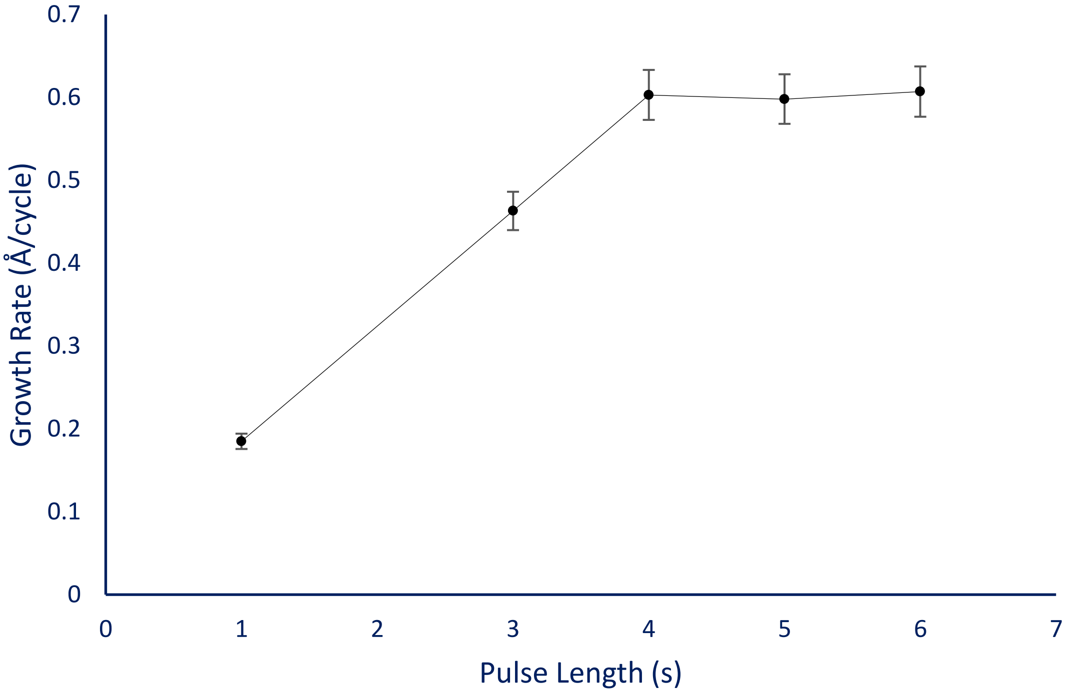

Figure 46. Plot of growth rate of nickel metal on platinum substrates *versus* pulse length of *tert*-butyl amine after 500 cycles, using Ni(^{tBu2}DAD)$_2$ and *tert*-butyl amine as precursors.

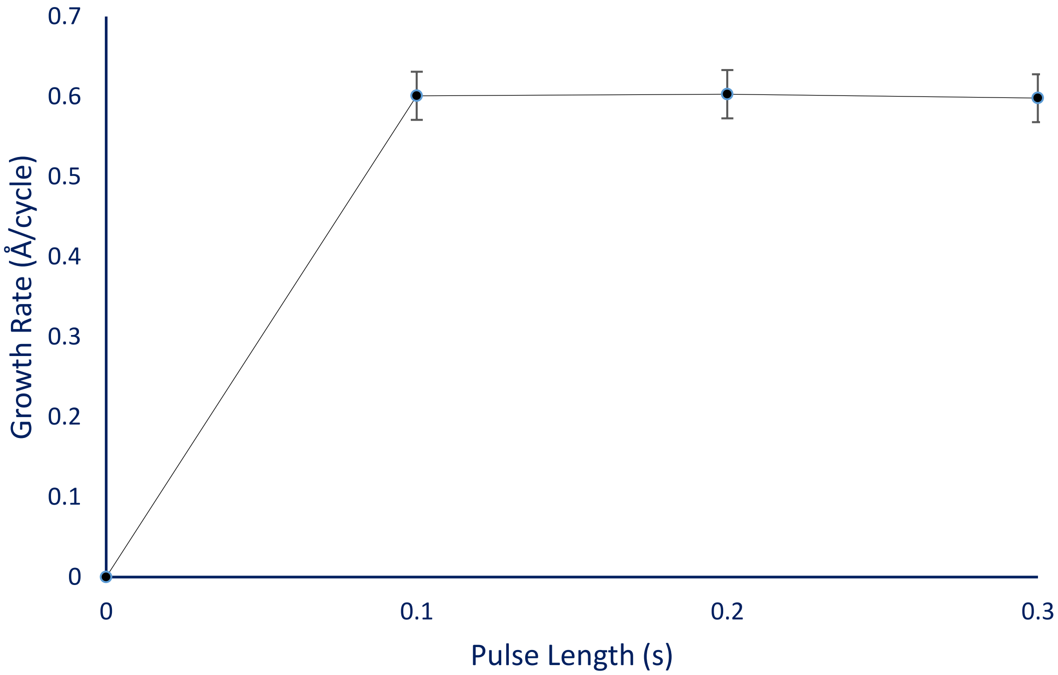

To assess temperature dependence, experiments to construct an ALD window were performed. Films were grown using a saturative pulsing sequence of Ni(^{tBu2}DAD)$_2$ (5.0 s), purge (10.0 s), *tert*-butyl amine (0.1 s), purge (10.0 s) at temperatures within 160 – 220 °C, each for 250 cycles. Due to the decomposition temperature of 230 °C for Ni(^{tBu2}DAD)$_2$, higher temperatures were not evaluated.[92] A constant growth rate of 0.60 Å/cycle was observed between 180 – 195 °C for films deposited on platinum substrates (**Figure 47**). Cross-sectional SEM images revealed uniform, continuous films deposited on platinum in the ALD window.

Figure 47. Plot of growth rate *versus* deposition temperature for nickel metal growth on platinum substrates after 250 cycles using Ni(^{tBu2}DAD)$_2$ and *tert*-butyl amine.

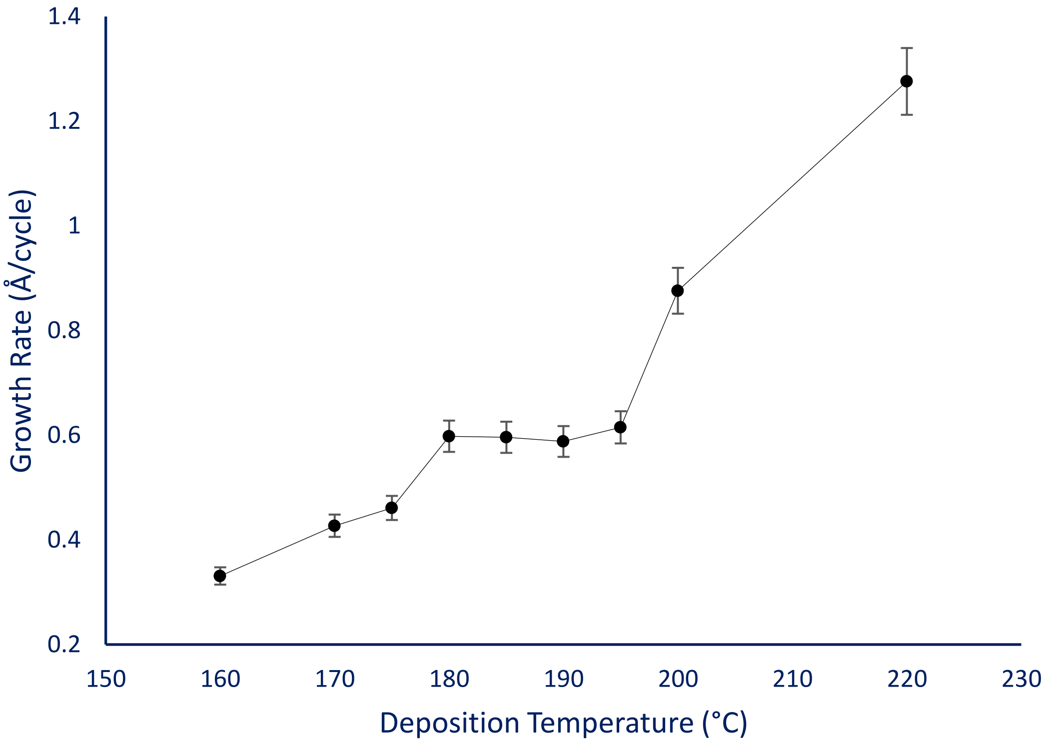

To evaluate the growth of this process as a function of number of ALD cycles, the same saturative dose pulsing sequence used for the ALD window determination was used, at a deposition temperature of 180 °C, while varying the number of cycles. The resulting plot shows a slope of 0.60, which corresponds to a constant growth rate of 0.60 Å/cycle on platinum from 25 – 1000 cycles (**Figure 48**). The y-intercept of 1.22 is within experimental error of zero, indicating that as few as 50 cycles (~3.0 nm) are needed to achieve normal ALD growth without a nucleation delay.

Figure 48. Plot of thickness *versus* number of cycles for nickel metal growth on platinum substrates at 200 °C using Ni(^{tBu2}DAD)$_2$ and *tert*-butyl amine.

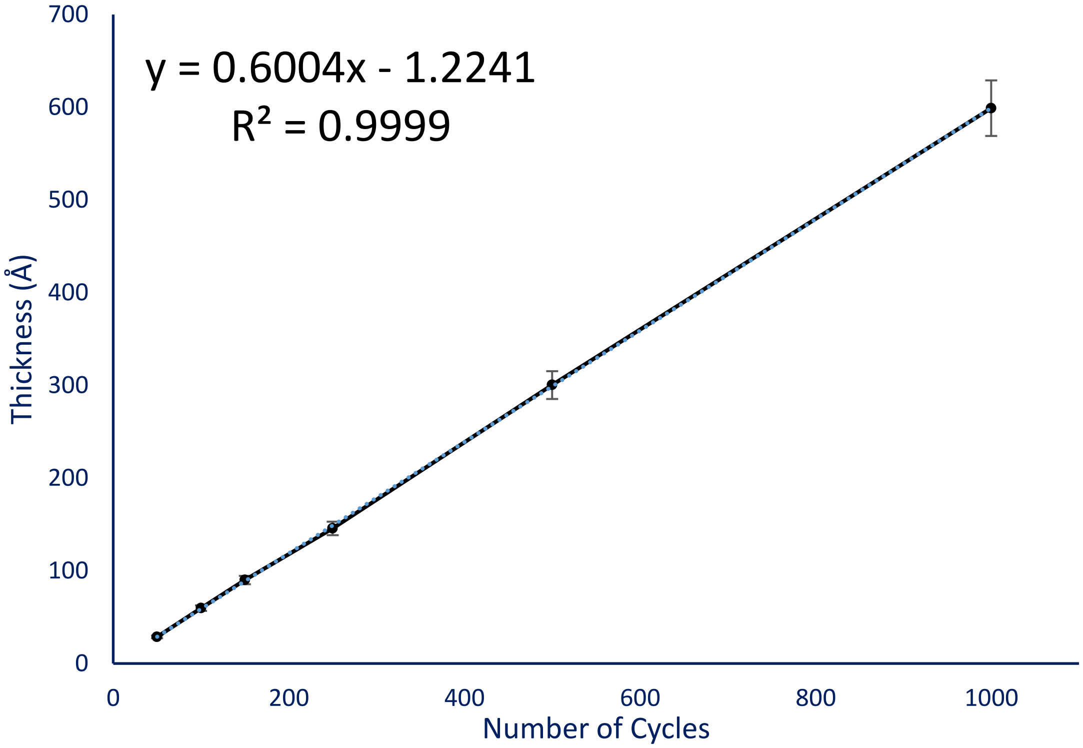

4.2.2 Characterization of Films Deposited by ALD using Ni(^{tBu}DAD)$_2$ and *tert*-butyl Amine

XRD was performed on a ~60 nm thick nickel film grown on a platinum substrate to assess the degree of crystallinity of the as-deposited film (**Figure 49**). The XRD pattern displayed reflections consistent with that of previously determined XRD pattern for the bare substrate. Nickel metal reflections appear in a similar region to the peak from the platinum substrate, making the information from this XRD spectrum inconclusive.

Figure 49. X-ray diffraction pattern for a ~60 nm thick nickel metal film grown on a platinum substrate at 180 °C using Ni(^{tBu2}DAD)$_2$ and *tert*-butyl amine.

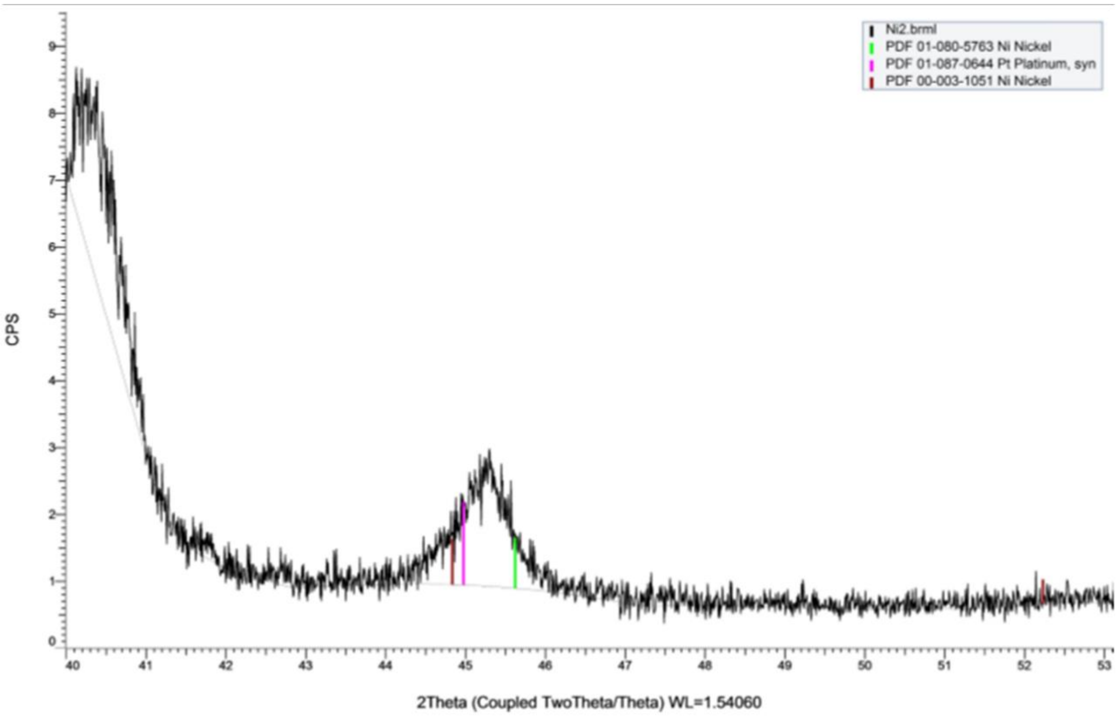

AFM was performed to examine the surface topologies of nickel films of different thicknesses (~18 nm and ~60 nm) grown on platinum substrates. The uncoated platinum substrate has been previously measured to have an rms roughness value of 0.19 nm.[34] The ~18 nm thick film had an rms roughness value of 0.45 nm over the full 5 x 5 μm^2 area (**Figure 50**), which corresponds to 2.5% of the total film thickness. The ~60 nm thick film had an rms roughness value of 1.52 nm over the full 5 x 5 μm^2 area (**Figure 51**), which corresponds to 2.5% of the total film thickness. These rms roughness values indicate that over a wide span of thicknesses, the as-deposited films from this process are extremely smooth.

Figure 50. Atomic force microscopy 5 x 5 μm^2 area image of a ~18 nm thick nickel metal film grown on a platinum substrate at 180 °C using Ni(^{tBu2}DAD)$_2$ and *tert*-butyl amine; rms roughness = 0.45 nm.

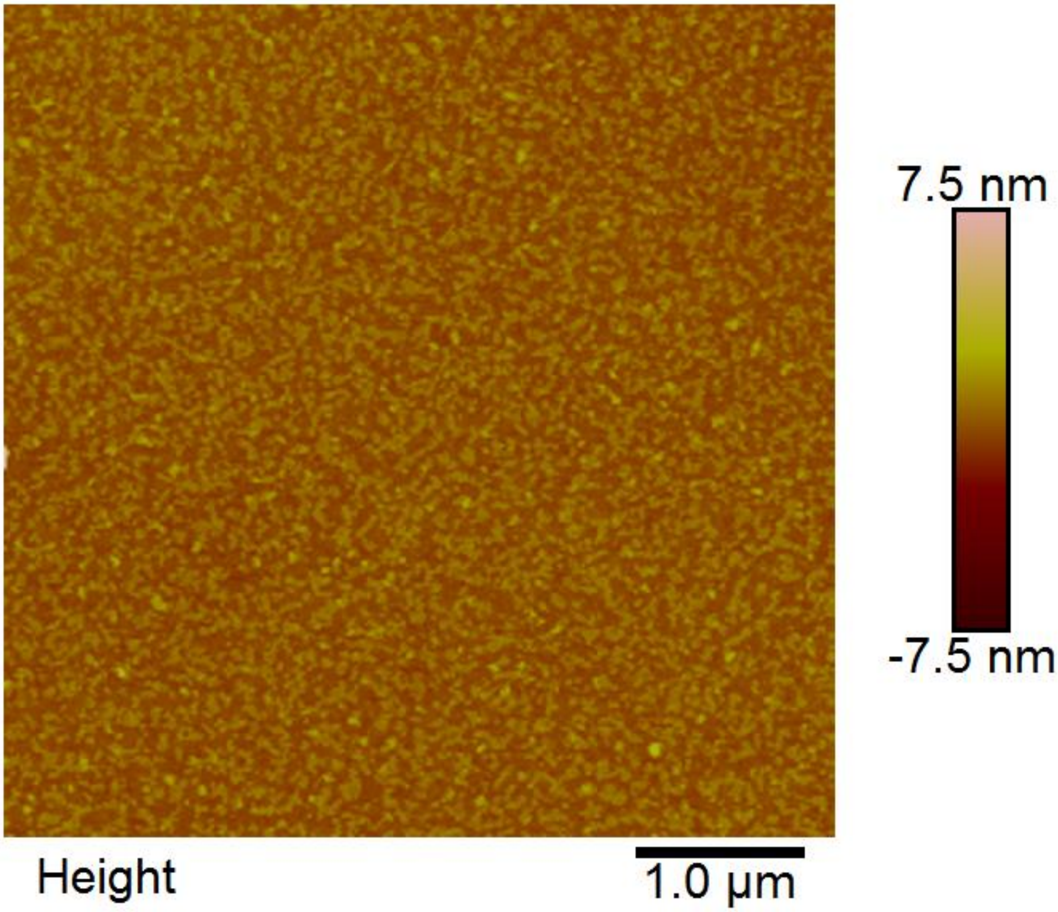

Figure 51. Atomic force microscopy 5 x 5 μm^2 area image of a ~60 nm thick nickel metal film grown on a platinum substrate at 180 °C using Ni(^{tBu2}DAD)$_2$ and *tert*-butyl amine; rms roughness = 1.52 nm.

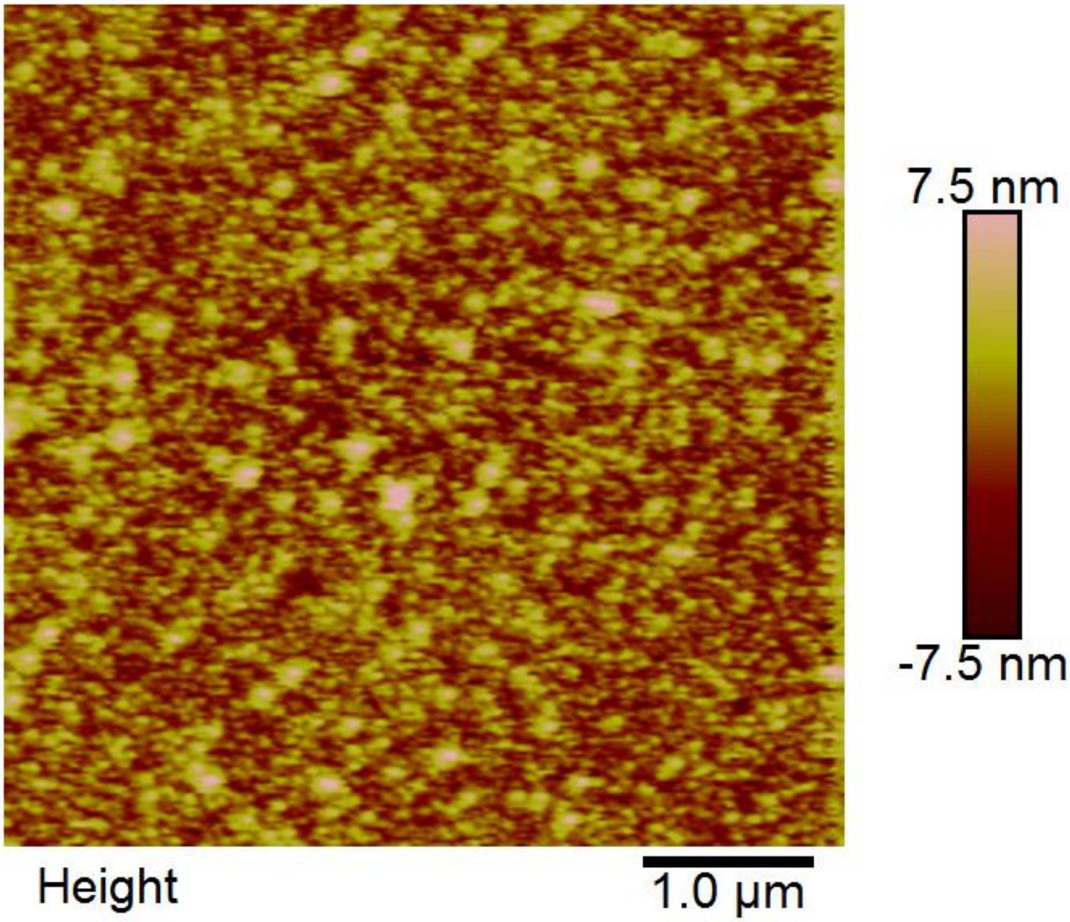

XPS was performed to assess the purity and elemental composition of the as-deposited films of different thicknesses of nickel films (~18 nm and ~60 nm) grown on platinum substrates, at 180 °C. Analysis of the high-resolution multiplex of the Ni 2p core shell reveals binding energies which correspond with metallic nickel (Ni 2p$_{3/2}$ 851.25 eV and Ni 2p$_{1/2}$ 869.99 eV) after as little as 0.5 minutes of sputtering, for both samples (**Figure 52a,b**). These binding energies are consistent with values obtained from a nickel metal standard (Ni 2p$_{3/2}$ 851.25 eV and Ni 2p$_{1/2}$ 869.99 eV) (**Figure 52c**). XPS depth profiling was performed to assess the elemental composition of the films. The ~18 nm thick film was analyzed to assess whether intermixing of the nickel film and platinum substrate occurred. Significant amounts of platinum (> 10%) were observed immediately upon sputtering for 0.5 min (**Figure 53)**. This is suggestive of interfacial alloy formation, which was also seen in the analogous cobalt process described in Chapter 3, and the process using $Co(^{tBu2}DAD)_2$ and formic acid.[34] The ~60 nm thick film was analyzed to assess purity of the deposited films, which revealed > 97% pure nickel metal upon sputtering, with trace impurities (< 1%) of carbon, oxygen, and nitrogen (**Figure 54**).

Figure 52. High-resolution XPS multiplex of nickel 2p region of a) 18 nm and b) 60 nm thick nickel film grown on platinum, at 180 °C, using Ni(^{tBu2}DAD)$_2$ and *tert*-butyl amine; c) reference nickel film.

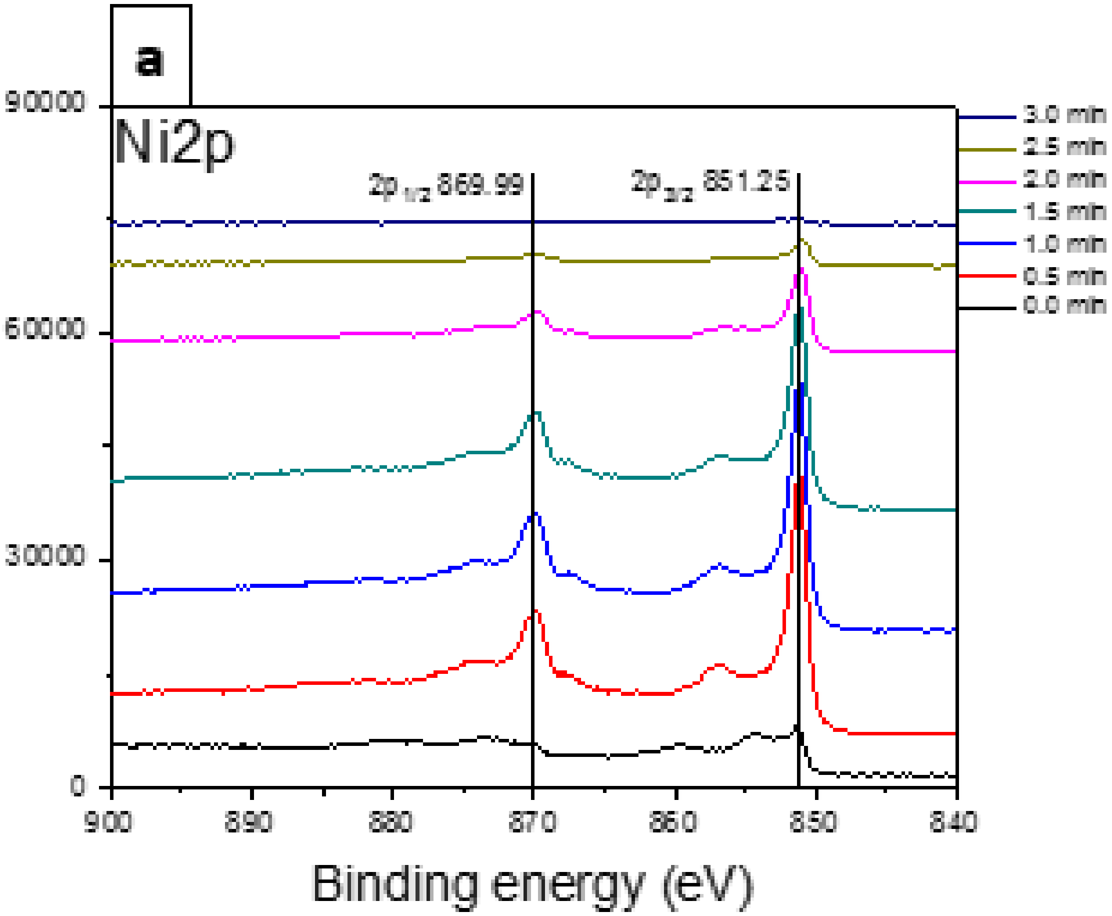

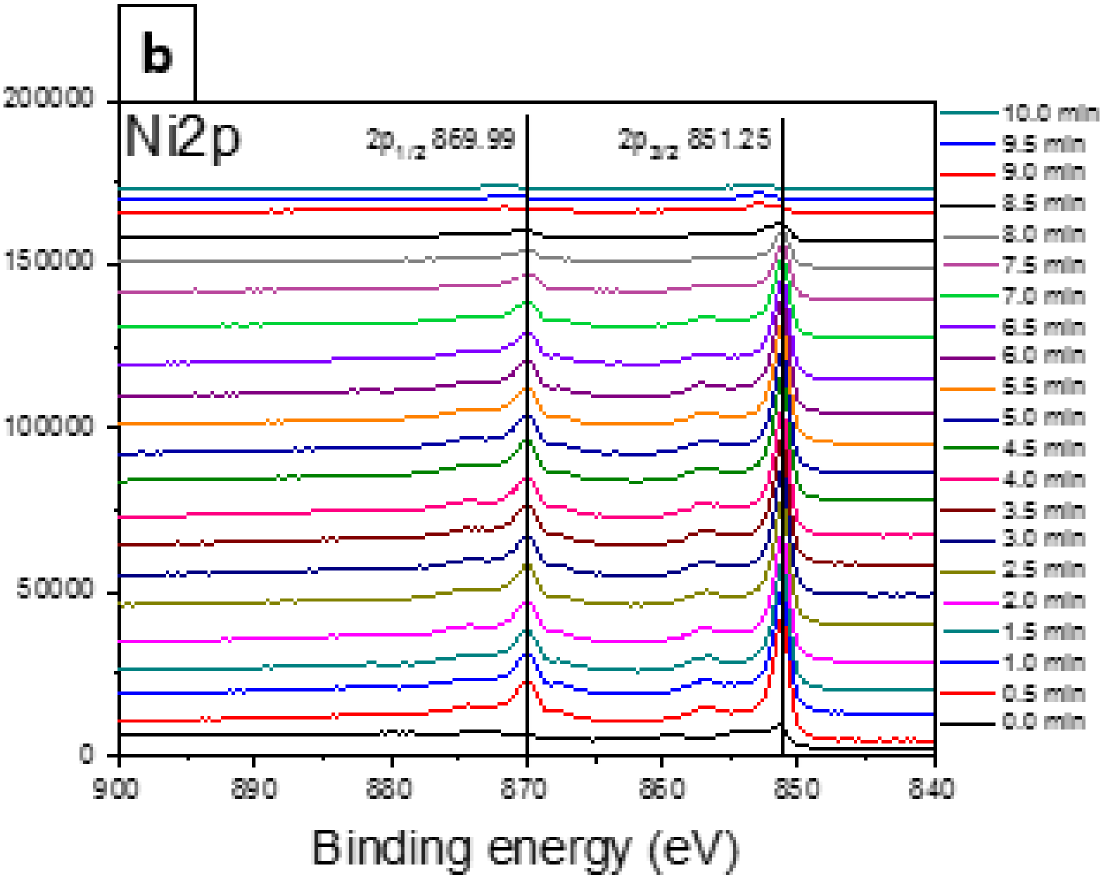
b
Ni2p
$2p_{1/2}$ 869.99
$2p_{3/2}$ 851.25
200000
150000
100000
50000
0
900
890
880
870
860
850
840
Binding energy (eV)
10.0 min
9.5 min
9.0 min
8.5 min
8.0 min
7.5 min
7.0 min
6.5 min
6.0 min
5.5 min
5.0 min
4.5 min
4.0 min
3.5 min
3.0 min
2.5 min
2.0 min
1.5 min
1.0 min
0.5 min
0.0 min

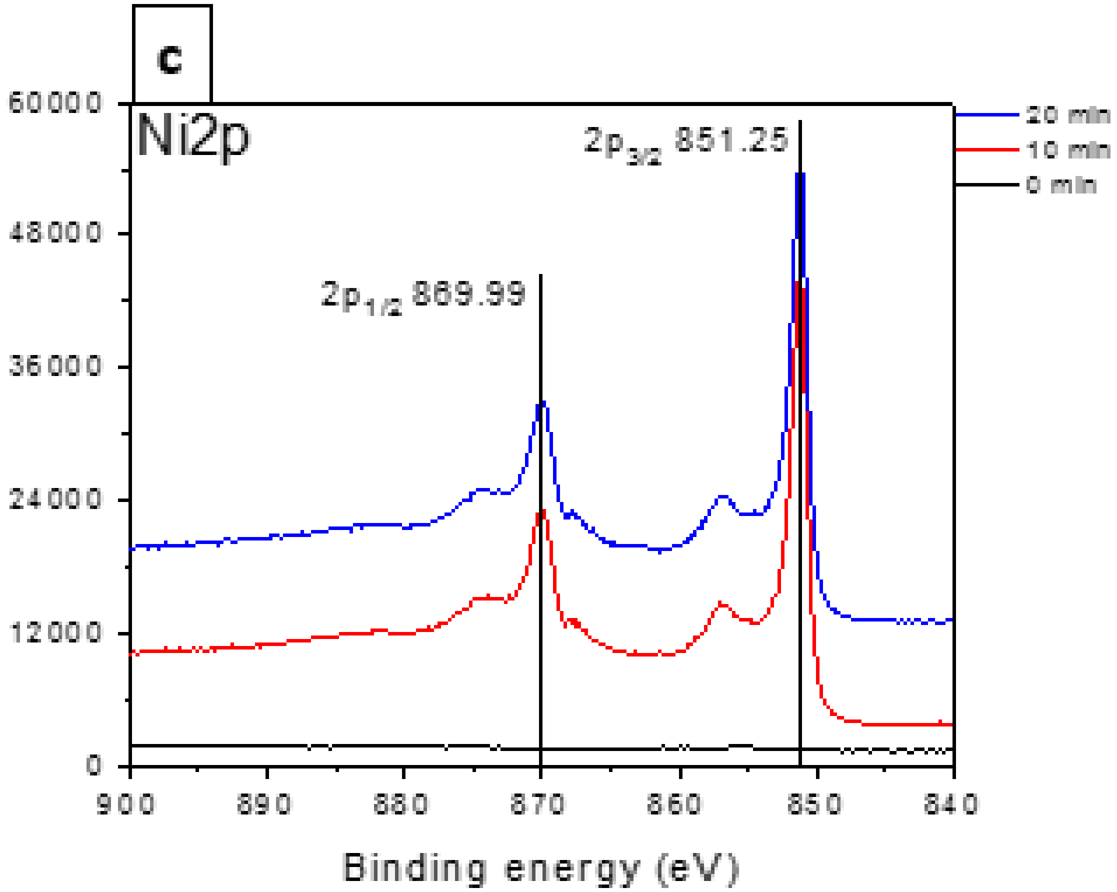
c
Ni2p
$2p_{3/2}$ 851.25
$2p_{1/2}$ 869.99
20 min
10 min
0 min
60000
48000
36000
24000
12000
0
900
890
880
870
860
850
840
Binding energy (eV)

Figure 53. a) XPS depth profile and b) elemental compositions of an 18 nm thick nickel film grown on platinum at 180 °C using Ni(^{tBu2}DAD)$_2$ and *tert*-butyl amine.

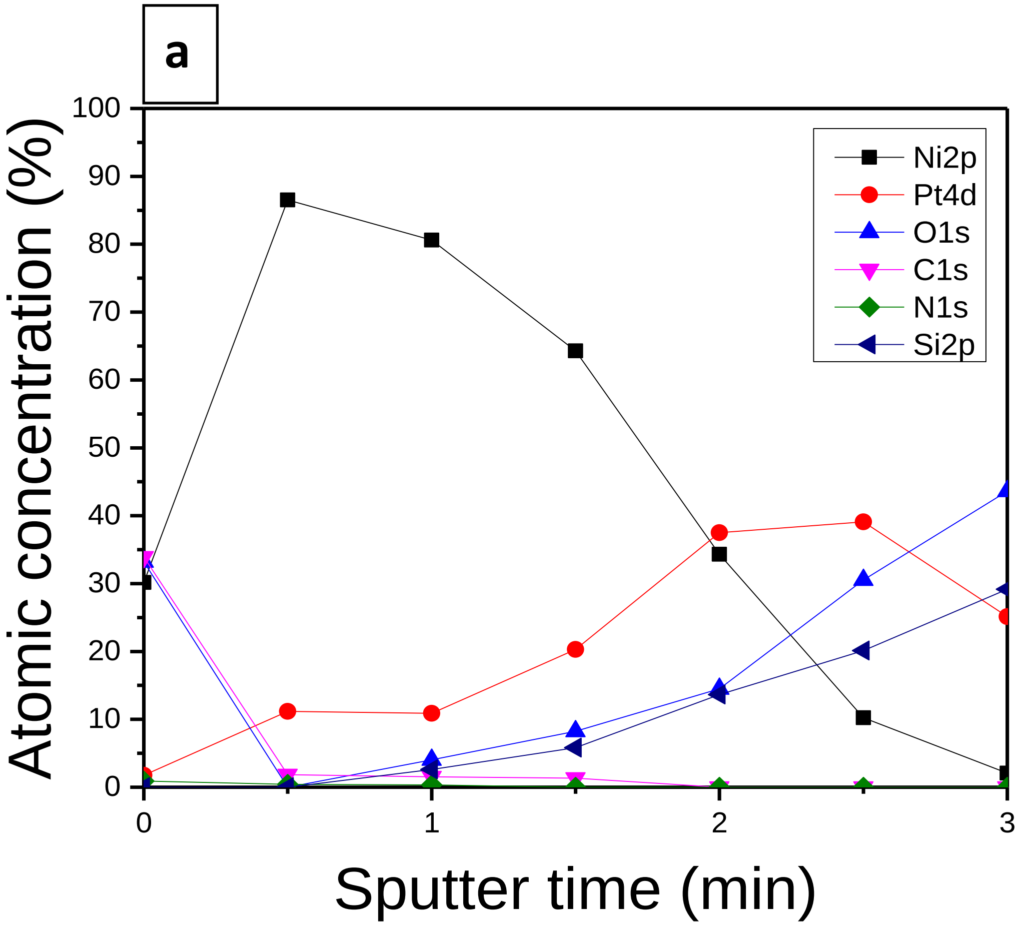

b

Sputter Time (min)	Ni2p	Pt4d	O1s	C1s	N1s	Si2p
0.0	30.2	1.8	33.2	33.9	0.9	0.0
0.5	86.5	11.2	0.0	1.9	0.4	0.0
1.0	80.6	10.9	4.0	1.5	0.3	2.6
1.5	64.3	20.3	8.2	1.3	0.0	5.8
2.0	34.3	37.5	14.5	0.0	0.0	13.7
2.5	10.2	39.1	30.5	0.0	0.0	20.1
3.0	2.1	25.1	43.6	0.0	0.0	29.2

Figure 54. XPS depth profile of a 60 nm thick nickel film grown on platinum at 180 °C using Ni(^{tBu2}DAD)$_2$ and *tert*-butyl amine.

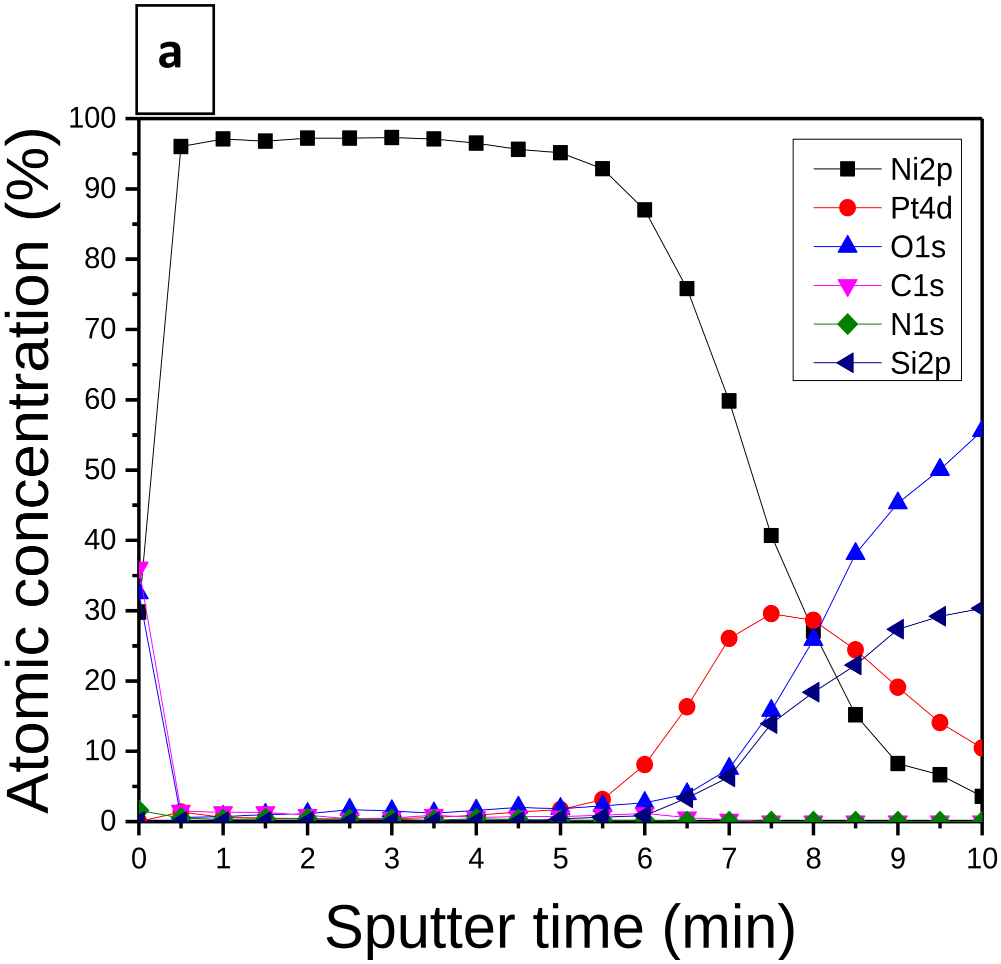

b

Sputter Time (min)	Ni2p	Pt4d	O1s	C1s	N1s	Si2p
0.0	29.8	0.0	32.5	36.1	1.6	0.0
0.5	96.0	1.4	0.6	1.5	0.5	0.0
1.0	97.1	0.6	0.7	1.3	0.3	0.0
1.5	96.8	0.5	1.0	1.3	0.4	0.0
2.0	97.2	0.4	1.1	0.9	0.4	0.0
2.5	97.2	0.4	1.7	0.4	0.3	0.0
3.0	97.3	0.4	1.5	0.5	0.3	0.0
3.5	97.1	0.6	1.2	0.9	0.2	0.0
4.0	96.5	0.9	1.6	0.6	0.4	0.0
4.5	95.6	1.4	2.0	0.7	0.3	0.0
5.0	95.1	1.7	1.8	0.7	0.2	0.4
5.5	92.9	3.1	2.3	0.9	0.2	0.6
6.0	87.0	8.1	2.7	1.2	0.2	0.9
6.5	75.8	16.3	3.9	0.6	0.0	3.4
7.0	59.8	26.0	7.5	0.3	0.0	6.3
7.5	40.7	29.6	15.8	0.0	0.0	13.9
8.0	27.1	28.6	25.9	0.0	0.0	18.4
8.5	15.2	24.4	38.1	0.0	0.0	22.3
9.0	8.2	19.1	45.3	0.0	0.0	27.4
9.5	6.7	14.1	50.1	0.0	0.0	29.2
10.0	3.6	10.5	55.6	0.0	0.0	30.4

4.2.3 Description of Growth of Nickel Metal on Metallic Substrates

The early stages of growth of metallic nickel were demonstrated on a variety of metallic substrates (platinum, copper, and ruthenium) using Ni(^{tBu2}DAD)$_2$ and *tert*-butyl amine as precursors. These experiments used a previously established saturative pulsing sequence of Ni(^{tBu2}DAD)$_2$ (5.0 s), purge (10.0 s), *tert*-butyl amine (0.2 s), purge (10.0 s) for 50 – 1000 cycles. Film growth as a function of number of cycles was analyzed, with thicknesses confirmed by cross-sectional SEM, on platinum, copper, and ruthenium (**Figure 55**). Linear growth was observed on platinum substrates ≥ 50 cycles (~ 3.0 nm), showing no nucleation delay for this process on these substrates. Although linear growth was observed on platinum substrates, the growth on ruthenium and copper was not linear in relation to the number of cycles. Growth of metallic nickel films on ruthenium substrates shows a delay in growth before 250 cycles (growth rate of 0.12 Å/cycle), and varying growth rates at 500 (0.18 Å/cycle) and 1000 (0.44 Å/cycle) cycles. This delay in normal growth behavior has been observed for the analogous cobalt process (*vide supra*) and is likely due to oxidation of the substrate surface, which is then reduced during the initial cycles, as described in Chapter 2.[34] Further depositions (1500 and 2000 cycles) will be explored to ascertain if ALD growth on ruthenium occurs. Growth of metallic nickel films on copper substrates shows high growth rates at the early stages of growth (1.6 Å/cycle) which tapers down significantly by 1000 cycles (0.59 Å/cycle). The peculiar growth behavior could be due to a catalytic reaction with the copper surface, where precursor interaction with the copper substrate is necessary for the reaction to proceed, with similar growth behavior previously reported for nickel metal grown on ruthenium.[84] Further depositions (1500 and 2000 cycles) will be explored to ascertain if growth completely ceases, as with the prior report.[84] This growth behavior could also be due to oxidation or contaminants found on the copper surface,[34] accordingly, further depositions will be explored by using surface pretreatments to clean the copper substrates before nickel deposition.

Figure 55. Plot of thickness *versus* number of cycles for the growth of nickel metal on ruthenium, copper, and platinum substrates at 180 °C using Ni(^{tBu2}DAD)$_2$ and *tert*-butyl amine.

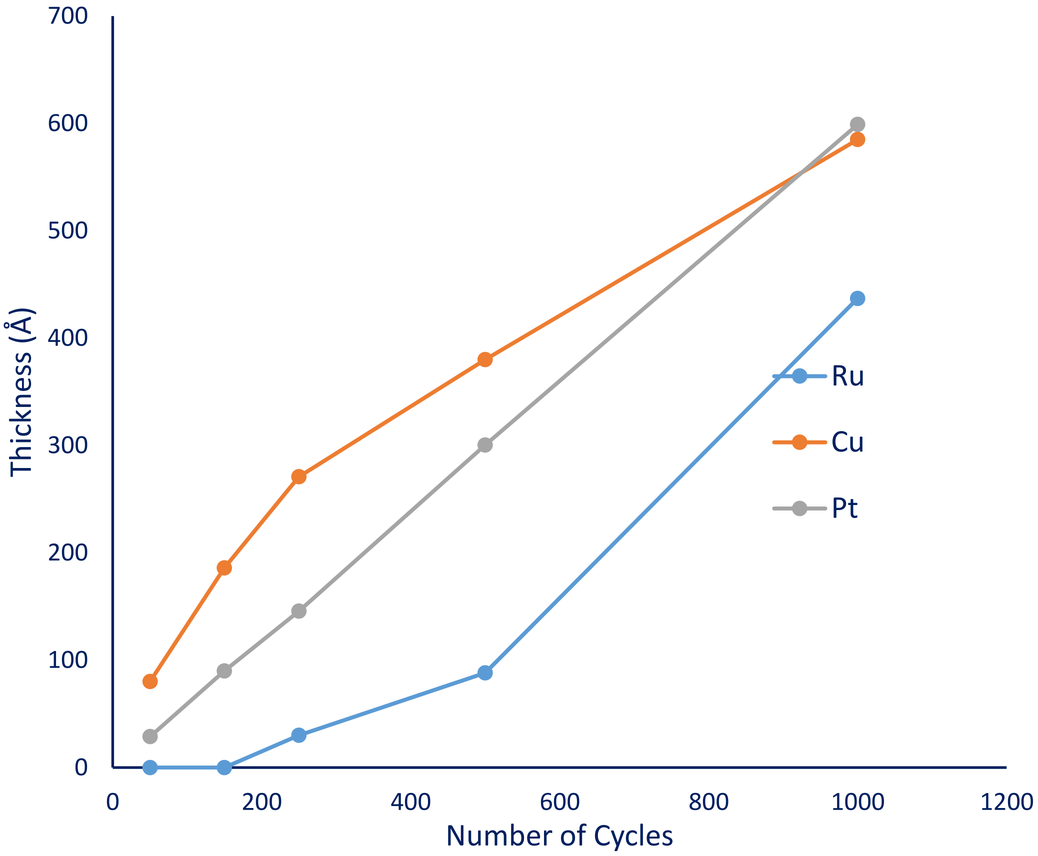

Bulk resistivities were measured for cobalt films deposited on platinum, copper, and ruthenium substrates (**Table 4**). Bulk resistivity was calculated as the product of sheet resistivity and film thickness. The as deposited nickel films grown on platinum have low resistivities, with the resistivity for a 60 nm thick nickel film being 22.1 μΩ cm. For comparison, bulk resistivity of nickel metal at 22 °C is 6.99 μΩ cm.[100] The resistivities of thinner (< 60 nm) nickel films grown on platinum have higher resistivities (~32 – 45 μΩ cm), likely due to the significant intermixing of the nickel and platinum layers as seen by XPS. The resistivities of nickel films grown on ruthenium at the early stages of growth match that of the bare ruthenium substrate, indicating the absence of nickel metal. SEM images also support that no film growth is observed at less than 250 cycles. The delay in growth on ruthenium is likely due to surface oxidation of the ruthenium (*vide supra*). The resistivity of the nickel films on ruthenium after 1000 cycles is 30.6 μΩ cm, which is comparable to the nickel films grown on platinum of similar thickness (31.8 μΩ cm). The comparable resistivities suggest that the nickel films grown after 1000 cycles on ruthenium are similar in quality to the films grown on platinum. The resistivity measured for nickel metal films grown on copper after 1000 cycles is 22.9 μΩ cm, which is within experimental error of nickel films of similar thickness grown on platinum. Low resistivities are observed for nickel films grown on copper from 150 – 500 cycles as well (~27 – 37 μΩ cm). After 50 growth cycles, the resistivity of the ~8 nm thick nickel film grown on copper is that of the copper substrate (1.7 μΩ cm), which is consistent with the conduction occurring through the lower resisitivity copper substrate. It is also possible that intermixing of the nickel and copper layers occur, which will be further investigated with XPS.

Table 4. Resistivities of nickel films grown on metallic substrates using Ni(^{tBu2}DAD)$_2$ and *tert*-butyl amine at 180 °C.

Cycles	Ruthenium[a,b]	Copper[a,c]	Platinum[a,d]
50	53.0	1.7	44.8
150	52.8	36.7	38.6
250	51.1	34.2	36.8
500	49.4	26.7	31.8
1000	30.6	22.9	22.1

[a] Values are in µΩ cm.
[b] The measured resistivity of the uncoated ruthenium substrate is 52.1 µΩ cm.
[c] The measured resistivity of the uncoated copper substrate is 1.7 µΩ cm.
[d] The measured resistivity of the uncoated platinum substrate is 42.6 µΩ cm.

4.2.4 Description of Attempted Growth of Metallic Nickel on Non-Metallic Substrates

The growth of metallic nickel was attempted on a variety of non-metallic substrates (Si(100), SiO$_2$, Si-H, and CDO) using Ni(^{tBu2}DAD)$_2$ and *tert*-butyl amine as precursors. These experiments used a previously established saturative pulsing sequence of Ni(^{tBu2}DAD)$_2$ (5.0 s), purge (10.0 s), *tert*-butyl amine (0.2 s), purge (10.0 s) for 50 – 1000 cycles. The absence of cobalt metal films on these substrates up to 1000 cycles was confirmed by cross-sectional SEM and EDS (**Figure 56**).

Figure 56. a) Cross-sectional SEM of a CDO substrate after 1000 deposition cycles at 180 °C b) EDS of a CDO substrate after 1000 deposition cycles at 180 °C.

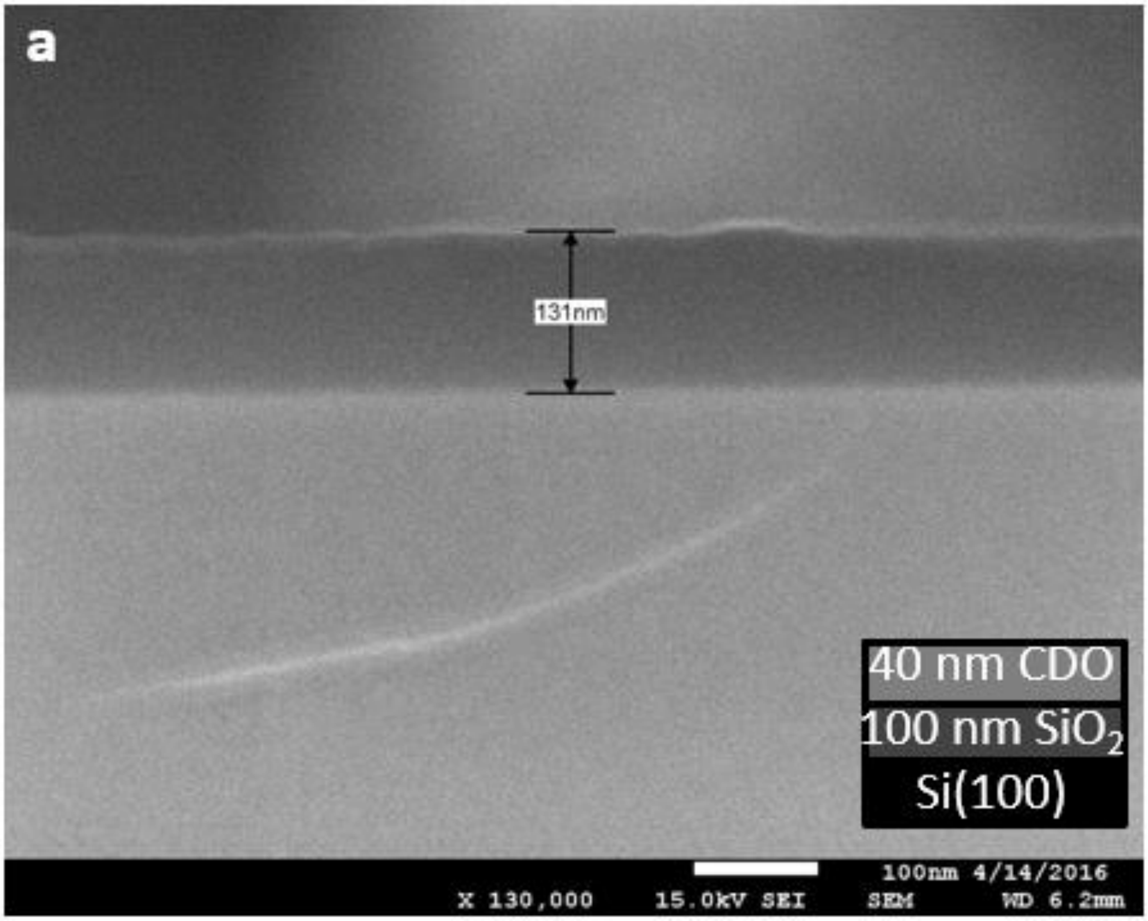

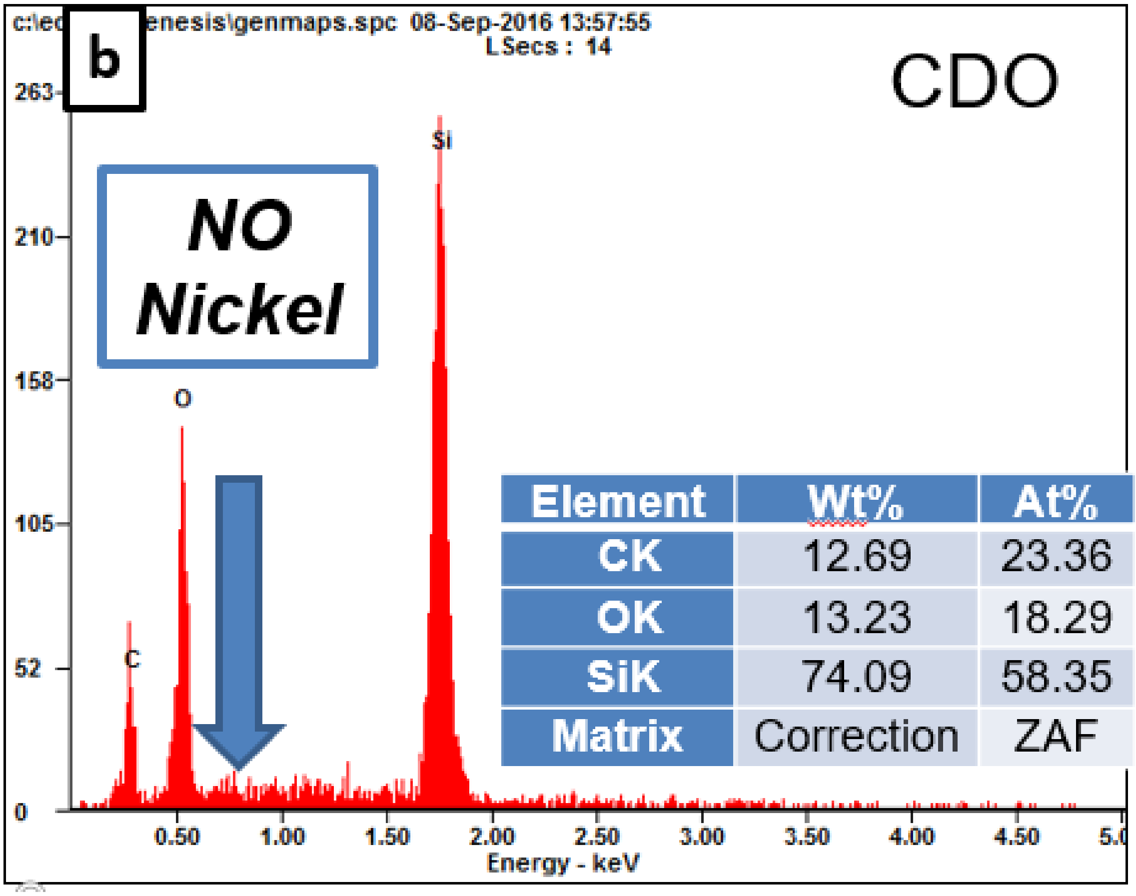

Element	Wt%	At%
CK	12.69	23.36
OK	13.23	18.29
SiK	74.09	58.35
Matrix	Correction	ZAF

The temperature dependence of the substrate-selective deposition of this process, the selectivity window, was explored. A series of 250-cycle depositions were carried out with saturative precursor doses, Ni(^{tBu2}DAD)$_2$ (5.0 s), purge (10.0 s), *tert*-butyl amine (0.2 s), purge (10.0 s), at varying temperatures. Since applications for selective depositions will require ≤ 20 nm of nickel metal, and the observed growth rate for this process is 0.60 Å/cycle, a 250 cycle limit was imposed to provide relevant insight. The depositions were carried out from 160 – 220 °C (**Figure 57**). None of the attempted deposition temperatures resulted in the deposition of nickel on any of the non-metallic substrates, and the absence of nickel metal films on these substrates was confirmed by cross-sectional SEM and EDS.

Figure 57. Area-selective ALD temperature window, where no growth was observed on Si(100), Si-H, and CDO substrates after 250 cycles.

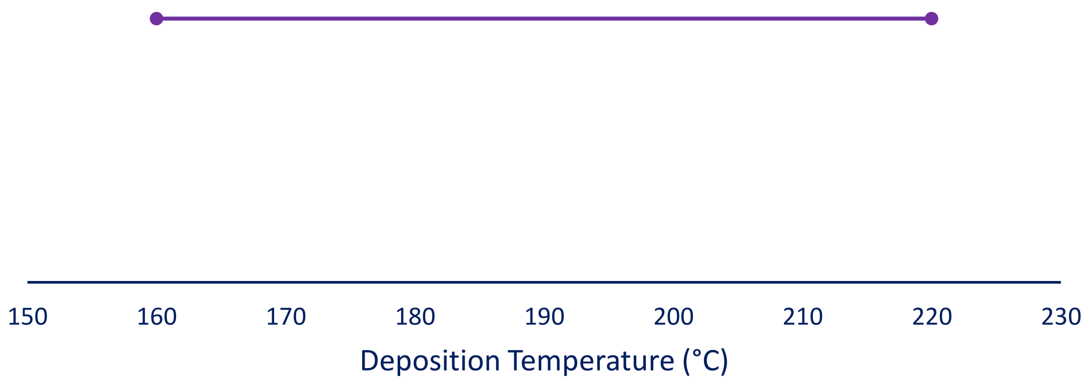

4.2.5 Trial Depositions for Nickel Metal using Ni(^{tBu2}DAD)$_2$ and Other Alkyl amines

The growth of metallic nickel was explored using diethyl amine and triethyl amine as a precursor alternative to *tert*-butyl amine. Films were grown using the pulsing sequence of Ni(^{tBu2}DAD)$_2$ (5.0 s), purge (10.0 s), diethyl amine (0.2 s)/ triethyl amine (0.2 s), purge (10.0 s) at a deposition temperature of 250°C, for 180 cycles. Nickel metal depositions on platinum substrates using diethyl amine and triethyl amine as a precursor resulted in no observable films (as confirmed by cross-sectional SEM). No further investigation was pursued.

4.3 Conclusions

The growth of nickel metal by low temperature thermal ALD from Ni(^{tBu2}DAD)$_2$ and *tert*-butyl amine at 180 °C on various substrates was demonstrated. On platinum substrates, a linear growth rate of 0.60 Å/cycle from 50 – 1000 cycles was observed for plots of thickness as a function of the number of cycles. The y-intercept for this graph is within experimental error of zero, indicating no nucleation delay, with normal growth observed for as little as 3 nm of nickel on platinum substrates. Growth on ruthenium substrates showed a delay of 250 cycles before growth was observed, and is likely due to surface oxidation of the ruthenium substrate. Linear ALD growth of nickel metal on ruthenium and copper was not demonstrated, further depositions will be performed to determine if linear ALD growth occurs for this process on these substrates. Films of ~18 nm and ~60 nm thick nickel metal on platinum substrates were analyzed by AFM, with rms surface roughnesses of 0.45 nm (2.5% of total thickness), and 1.52 nm (2.5% of total thickness), respectively, which show that these films are smooth and continuous over a wide range of thicknesses. XPS analyses reveal that this process deposits high-purity nickel metal (> 97%). Films grown on platinum and copper substrates showed low resistivities of ~22 μΩ cm after 1000 cycles (~60 nm thick films). No film growth was observed after 1000 cycles on Si(100), Si-H, thermal SiO_2 and CDO substrates. Selective deposition of nickel metal on metallic substrates over non-metallic substrates occurs over a selectivity window of 160 – 220 °C.

4.4 Experimental Section

A Picosun R-75BE ALD reactor was used for the thin film deposition experiments. Ultra-high purity nitrogen (99.999%, purchased from Airgas) was used as the carrier and purge gas for all depositions. The ALD reactor had a constant flow of the same ultra-high purity nitrogen in the deposition chamber for all depositions, with a pressure of 6 – 9 Torr.

The low-temperature ALD of metallic nickel thin films was performed using Ni($^{\text{tBu2}}$DAD)$_2$ and *tert*-butyl amine as precursors. Ni($^{\text{tBu2}}$DAD)$_2$ was according to a literature procedure.[92] All alkyl amines used in depositions (*tert*-butyl amine, diethyl amine, and triethyl amine) were purchased from Sigma Aldrich. In initial growth trials, the source temperature for Ni($^{\text{tBu2}}$DAD)$_2$ was found to be optimum at 140 °C under the reactor pressure, and Ni($^{\text{tBu2}}$DAD)$_2$ was delivered by a Picosun solid state booster, while *tert*-butyl amine was delivered by a vapor-draw ampule at 20 °C. Substrate temperatures were varied between 160 and 220 °C. Film growth experiments used to assess selectivity were performed using the pulse sequence Ni($^{\text{tBu2}}$DAD)$_2$ (4.0 s)/N$_2$ purge (10.0 s)/*tert*-butyl amine (0.2 s)/N$_2$ purge (10.0 s) at 200 °C. For the selectivity temperature window experiments, the same pulse and purge sequence was used, but the deposition temperatures were varied from 160 – 220 °C. ALD growth studies were performed on Ru (13 nm)/TaN (2 nm)/SiO$_2$ (100 nm)/Si(100), Cu (33 nm)/TaN (7 nm)/SiO$_2$ (100 nm)/Si(100), Pt (10 nm)/SiO$_2$ (100 nm)/Si(100), Si(100) with native oxide, Si-H, thermal SiO$_2$ (100 nm)/Si(100), and CDO (~40 nm)/SiO$_2$ (100 nm)/Si(100) substrates. Si-H substrates were prepared by treating Si(100) with native oxide substrates with a 2% aqueous HF solution, followed by rinsing with deionized water and then drying with a stream of clean, dry air. The other substrates were used as received, except that they were rinsed sequentially with isopropanol and deionized water and then were dried with a stream of clean, dry air. One substrate of each kind, a 2 x 2 cm^2 coupon, was used in each experiment.

Film thicknesses were determined using cross-sectional SEM collected on a JEOL-6510LV electron microscope. The growth rates were determined by dividing the measured film thicknesses by the number of deposition cycles. Film thicknesses were measured at a minimum of three positions on each film to evaluate the uniformity. EDS was carried out on the JEOL-6510LV electron microscope using an Ametek EDAX system with Genesis Spectrum software. The accelerating voltage for the EDS measurements was 6 kV. AFM measurements were conducted using a Bruker BioScope Catalyst AFM using contact mode. XPS measurements were conducted using an Al Kα (1486.6 eV) X-ray source at a chamber base pressure of 10^{-10} Torr. Spectra were recorded using a 16-channel detector with a hemispherical analyzer. Sputtering was performed using argon ions supplied by an argon sputter gun positioned at a 45° angle with respect to the substrate normal. Each sample was sputtered over a 2 x 2 mm^2 area and measured over a 0.8 x 0.8 mm^2 area. Nickel metal standards were sputtered with 5 keV argon ions. An uncoated platinum substrate (Pt (10 nm)/SiO_2 (100 nm)/Si(100)) was used as a standard for platinum and was sputtered with 3 keV argon ions. The ALD-grown cobalt films on platinum were sputtered with 3 keV argon ions. Sheet resistivity measurements were obtained using a Jandel 4-point probe in combination with a Keithley 2400 SourceMeter and a Keithley 2182A Nanovoltmeter. All films grown on metal substrates passed the Scotch tape test.

CHAPTER 5 CONCLUSIONS

This work shows that substrate-selective deposition has been demonstrated for Co(^{tBu2}DAD)$_2$ and formic acid. Cobalt metal is inherently deposited on metallic substrates, with no metal film deposition observed on non-metallic substrates. Cross-sectional SEM has been employed to study the film thicknesses. EDS was carried out to confirm the absence of cobalt on the non-metallic substrates, which was also supported by XPS. Elemental composition of the deposited films has been carried out using XPS, revealing significant intermixing of the cobalt film layer and the metallic substrate layer (platinum, copper). Four-point probe measurements were carried out to determine the sheet resistivity of the films, giving insight into the continuity and composition of the metallic films. Data obtained from XPS studies, coupled with sheet resistivities of the films, supports the hypothesis that the facile ALD growth of cobalt on platinum and copper substrates is likely due to the formation of an interfacial alloy layer.

The deposition of high-purity metallic cobalt thin films grown by ALD, using non-corrosive, inexpensive, alkyl amine reducing co-reagents has been demonstrated. The low-temperature thermal ALD process used Co(^{tBu2}DAD)$_2$ and *tert*-butyl amine to afford high-purity, low-resistivity (13 – 19 μΩ cm) cobalt metal thin films in the ALD window between 170 – 200 °C. Self-limiting growth was observed, along with a linear growth rate of 0.98 Å/cycle for cobalt films deposited on platinum and copper substrates for as little as 25 cycles, allowing for precise control of thin film growth. Characterization of cobalt metal films grown on various substrates was performed. Cross-sectional SEM has been employed to study the film thickness. Elemental composition of the deposited films using XPS revealed high-purity cobalt metal (> 98%), with low contamination from carbon, nitrogen and oxygen (< 1% each). Four-point probe measurements were carried out to determine the resistivity of the films, giving insight into the continuity on composition of the metallic films. These resistivity values are similar to the values measured in the study presented in Chapter 2, for films of comparable thicknesses. Data obtained from XPS studies, coupled with sheet resistivities of the films, supports the hypothesis that the facile ALD growth of cobalt on platinum and copper substrates is likely due to the formation of an interfacial alloy layer. Substrate-selective deposition has been demonstrated for $Co(^{tBu2}DAD)_2$ and *tert*-butyl amine. Cobalt metal is inhertently deposited on metallic substrates, with no metal film deposition on non-metallic substrates. Selectivity was assessed by cross-sectional SEM, and EDS was carried out to assess cobalt deposition on the non-metallic substrates. Elemental composition of the deposited films has been carried out using XPS, revealing significant intermixing of the cobalt film layer and the metallic substrate layer (platinum).

The low-temperature thermal ALD process for $M(^{tBu2}DAD)_2$ and alkyl amines was explored for the use of the deposition of metallic nickel thin films. $Ni(^{tBu2}DAD)_2$ and *tert*-butyl amine afforded films of high-purity, low-resistivity (22 $\mu\Omega$ cm) nickel metal films in the ALD window between 180 – 195 °C. Self-limiting growth was observed, along with a linear growth rate of 0.60 Å/cycle for nickel films deposited on platinum substrates for as little as 50 cycles; allowing for precise control of thin film growth. Full characterization of nickel metal films grown on platinum substrates was performed. Cross-sectional SEM was employed to study the film thicknesses. Elemental composition of the deposited films using XPS showed high-purity nickel metal (> 97%), with low contamination of carbon, nitrogen and oxygen (< 1.5% each) for the ~60 nm thick film. XPS analysis of the ~18 nm thick film revealed significant intermixing of the nickel film layer and the metallic substrate layer (platinum). Four-point probe measurements were performed to determine the resistivity of the films, giving insight into the continuity and composition of the metallic films. The low-resistivity value (22 μΩ cm) suggests that these films are continuous, high-purity, metallic nickel films. XPS, together with resistivity data, suggest the facile growth of nickel on platinum substrates proceeding *via* interfacial alloy formation. Substrate-selective deposition was demonstrated for $Ni(^{tBu2}DAD)_2$ and *tert*-butyl amine. Nickel metal is inherently deposited on metallic substrates, with no metal film deposition present on non-metallic substrates. Selectivity was assessed by cross-sectional SEM, along with EDS, which qualitatively supported the absence of cobalt on the non-metallic substrates. Although linear growth was observed on platinum substrates, it was not observed for copper or ruthenium substrates. More experiments are necessary to understand fully what is occurring to cause the unusual growth behavior on copper and ruthenium substrates.

The low-temperature thermal ALD process using $M(^{tBu2}DAD)_2$ and alkyl amines to afford metal films was successfully extended from a cobalt metal process to a nickel metal process. These results are suggestive that ALD processes employing $M(^{tBu2}DAD)_2$ and alkyl amines may be general to give the corresponding metals. Future directions for this research could lead to new avenues to deposit other desirable and challenging to reduce metals by thermal ALD, such as iron, manganese, and chromium.

A future application for this work is the potential to deposit magnetic materials, such as iron/cobalt or iron/nickel layered-films, by thermal ALD. Deposition of magnetic materials by ALD could enable magnetic based storage devices (such as MRAM, which requires multilayered magnetic materials) to be developed with atomic layer precision of thicknesses. This can be achieved by depositing alternating desired metal layers using $M(^{tBu2}DAD)_2$ and alkyl amines.

APPENDIX

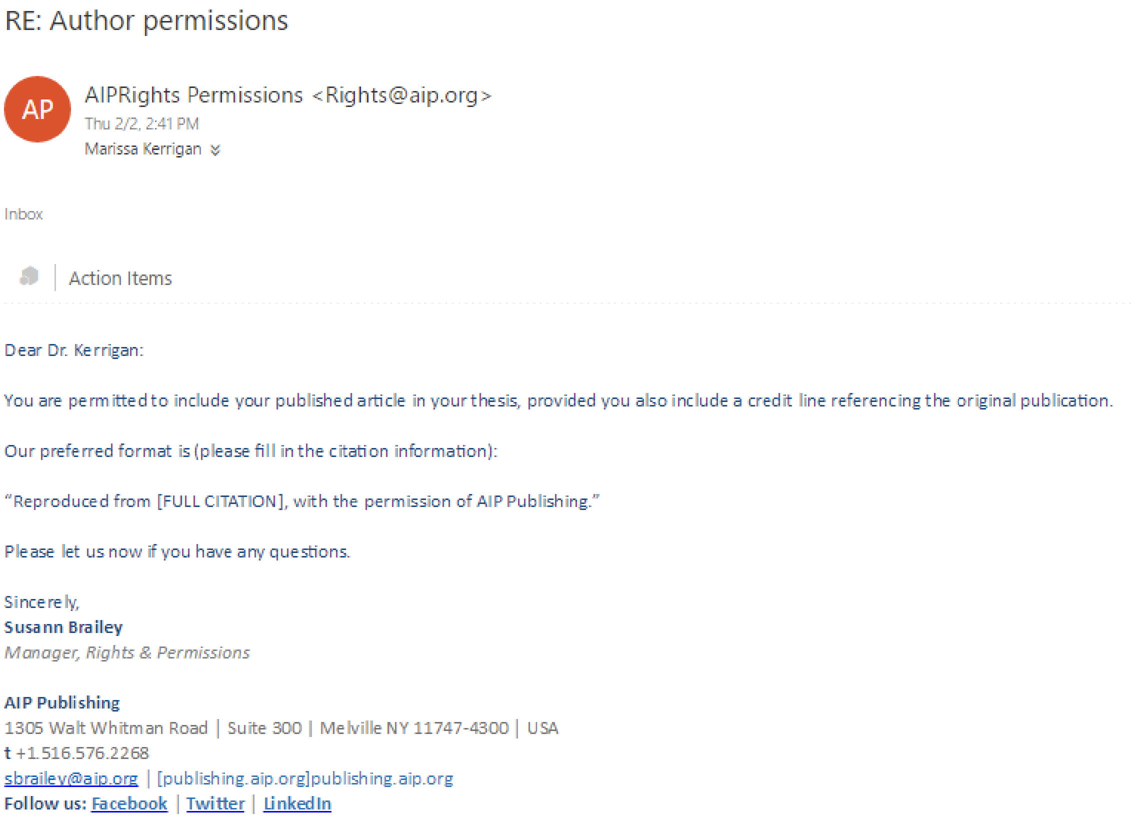

RE: Author permissions

AIPRights Permissions <Rights@aip.org>
Thu 2/2, 2:41 PM
Marissa Kerrigan

Dear Dr. Kerrigan:

You are permitted to include your published article in your thesis, provided you also include a credit line referencing the original publication.

Our preferred format is (please fill in the citation information):

“Reproduced from [FULL CITATION], with the permission of AIP Publishing.”

Please let us now if you have any questions.

Sincerely,
Susann Brailey
Manager, Rights & Permissions

AIP Publishing
1305 Walt Whitman Road | Suite 300 | Melville NY 11747-4300 | USA
t +1.516.576.2268
sbrailey@aip.org | [publishing.aip.org]publishing.aip.org
Follow us: Facebook | Twitter | LinkedIn

REFERENCES

1. Leskelä, M.; Ritala, M. *Angew. Chem. Int. Ed.* **2003,** *42*, 5548-5554.
2. George, S. M. *Chem. Rev.* **2010,** *110*, 111-131.
3. Knisley, T. J.; Kalutarage, L. C.; Winter, C. H. *Coord. Chem. Rev.* **2013,** *257*, 3222-3231.
4. *Digital Integrated Circuits A Design Perspective;* Rabaey, J. M. C., A.; Nikolic, B.; Second ed.; Pearson Education, Inc.: Upper Saddle River, NJ 07458, 2003.
5. *Semiconductor Device Fundamentals*; Pierret, R. F.; Addison Wesley Longman: Reading, Massachussetts, 1996; p 1-781.
6. Moore, G. E. *Electronics* **1965,** *38*, 33-35.
7. Tullo, A. H.; McCoy, M.; Tremblay, J.-F. *C&E News* **2015,** *93*, 31.
8. *International Roadmap for Semiconductors*; 2017. www.itrs2.net/.
9. Wong, H.; Zhang, J.; Feng, X.; Yu, D.; Iwai, H. *IEEE T. Electron. Dev.* **2016**, *49*, 36-39.
10. *Al/HfO*$_2$*/Si Gate Stack with Improved Physical and Electrical Parameters;* Prasher, R.; Dass, D.; Vaid, R. Taylor & Francis: 2016, pp 334-337.
11. Gritsenko, V. A.; Perevalov, T. V.; Islamov, D. R. *Phys. Rep.* **2016**, *613*, 1-20.
12. Wilk, G. D.; Wallace, R. M.; Anthony, J. M. *J. Appl. Phys.* **2001**, *89*, 5243-5275.
13. Roule, A. A.; Amuntencei, M.; Deronzier, E.; Haumesser, P. H.; Da Silva, S.; Avale, X.; Pollet, O.; Baskaran, R.; Passemard, G. *Microelectron. Eng.* **2007**, *84*, 2610-2614.

14. Huang, C.-L.; Lai, C.-H.; Tsai, P.-H.; Kuo, Y.-L.; Lin, J.-C. *Elec. Mater. Let.* **2014,** *10*, 551-556.

15. Rossnagel, S. M. *J. Vac. Sci. Technol. A* **2003**, *21*, S74-S87.

16. Norman, J. A. T.; Muratore, B. A.; Dyer, P. N.; Roberts, D. A.; Hochberg, A. K.; Dubois, L. H. *Mater. Sci. Eng. B* **1993**, *17*, 87-92.

17. Bryant, W. A. *J. Mater Sci.* **1977**, *12*, 1285-1306.

18. Holstein, W. L. *Prog. Cryst. Growth Charact. Mater.* **1992**, *24*, 111-211.

19. Parsons, G. N.; George, S. M.; Knez, M. *MRS Bull.* **2011**, *36*, 865-871.

20. Rossnagel, S. M.; Sherman, A.; Turner, F. *J. Vac. Sci. Technol. B* **2000**, *18*, 2016-2020.

21. Kim, H.; Rossnagel, S. M. *J. Vac. Sci. Technol. A* **2002**, *20*, 802-808.

22. Profijt, H. B.; Potts, S. E.; van de Sanden, M. C. M.; Kessels, W. M. M. *J. Vac. Sci. Technol. A* **2011**, *29*, 050801.

23. Mackus, A. J. M.; Bol, A. A.; Kessels, W. M. M. *Nanoscale* **2014**, *6*, 10941-10960.

24. Kim, W.-H.; Hashemi, M.; Sadat, F.; Mackus, A. J. M.; Singh, J.; Kim, Y.; Bobb-Semple, D.; Fan, Y.; Kaufman-Osborn, T.; Godet, L.; Bent, S. F. *ACS Nano* **2016**, *10*, 4451-4458.

25. Kalanyan, B.; Lemaire, P. C.; Atanasov, S. E.; Ritz, M. J.; Parsons, G. N. *Chem. Mater.* **2016**, *28*, 117-126.

26. Lee, H.-B.-R.; Kim, H. *ECS Trans.* **2008**, *16*, 219-225.

27. Lee, H.; Kim, J.; Kim, H.; Kim, W.; Lee, J.; Hwang, I. *J. Korean Phys. Soc.* **2010**, *56*, 104-107.

28. Lee, H.-B.-R.; Kim, W.-H.; Lee, J. W.; Kim, J.-M.; Heo, K.; Hwang, I. C.; Park, Y.; Hong, S.; Kim, H. *J. Electrochem. Soc.* **2010**, *157*, D10-D15.

29. Hashemi, M.; Sadat, F.; Prasittichai, C.; Bent, S. F. *ACS Nano* **2015**, *9*, 8710-8717.

30. Färm, E.; Kemell, M.; Ritala, M.; Leskelä, M. *Chem. Vap. Dep.* **2006**, *12*, 415-417.

31. Park, K. J.; Doub, J. M.; Gougousi, T.; Parsons, G. N. *Appl. Phys. Lett.* **2005**, *86*, 051903.

32. Jiang, X.; Wang, H.; Qi, J.; Willis, B. G. *J. Vac. Sci. Technol. A* **2014**, *32*, 041513.

33. Willis, B. G.; Qi, J.; Jiang, X.; Chen, J.; Weisel, G. J.; Zimmerman, D. T. *ECS Trans.* **2014**, *64*, 253-263.

34. Kerrigan, M. M.; Klesko, J. P.; Rupich, S. M.; Dezelah, C. L.; Kanjolia, R. K.; Chabal, Y. J.; Winter, C. H. *J. Chem. Phys.* **2017**, *146*, 052813.

35. Lutsev, L. V.; Stognij, A. I.; Novitskii, N. N. *Phys. Rev. B* **2009**, *80*, 184423.

36. Chi, V.-V.; Zoukaa, K.-B.; Hongxin, Y.; Johann, C.; Jan, V.; Stefania, P.; Pascale, B.-G.; Mairbek, C.; Laurent, R.; Valérie, G.; Philippe, D.; Violaine, S.; Olivier, F. *New J. Phys.* **2010**, *12*, 103040.

37. Zhu, S.; Van Meirhaeghe, R. L.; Detavernier, C.; Cardon, F.; Ru, G.-P.; Qu, X.-P.; Li, B.-Z. *Solid-State Electron.* **2000**, *44*, 663-671.

38. He, M.; Zhang, X.; Nogami, T.; Lin, X.; Kelly, J.; Kim, H.; Spooner, T.; Edelstein, D.; Zhao, L. *J. Electrochem. Soc.* **2013**, *160*, D3040-D3044.

39. Yang, C. C.; Flaitz, P.; Wang, P. C.; Chen, F.; Edelstein, D. *IEEE Electron Dev. Let.* **2010**, *31*, 728-730.

40. Yutaka, K.; Shuji, K.; Youhei, E.; Junichi, H.; Masamichi, H.; Shouichirou, K.; Yuta, S.; Yasushi, H. *Jap. J. Appl. Phys.* **2013**, *52*, 05FA01.

41. Wislicenus, M.; Liske, R.; Gerlich, L.; Vasilev, B.; Preusse, A. *Microelectron. Eng.* **2015**, *137*, 11-15.

42. Simon, A. H.; Bolom, T.; Niu, C.; Baumann, F. H.; Hu, C. K.; Parks, C.; Nag, J.; Kim, H.; Lee, J. Y.; Yang, C. C.; Nguyen, S.; Shobha, H. K.; Nogami, T.; Guggilla, S.; Ren, J.; Sabens, D.; AuBuchon, J. F. *IEEE Int. Reliability Physics Symposium (IRPS)*, 14-18 April 2013; pp 3F.4.1-3F.4.6.

43. Chen, S.-T.; Liu, Y.-Y.; Chen, G.-S. *Appl. Surf. Sci.* **2015**, *354*, 144-147.

44. McLellan, P. **2016**, https://community.cadence.com/cadence_blogs_8/b/breakfast-bytes/archive/2016/06/24/an-steegen-16

45. Lapedus, M. **2016**, http://semiengineering.com/interconnect-challenges-grow-2/.

46. Koike, J.; Wada, M. *Appl. Phys. Lett.* **2005**, *87*, 041911.

47. Haneda, M.; Iijima, J.; Koike, J. *Appl. Phys. Lett.* **2007**, *90*, 252107.

48. Usui, T.; Nasu, H.; Takahashi, S.; Shimizu, N.; Nishikawa, T.; Yoshimaru, M.; Shibata, H.; Wada, M.; Koike, J. *IEEE T. Electron Dev.* **2006**, *53*, 2492-2499.

49. Kalutarage, L. C.; Clendenning, S. B.; Winter, C. H. *ECS Trans.* **2014**, *64*, 147-157.

50. Atosuo, E.; Mäntymäki, M.; Mizohata, K.; Heikkilä, M. J.; Räisänen, J.; Ritala, M.; Leskelä, M. *Chem. Mater.* **2017**, *29,* 998-1005.

51. Jaegers, N. R.; Wan, C.; Hu, M. Y.; Vasiliu, M.; Dixon, D. A.; Walter, E.; Wachs, I. E.; Wang, Y.; Hu, J. Z. *J. Phys. Chem. C* **2017**, *121*, 6246–6254.

52. Alfaruqi, M. H.; Mathew, V.; Song, J.; Kim, S.; Islam, S.; Pham, D. T.; Jo, J.; Kim, S.; Baboo, J. P.; Xiu, Z. *Chem. Mater*. **2017**, *29*, 1684–1694

53. Mjejri, I.; Rougier, A.; Gaudon, M. *Inorg. Chem.* **2017**, *56*, 1734-1741.

54. *Handbook of Chemistry and Physics*. 92nd ed.; CRC: Boca Raton, FL, 2012.

55. West, G. A.; Beeson, K. W. *Appl. Phys. Lett.* **1988**, *53,* 740-742.

56. Lane, P. A.; Oliver, P. E.; Wright, P. J.; Reeves, C. L.; Pitt, A. D.; Cockayne, B. *Chem. Vap. Deposition* **1998**, *4,* 183-186.

57. Paranjape, M. A.; Mane, A. U.; Raychaudhuri, A. K.; Shalini, K.; Shivashankar, S. A.; Chakravarty, B. R. *Thin Solid Films* **2002**, *413,* 8-15.

58. Ko, Y. K.; Parl, D.S.; Seo, B.S.; Yang, H.J.; Shin, H.J.; Kim, J.Y.; Lee, J.H.; Lee, W.H.; Reucroft, P.J.; Lee. J.G. *Mater. Chem. Phys.* **2003**, *80,* 560-564.

59. Ye, D.-X. Pimanpang, S.; Jezewski, C.; Tang, F.; Senkevich, J.J.; Wang, G.-C.; Lu, T.-M. *Thin Solid Films* **2005**, *485,* 95-100.

60. Chioncel, M. F.; Haycock, P. W. *Chem. Vap. Deposition* **2005**, *11*, 235-243.

61. Lee, K. P., T.; Lee, J.; Kim, J.; Kim, J.; Kwak, N.; Yeom, S.; Jeon, H. *Jap. J. Appl. Phys.* **2008**, *47*, 5396-5399.

62. Pugh, T.; Cosham, S. D.; Hamilton, J. A.; Kingsley, A. J.; Johnson, A. L. *Inorg. Chem.* **2013**, *52*, 13719-13729.

63. Georgi, C. H., A.; Waechtler, T.; Schulz, S. E.; Gessner, T.; Lang, H. *J. Mater. Chem. C* **2014**, *2*, 4676-4682.

64. Georgi, C. H., M.; Thiel, I.; Hildebrandt, A.; Waechtler, T.; Schulz, S. E.; Lang, H. *Thin Solid Films* **2015**, *578*, 180-184.

65. Yang, J. L., K.; Feng, J.; Gordon, R. G. *J. Mater. Chem. C* **2015**, *3*, 12098-12106.

66. Hamilton, J. A.; Pugh, T.; Johnson, A. L.; Kingsley, A. J.; Richards, S. P., *Inorg. Chem.* **2016**, *55*, 7141-7151.

67. Yang, C. C.; Baumann, F.; Wang, P. C.; Lee, S. Y.; Ma, P.; AuBuchon, J.; Edelstein, D. *Microelectron. Eng.* **2013**, *106*, 214-218.

68. Kim, H. *Microelectron. Eng.* **2013**, *106*, 69-75.

69. Park, J.; Lee, H.-B.-R.; Kim, D.; Yoon, J.; Lansalot, C.; Gatineau, J.; Chevrel, H.; Kim, H. *J. Energy Chem.* **2013**, *22*, 403-407.

70. Lee, H.-B.-R.; Park, Y. J.; Baik, S.; Kim, H. *Chem. Vap. Deposition* **2012**, *18*, 41-45.

71. Jae-Min, K.; Han-Bo-Ram, L.; Clement, L.; Dussart, C.; Julien, G.; Kim, H. *Jap. J. Appl. Phys.* **2010**, *49*, 05FA10.

72. Keunjun, K.; Keunwoo, L.; Sejin, H.; Taeyong, P.; Youngjin, L.; Jeongtae, K.; Seungjin, Y.; Hyeongtag, J. *Jap. J. Appl. Phys.* **2007**, *46*, L173.

73. Kim, K.; Lee, K.; Han, S.; Jeong, W.; Jeon, H. *J. Electrochem. Soc.* **2007**, *154*, H177-H181.

74. Lee, H.-B.-R.; Kim, H., *Electrochem. Solid-State Lett.* **2006**, *9*, G323-G325.

75. Lee, K.; Kim, K.; Park, T.; Jeon, H.; Lee, Y.; Kim, J.; Yeom, S. *J. Electrochem. Soc.* **2007**, *154*, H899-H903.

76. Park, J.-H.; Moon, D.-Y.; Han, D.-S; Shin, S.-R.; Jeon, H.-T.; Park, J.-W. *Surf. Coat. Technol.* **2014**, *259*, 98-101.

77. Lim, B. S.; Rahtu, A.; Park, J.-S.; Gordon, R. G. *Inorg. Chem.* **2003**, *42*, 7951-7958.

78. Li, Z.; Gordon, R. G.; Farmer, D. B.; Lin, Y.; Vlassak, J. *Electrochem. Solid-State Lett.* **2005**, *8*, G182-G185.

79. Li, Z.; Rahtu, A.; Gordon, R. G. *J. Electrochem. Soc.* **2006**, *153*, C787-C794.

80. Li, Z.; Lee, D. K.; Coulter, M.; Rodriguez, L. N. J.; Gordon, R. G. *Dalton Trans.* **2008**, 19, 2592-2597.

81. Lim, B. S.; Rahtu, A.; Gordon, R. G. *Nat. Mater.* **2003**, *2*, 749-754.

82. Klesko, J. P.; Kerrigan, M. M.; Winter, C. H. *Chem. Mater.* **2016**, *28*, 700-703.

83. Kwon, J.; Saly, M.; Halls, M. D.; Kanjolia, R. K.; Chabal, Y. J. *Chem. Mater.* **2012**, *24*, 1025-1030.

84. Kalutarage, L. C.; Martin, P. D.; Heeg, M. J.; Winter, C. H. *J. Am. Chem. Soc.* **2013**, *135*, 12588-12591.

85. Ishikawa, M.; Kada, T.; Machida, H.; Ohsita, Y.; Ogura, A. *Jpn. J. Appl. Phys.* **2004**, *43*, 1833-1836.

86. Chae, J.; Park, H.-S.; Kang, S.-W. *Electrochem. Solid-State Lett.* **2002**, *5*, C64-C66.

87. Stauf, G. T.; Driscoll, D. C.; Dowben, P. A. *Thin Solid Films* **1987**, *153*, 421-430.

88. Yoo, S. H.; Choi, H.; Kim, H.-S.; Park, B. K.; Lee, S. S.; An, K.-S.; Lee, Y. K.; Chung, T.-M.; Kim, C. G. *Eur. J. Inorg. Chem.* **2011**, 1833-1839.

89. Lee, H.-B.-R.; Bang, S.-H.; Kim, H.-W.; Gu, G. H.; Lee, Y. K.; Chung, T.-M.; Kim, C. G.; Park, C. G.; Kim, H. *Jpn. J. Appl. Phys.* **2010,** *49*, 05FA11.

90. Lee, K.-M.; Kim, C. Y.; Choi, C. K.; Yun, S.-W.; Ha, J.-B.; Lee, J.-H.; Lee, J. Y. *J. Korean Phys. Soc.* **2009,** *55*, 1153-1157.

91. Daub, M.; Knez, M.; Goesele, U.; Nielsch, K. *J. Appl. Phys.* **2007,** *101*, 09J111.

92. Knisley, T. J.; Saly, M. J.; Heeg, M. J.; Roberts, J. L.; Winter, C. H. *Organometallics* **2011**, *30*, 5010-5017.

93. Hämäläinen, J.; Ritala, M.; Leskelä, M. *Chem. Mater.* **2014**, *26*, 786-801.

94. Hsu, I. J.; McCandless, B. E.; Weiland, C.; Willis, B. G. *J. Vac. Sci. Technol. A* **2009**, *27*, 660-667.

95. Adner, D.; Korb, M.; Schulze, S.; Hietschold, M.; Lang, H. *Chem. Comm.* **2013**, *49*, 6855-6857.

96. Aboaf, J. A.; Herd, S. R.; Klokholm, E. *MAG-19*, **1998**, 1514-1519.

97. Kalutarage, L. C.; Clendenning, S. B.; Winter, C. H. *Chem. Mater.* **2014**, *26*, 3731-3738.

98. Elko-Hansen, T. D. M.; Dolocan, A.; Ekerdt, J. G. *J. Phys. Chem. Lett.* **2014**, *5*, 1091-1095.

99. Ito, K.; Bernstein, H. J. *Can. J. Chem.* **1956,** *34*, 170-178.

100. *The Electrical Properties of Metals and Alloys*; Dugdale, J. S.; Courier Dover Publications: 2016.

ABSTRACT

SELECTIVE ATOMIC LAYER DEPOSITION OF TRANSITION METAL THIN FILMS

by

MARISSA MARIE KERRIGAN

August 2017

Advisor: Dr. Charles H. Winter

Major: Chemistry (Inorganic)

Degree: Doctor of Philosophy

Atomic layer deposition (ALD) affords highly conformal thin films with precise thickness control due to its self-limited growth mechanism. ALD enables the increasing demands for smaller feature sizes in microelectronics devices to be met. Area-selective ALD growth is receiving attention in the fabrication of microelectronic devices, since it can eliminate complicated etching steps from the fabrication process and minimizes expensive and toxic reagent use. Selectivity can be achieved by tailoring the surface chemistry of the precursor and substrate. To date, few area-selective ALD processes have been reported for metallic films. Thin films of cobalt metal deposited selectively are of considerable interest for use in microelectronics devices, specifically as a metallization liner in sub-10 nm logic nodes. Our laboratory has recently reported an ALD process for cobalt metal thin films using bis(1,4-di-*tert*-butyl-1,3-diazabutadienyl)cobalt(II), $Co(^{tBu2}DAD)_2$, and formic acid. This process affords high-purity, low-resistivity cobalt films. Excellent cobalt metal film growth also occurs on metallic substrates, with a growth rate of ~0.95 Å/cycle. In this work, I will describe the early stage nucleation and selective

growth of cobalt metal from Co(^{tBu2}DAD)$_2$ and formic acid on ruthenium, platinum, and copper substrates. No cobalt metal growth is observed on nonmetallic substrates. I will also describe the development of a new inherently substrate-selective ALD process for high-purity, low-resistivity (~13 μΩcm) cobalt metal from Co(^{tBu2}DAD)$_2$ and alkyl amines, with a GR of 0.98 Å/cycle on metal substrates. No cobalt metal growth is observed on dielectric substrates. I will also describe the development of a new inherently substrate-selective ALD process for high-purity, low-resistivity (~20 μΩcm) nickel metal from Ni(^{tBu2}DAD)$_2$ and alkyl amines, with a growth rate of 0.60 Å/cycle on metal substrates. No nickel metal growth is observed on dielectric substrates.

AUTOBIOGRAPHICAL STATEMENT

MARISSA MARIE KERRIGAN

Education:

Ph.D., Inorganic Chemistry, Wayne State University, Detroit, MI
2012–2017; GPA: 3.84 (4.00)

B.S., Chemistry, University of Michigan, Dearborn, MI
2007–2012; GPA: 3.30 (4.00)

Publications:

1. Sirimanne, C. T.; **Kerrigan, M. M.**; Martin, P. D.; Kanjolia, R. K.; Elliot, S. D.; Winter, C. H. "Reductive Elimination of Hypersilyl Halides from Zinc(II) Complexes. Implications for Electropositive Metal Thin Film Growth." *Inorg. Chem.*, **2015**, *54*, 7-9.

2. Klesko, J. P.; **Kerrigan, M. M.**; Winter, C. H. "Low Temperature Thermal Atomic Layer Deposition of Cobalt Metal Films." *Chem. Mater.* **2016**, *28*, 700-703.

3. **Kerrigan, M. M.**; Klesko, J. P.; Rupich, S. M.; Dezelah, C. L.; Kanjolia, R. K.; Chabal, Y. J.; Winter, C. H. "Substrate Selectivity in the Low Temperature Atomic Layer Deposition of Cobalt Metal Films from Bis(1,4-di-*tert*-butyl-1,3-diazadienyl)cobalt and Formic Acid." *J. Chem. Phys.* **2017**, *146*, 052813.

4. Peeters, D.; Taffa, D. H.; **Kerrigan, M. M.**; Ney, A.; Jöns, N.; Rogalla, D.; Cwik, S.; Becker, H.-W.; Grafen, M.; Ostendorf, A.; Winter, C. H.; Chakraborty, S.; Wark, M.; Devi, A. "Photoactive Zinc Ferrites Fabricated via Conventional CVD Approach." *ACS Sustainable Chem. Eng.* **2017**, *5*, 2917–2926.

5. **Kerrigan, M. M.**; Klesko, J. P.; Winter, C. H. "Low Temperature Growth and Substrate Selectivity of Cobalt Metal Thin Films by Thermal Atomic Layer Deposition from Bis(1,4-di-*tert*-butyl-1,3-diazadienyl)cobalt and Amines." *Manuscript in progress* **2017**.

6. **Kerrigan, M. M.**; Klesko, J. P.; Winter, C. H. "Low Temperature Growth and Substrate Selectivity of Nickel Metal Thin Films by Thermal Atomic Layer Deposition from Bis(1,4-di-*tert*-butyl-1,3-diazadienyl)nickel and Amines." *Manuscript in progress* **2017**.